

**Degradable Core-Multishell Nanocarriers for the Delivery of  
Bioactive Molecules**

DISSERTATION

zur Erlangung des akademischen Grades des  
Doktors der Naturwissenschaften (Dr. rer. nat.)

eingereicht im Fachbereich Biologie, Chemie, Pharmazie  
der Freien Universität Berlin

vorgelegt von

**Fang Du**

aus Hunan, China

November, 2017

The results showed in this thesis were performed from October 2013 to November 2017 under the supervision of Prof. Dr. Rainer Haag at the Institute of Chemistry and Biochemistry of the Freie Universität Berlin.

1st Reviewer: Prof. Dr. Rainer Haag, Freie Universität Berlin

2nd Reviewer: PD. Dr., Kai Licha, Freie Universität Berlin

Date of Defense: 18. 12. 2017

## **Acknowledgement:**

The past 4 years doing my PhD in FUB has been the most precious experience for me. Here I have learnt not only how to do science and research independently, but also many other new things, made new friends and gained a new attitude. With this opportunity, I would like to thank those who love and encourage me and those who help and support me to finish my PhD thesis.

First of all, I thank Prof. Rainer Haag for offering me the opportunity working in this group. He provides me plenty of supports and scientific suggestions to accomplish my projects and fulfil my own idea. So much things I have learnt from him, for example, how to do research, how to make professional connections, as well as being detail-oriented, patient and diligent. His passion towards work continuously motives me to move on.

I also thank PD. Dr. Kai Licha for being my second referee and for spending his time on reading my thesis.

A special thanks to my collaborators Prof. Dr. Sarah Hedtrich, Guy Yealland, Stefan Hönzke and Patrick Graff from the Pharmacy Department of FUB for conducting all the in vitro skin experiments, Prof. Dr. Nan Ma, Falko Neumann and Yan Li for the cytotoxicity tests, Prof. Dr. Roland Netz and Richard Schwarzl from the Physics Department of FUB for the release kinetics studies, Prof. Dr. Burkhard Kleuser and Dr. Fabian Schumacher from Potsdam University for the LC-MS measuring, Prof. Dr. Achim Grube, Hannah Pischon, Moritz Radbruch for the on-going in vivo skin penetration tests. I would like to acknowledge Dr. Andreas Schäfer for the NMR measurements and Dr. Christoph Böttcher for the Cryo-TEM measurements.

I'd like to acknowledge our lab assistant Marleen Selent for measuring hundreds of HPLC samples, Anja Stöshel and Cathleen Schlesener for providing me hPG. A special thank to Dr. Pamela Winchester for the proof-reading of my manuscripts and thesis and to Dr. Wiebke Fischer for her tremendous help in many aspects.

I would like to thank all the AG Haag members, especially my labmates, my former (lovely Chinese mafia) and present officemates for creating such a nice working

atmosphere. I will miss our annual multicultural lab dinner event for sure. Special thanks go to my hoodmate Karolina Walker, to Dr. Lingyan Gao, Qingcai Zhao and Antara Sharma for all the interesting scientific as well as non-scientific topics discussing. Many thanks to Dr. Virginia Wycisk, Leonhard Urner and Karolina Walker for the translation work and that is a huge help.

Finally, I would like to thank my parents, my sister, meine Deutschlehrerin Christa Wunderlich, my husband and my cat friend Luy for always being there for me. Their love and supports bring me a lot of energy to explore the unknown and to overcome the difficulties in front of me.

# Table of content

Chapter 1. Introduction .....	1
1.1 Nanoscale Drug Delivery Systems.....	1
1.2 Degradable DDS .....	6
1.3 Self-assembled Core-shell Delivery Systems .....	11
1.4 Dendritic Core-(Multi)shell Systems .....	12
1.5 Topical Drug Delivery .....	17
Scientific Goals.....	26
Chapter 2. Degradable CMS with Different Hydrophobicity for Efficient Topical Drug Delivery .....	28
2.1 Design of hPG-PCL <sub>m</sub> -mPEG CMS Nanocarriers .....	28
2.2. Self-Aggregation Properties of hPG-PCL <sub>m</sub> -mPEG.....	33
2.3. Encapsulation Studies .....	34
2.4. Drug Release Study.....	36
2.5. Skin Penetration .....	37
2.6. Cytotoxicity.....	39
2.7 Cellular Uptake .....	40
2.8 Bovine Corneal Opacity and Permeability (BCOP) Test.....	41
Chapter 3. Skin Penetration of Tacrolimus-containing CMS Formulations.....	44
3.1 Comparison of Different Drug Loading Methods.....	44
3.2 Formulation Preparation with Different Tacrolimus Contents .....	45
3.3 Release Study .....	46
3.4 In vitro Skin Penetration of Tacrolimus-Containing Formulations .....	47
Chapter 4. Cationic CMS as Potential Platform for Topical Multi-payloads Delivery. .....	50
4.1. Design of Core-multishell Unimicellar Systems.....	50
4.2. Aggregation Properties of CMS.....	53
4.3. Encapsulation and Release Studies .....	56
4.4. QCM-D Study on Interactions between CMS and SC Model .....	58

4.5. ATR-FTIR Study on Interactions between CMS and Isolated SC from Human Skin .....	60
4.6. Skin Penetration of CMS Containing Different Payloads.....	61
4.7 Cytotoxicity.....	64
Chapter 5. Experimental Part.....	66
5.1 Degradable CMS with Different Hydrophobicity for Efficient Topical Drug Delivery.....	67
5.2 Skin Penetration of Tacrolimus-containing CMS Formulations.....	73
5.3 Cationic CMS as Potential Platform for Topical Multi-payloads Delivery. ....	75
Summary and Outlook .....	82
Zusammenfassung.....	84
Appendix.....	88
References.....	105
Curriculum Vitae .....	114

## Abbreviations

ABU	Arbitrary pixel brightness values
ATRP	Atom-transfer radical polymerization
AUC	Area under the curve
BCOP	Bovine corneal opacity and permeability
BBB	Blood brain barrier
BSA	Bovine serum albumin
CAC	Critical aggregation concentration
CLSM	Confocal laser scanning microscope
CMC	Critical micelle concentration
CMS	Core-multishell
CTB	Cholera toxin B
Da	Dalton
DAPI	4',6-diamidino-2-phenylindole
DDS	Drug delivery system
DEA	2-Diethylaminoethanethiol
DM	Dendron-based micelle
dPG	Dendritic polyglycerol
DOX	Doxorubicin
DTT	1,4-dithiothreitol
EE	Encapsulation efficiency
EPR	Enhanced permeation and retention
FDA	US Food and Drug Administration
FITC	Fluorescein isothiocyanate
G2	Generation 2
GSH	Glutathione
HES	Hydroxyethyl starch
hPG	Hyperbranched polyglycerol
IVIS	<i>in vitro</i> irritation score

LC	Loading capacity
IPG	Linear polyglycerol
$\log P$	1-octanol/PBS Partition Coefficients
mPEG	Mono methyl ether poly(ethylene glycol)
MWCO	Molecular weight cut off
PAMAM	Poly(amido amine)
PAsp	Poly(aspartate)
PBS	Phosphate-buffered saline
PCL	Poly( $\epsilon$ -caprolactone)
PAEMA	Poly(2-azepane ethyl methacrylate)
PDI	Polydispersity index
PEEP	Poly(ethyl ethylene phosphate)
PEI	Poly(ethylene imine)
PEGylated	Poly(ethylene glycol)-conjugated
pI	Isoelectric point
PLGA	Poly(lactide-co-glycolide)
PPO	Poly(propylene oxide)
QCM-D	Quartz crystal microbalance with dissipation monitoring
RES	Reticuloendothelial system
RGC	Retinal ganglion cell
RhoB	Rhodamine B
ROP	Ring opening polymerization
RT	Room temperature
RTCA	Real-time cell index analysis
SC	Stratum corneum
SLN	Solid lipid nanoparticle
TAC	Tacrolimus
TDD	Topical drug delivery
VE	Viable Epidermis



# Chapter 1. Introduction

## 1.1 Nanoscale Drug Delivery Systems

The pharmacokinetic limitations associated with conventional therapeutics such as fast clearance, random distribution, and undesirable side effects often cause failure in many complex diseases' treatment.<sup>[1]</sup> Nanoscale drug delivery systems (DDS) have emerged as powerful vehicles to specifically target the delivery of conventional therapeutics with improved bioavailability and pharmacokinetics into the site of diseases. As controlled release systems, they can sustainably release the therapeutics at the site of action to maintain the desired therapeutic concentration for hours, even days after a single administration as illustrated in Figure 1-1.<sup>[2]</sup> Therefore, repeated administrations of high dosage conventional therapeutics can be avoided.

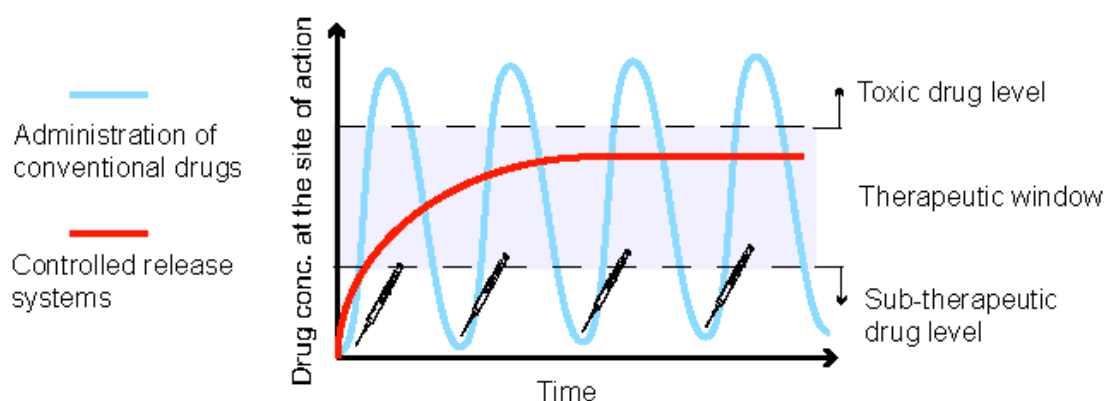


**Figure 1-1.** Drug concentration against time on the target site: Four times injection of conventional drugs (blue); Single time injection of drugs encapsulated in controlled release systems (red)

In the past two decades, many drug delivery products reached the market for the treatment of various diseases, including cancer, fungal infections, hepatitis A, and many

other chronic diseases. (Table 1-1).<sup>[1]</sup> For example, the first FDA-approved nanodrug Doxil<sup>[3]</sup>, PEGylated liposomal doxorubicin, is indicated for Kaposi sarcoma and several types of cancer. Its long circulation half-life and selective accumulation at the disease site led to significantly decreased toxicity compared to the conventionally formulated DOX.

**Table 1-1.** Some examples of DDS products on the market and their applications.<sup>[1]</sup>

Product name	Composition	Indication
Abelcet	Amphotericin B/ lipid complex	Fungal infections
Amphotec	Amphotericin B/ lipid colloidal dispersion	Fungal infections
Ambisome	Liposomal Amphotericin B	Fungal infections
DaunoXome	Liposomal daunorubicin	Kaposi sarcoma
Doxil/Caelyx	Liposomal doxorubicin	Cancer, Kaposi sarcoma
Depocyt	Liposomal cytarabine	Cancer
Epaxal Berna	Virosomal hepatitis vaccine	Hepatitis A
Inflexal V Berna	Virosomal influenza vaccine	Influenza
Myocet	Liposomal doxorubicin	Breast cancer
Estrasorb	Estradiol in micellar nanoparticles	Menopausal therapy

Polymeric DDS have had an enormous impact on drug therapy and have been considered as one of the most successful technological advances in therapeutics in the 21<sup>st</sup> century.<sup>[4]</sup> Generally, the polymeric DDS can be divided into two classes, namely, polymer-drug conjugates (prodrugs) and colloidal drug delivery systems such as micelles, polymersomes and nanogels (Figure 1-2). In the first case, therapeutic agents are covalently bonded to polymer backbones via cleavage linkers. Once the prodrug is

internalized into targeted cells, the active drug is released. In contrast to prodrugs, where the colloidal DDS is used, therapeutics can be physically encapsulated which allows more universal drug loading and is also relatively simple to perform without complex synthetic steps. By tuning the composition and surface area of the colloidal DDS, the rate of drug release can be adjusted based on the therapeutic requirement.

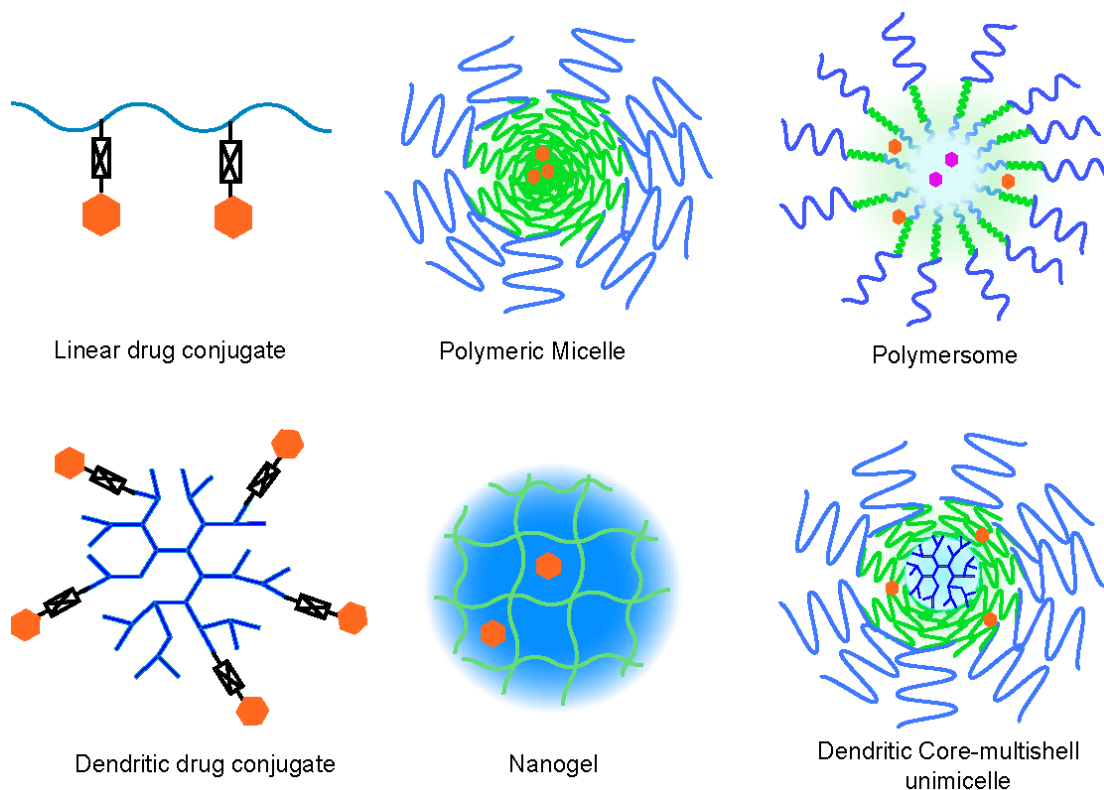


**Figure 1-2.** Overview of polymeric drug delivery systems: prodrug based on linear or dendritic polymer backbones, self-assembled micelles, polymersomes, nanogel, and unimolecular core-multishell (CMS) architectures.

The fate of DDS *in vivo* is limited by one or more biological barriers depending on the method of administration. For example, an efficacious outcome only happens when the DDS overcome barriers like skin<sup>[5]</sup> or mucus<sup>[6]</sup> for topical application. For tumor therapy, despite the increased half-life and accumulation of DDS at the tumor site, therapeutic outcomes are still limited by poor tumor penetration and cellular

internalization, inability to escape from endosome/lysosome and to overcome drug efflux pumps.<sup>[7]</sup> For brain disease treatment, the ability of the DDS to cross the blood brain barrier (BBB)<sup>[8]</sup> is crucial. To overcome these above mentioned biological barriers, particle size and surface properties including surface composition, functionalization, charge, shape et al. are the most important designing parameters.

A proper-sized DDS can significantly improve the accumulation of therapeutics to the site of disease. For an intravenous injection, small particles (4 - 6 nm) are rapidly eliminated by renal clearance.<sup>[9]</sup> Large particles, especially with hydrophobic surfaces, prefer to accumulate in lung, liver, or spleen, which can cause severe organ damage.<sup>[10]</sup> For passive tumor targeting, the ideal size range for DDS is 20-200 nm.<sup>[11]</sup> The microenvironment of tumors is full of leaky blood vessels and impaired lymphatic drainage.<sup>[12]</sup> Nanomedicine in this size range shows the best accumulation in solid tumors because of the enhanced permeability and retention (EPR) effect.<sup>[13]</sup> Recently, more and more research has been focused on sub 100 nm particles. Kataoka and coworkers<sup>[14]</sup> have found that 30 nm micelles could penetrate poorly permeable pancreatic tumors to achieve an antitumor effect, whereas micelles ~ 100 nm only showed in highly permeable tumors. Inspired by that, Wang et al.<sup>[15]</sup> designed a nano-bomb that was 100 nm at neutral pH and quickly disintegrated into small drug-conjugated particles around 10 nm at tumor acidic pH, which provided new ways to combine a good accumulation of large nanoparticles and deep tumor penetration of small nanoparticles (Figure 1-3). The same trend has also been found in topical drug delivery because small carriers could facilitate drug penetration better than bigger ones, which will be discussed more in detail in Section 1.5.2

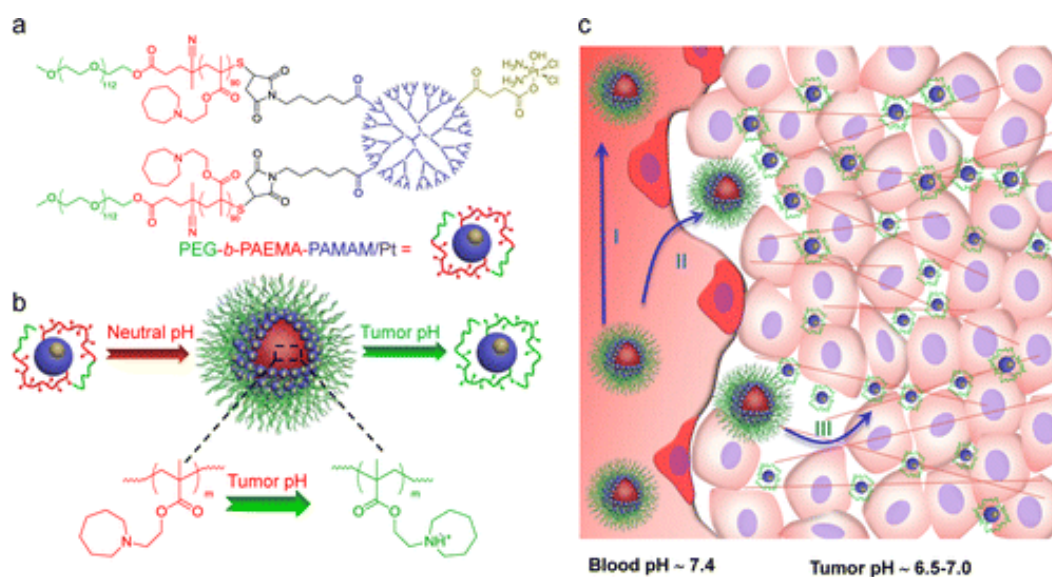


**Figure 1-3.** a) Chemical structure of the Pt-dendrimeric prodrug PEG-*b*-PAEMA-PAMAM/Pt; b) Self-assembly of PEG-*b*-PAEMA-PAMAM/Pt into cluster nano-bombs due to hydrophobic interaction at physiological pH and dissociation of nano-bombs into small dendritic prodrug due to protonation of tertiary amine at tumor acidic pH (pH 6.5-7); c) Illustration of the nano-bombs successfully delivery drugs to poorly permeable pancreatic tumor models via size transition strategy. Figure reprinted from literature<sup>[15]</sup> Copyright 2016 American Chemical Society.

Surface composition is another crucial factor, which has to be considered for a targeted delivery of active agents that can stabilize the colloids in water or an even more complex biological environment. Non-specific adsorption of the biological components to the surface of DDS could result in premature drug release,<sup>[16]</sup> elimination by immune system<sup>[17]</sup>, low barrier permeability,<sup>[18]</sup> and severe in vivo nano-toxicity.<sup>[19]</sup> To avoid these problems, it is essential to grant a DDS with a “stealth effect” to decrease the “off-target” ratio. The “stealth effect” is usually achieved by attaching neutral hydrophilic polymers to the surface of DDS.<sup>[20]</sup> Poly(ethylene glycol) (PEG) is the most used material so far, since two PEGylated protein products successfully entered the market in 1990s. Now PEG is considered a gold standard for the “stealth” effect to protect therapeutic agents from accumulating in the reticulo-endothelial system (RES), which

is part of the immune system.<sup>[21]</sup> The main disadvantage of PEG is its limited functional group and increased potential of a hypersensitive reaction because of the increased usage of PEG and PEGylated products in daily life.<sup>[22]</sup> With the fast development of polymer chemistry, many other polymers have been proposed as promising PEG substitutes, for example, linear or hyperbranched polyglycerol (IPG/dPG),<sup>[23]</sup> hydroxyethyl starch (HES),<sup>[24]</sup> poly (ethyl ethylene phosphate) (PEEP),<sup>[21a]</sup> and some zwitterionic polymers<sup>[25]</sup> (Figure 1-4). Among all the candidates, IPG/hPG, as multifunctional analogs of PEG, are the most promising ones because they display good water solubility and biocompatibility.

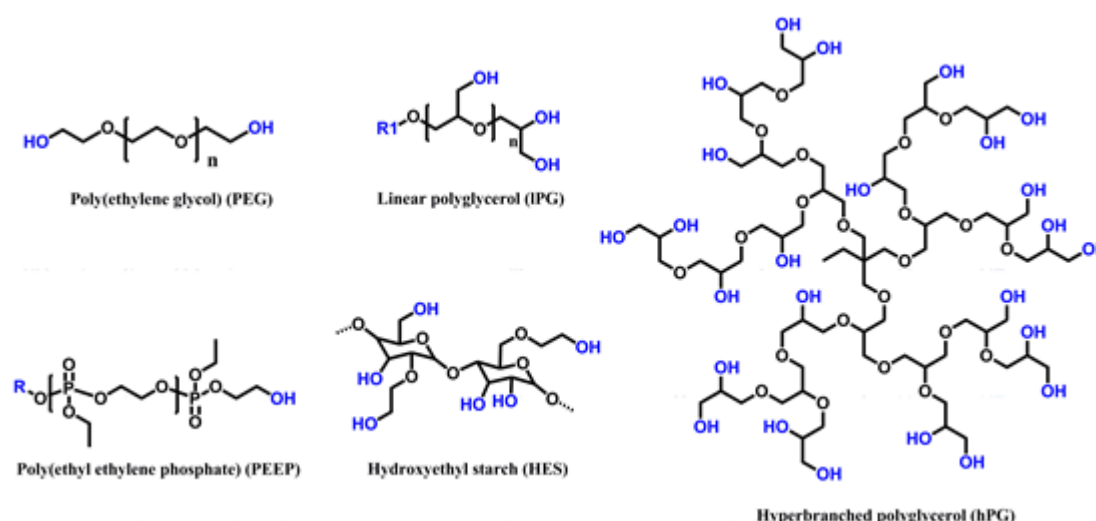


**Figure. 1-4.** Chemical structures of polymers that can be attached to surface of nanocarriers to reduce non-specific protein absorptions.

Other features, such as surface functionality and charge, also can heavily influence the interactions between the DDS and biomembranes. They will be discussed in more detail specifically for topical drug delivery systems designing in section 1.5.2.

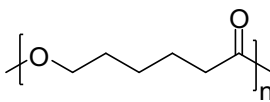
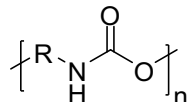
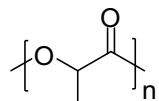
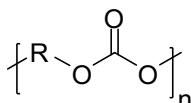
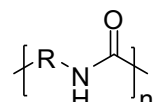
## 1.2 Degradable DDS

Degradable polymers represent one of the preferred classes of polymers used in

developing drug delivery systems. Their backbone can be degraded into small molecules in physiological conditions, mostly by hydrolysis or enzymatic cleavage,<sup>[26]</sup> and are thereby easily eliminated from the body after they have served their functions to avoid long term toxicity. Drug release from the DDSs are also related to the degradation rate of these polymers, which is depending on their molecular weight, crystallinity, and conditions of degradation.<sup>[27]</sup> Generally, the higher crystallized degree the structure, the slower degradation rate it has. Degradable polymers can be divided into two classes, namely, naturally existing polymers<sup>[28]</sup> and synthetic polymers.<sup>[29]</sup> Although they are abundant and low cost, it is not easy to achieve a controlled degree of functionalization for natural polymers. Instead, synthetic polymers such as polyesters,<sup>[30]</sup> polycarbonates,<sup>[29b]</sup> and polypeptides<sup>[31]</sup> offer more structural versatility. Table 1-2 shows a summary of degradation rates and structural information for degradable synthetic polymer families.<sup>[32]</sup>

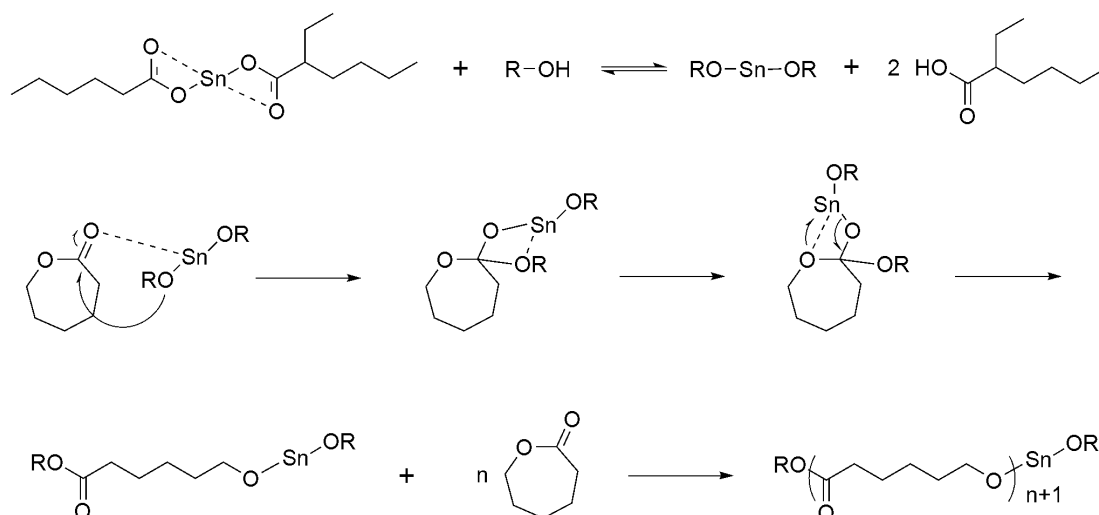
**Table 1-2.** Summary of structure information and degradation rate of common used degradable synthetic polymers for building drug delivery systems.<sup>[32]</sup>

Polymer	Structure	Degradation rate constant (s <sup>-1</sup> )
Polyphosphazenes	$\left[ \begin{array}{c} R_1 \\   \\ -P=N- \\   \\ R_2 \end{array} \right]_n$	$4.5 \times 10^{-2} - 1.4 \times 10^{-7}$
Polyanhydrides	$\left[ \begin{array}{c} O \quad O \\    \quad    \\ -C-R-C-O- \\   \quad   \end{array} \right]_n$	$1.9 \times 10^{-3} - 9.4 \times 10^{-9}$
Polyacetals	$\left[ \begin{array}{c} R_2 \quad R_3 \\ \diagdown \quad / \\ -R_1-O-C-O- \\ / \quad \diagdown \end{array} \right]_n$	$6.4 \times 10^{-5}$
Poly(ortho esters)	$\left[ \begin{array}{c} R_2 \quad O-R_3 \\ \diagdown \quad / \\ -R_1-O-C-O- \\ / \quad \diagdown \end{array} \right]_n$	$4.8 \times 10^{-5}$
Polyphosphoesters	$\left[ \begin{array}{c} O \\    \\ -R_1-O-P-O- \\   \\ R_2 \end{array} \right]_n$	$1.4 \times 10^{-6}$

Polycaprolactone		$3.5 \times 10^{-8}$
Polyurethanes		$8.3 \times 10^{-9}$
Poly lactide		$6.6 \times 10^{-9}$
Polycarbonates		$4.1 \times 10^{-10}$
Polyamides		$2.6 \times 10^{-13}$

Aliphatic polyesters, such as poly( $\epsilon$ -caprolactone) (PCL), are widely used materials for biomedical applications.<sup>[30, 33]</sup> Ring-opening polymerization (ROP) of the monomer  $\epsilon$ -caprolactone is the most common way to synthesize PCL. There are four main mechanisms, namely, anionic,<sup>[34]</sup> cationic,<sup>[35]</sup> monomer-activated,<sup>[36]</sup> and coordination-insertion<sup>[37]</sup> ROP, depending on the catalyst used. Stannous(II) ethylhexanoate ( $\text{Sn}(\text{Oct})_2$ ) is certainly one of the most frequently used catalyst for the ROP of  $\epsilon$ -CL, because it is cheap, effective, easy to handle, and soluble in a wide range of organic solvents. The mechanism of tin-induced ROP is shown in Scheme 1-1. The main drawback is that a high temperature is required during synthesis, which could cause side reactions to broaden the polydispersity.<sup>[38]</sup>





**Scheme 1-1.** Mechanism of ROP polymerization of  $\epsilon$ -CL catalyzed by tin(II) octoate.

The main limitation for the above-mentioned traditional polyesters is the absence of functionality on the polymer backbone. Recently, the design and synthesis of functional polyesters have drawn a lot of interest.<sup>[29a, 39]</sup> They can be prepared either by copolymerizing modifiable cyclic ester monomers or with other commercially available functional monomers, for example, carbonate<sup>[40]</sup> and epoxide monomers.

Alkyne- and alkene-bearing monomers are the most frequently used functional monomers, because combining ROP and “click” reactions allows a straightforward synthesis of polyesters bearing tailored functional groups for different biological applications. As an example, Emrick et al.<sup>[39]</sup> synthesized aliphatic polyesters with pendent acetylene groups by ring-opening copolymerizing alpha-propargyl- $\delta$ -valerolactone and  $\epsilon$ -caprolactone. They successfully proved that this platform could be further used for grafting azide-functionalized macromolecules such as poly(ethylene glycol) and oligopeptide by “click” chemistry under mild conditions without causing backbone degradation. The resulting polyesters have shown very good biocompatibility. Jing et al.<sup>[41]</sup> and Dove et al.<sup>[42]</sup> reported first an allyl-functional carbonate monomer, 5-methyl-5-allyloxycarbonyl-1,3-dioxan-2-one (MAC), which could undergo homopolymerization or be copolymerized with different ratios of L-lactide to yield poly(LA-MAC) random copolymers bearing pendent allyl ester groups. Further

quantitative functionalization of the homo-/copolymers was realized via the “thiol-ene” click reaction with negligible backbone degradation.

Involving of stimuli-sensitive linkers is another approach to synthesizing degradable DDS. The degradation of the DDS can be triggered either by internal stimuli such as enzyme, pH, redox potential or by external stimuli such as near infrared or UV light at the disease site, resulting in a fast release of cargos. Figure 1-5 shows examples of labile linkers for synthesis of degradable DDS.<sup>[43]</sup>

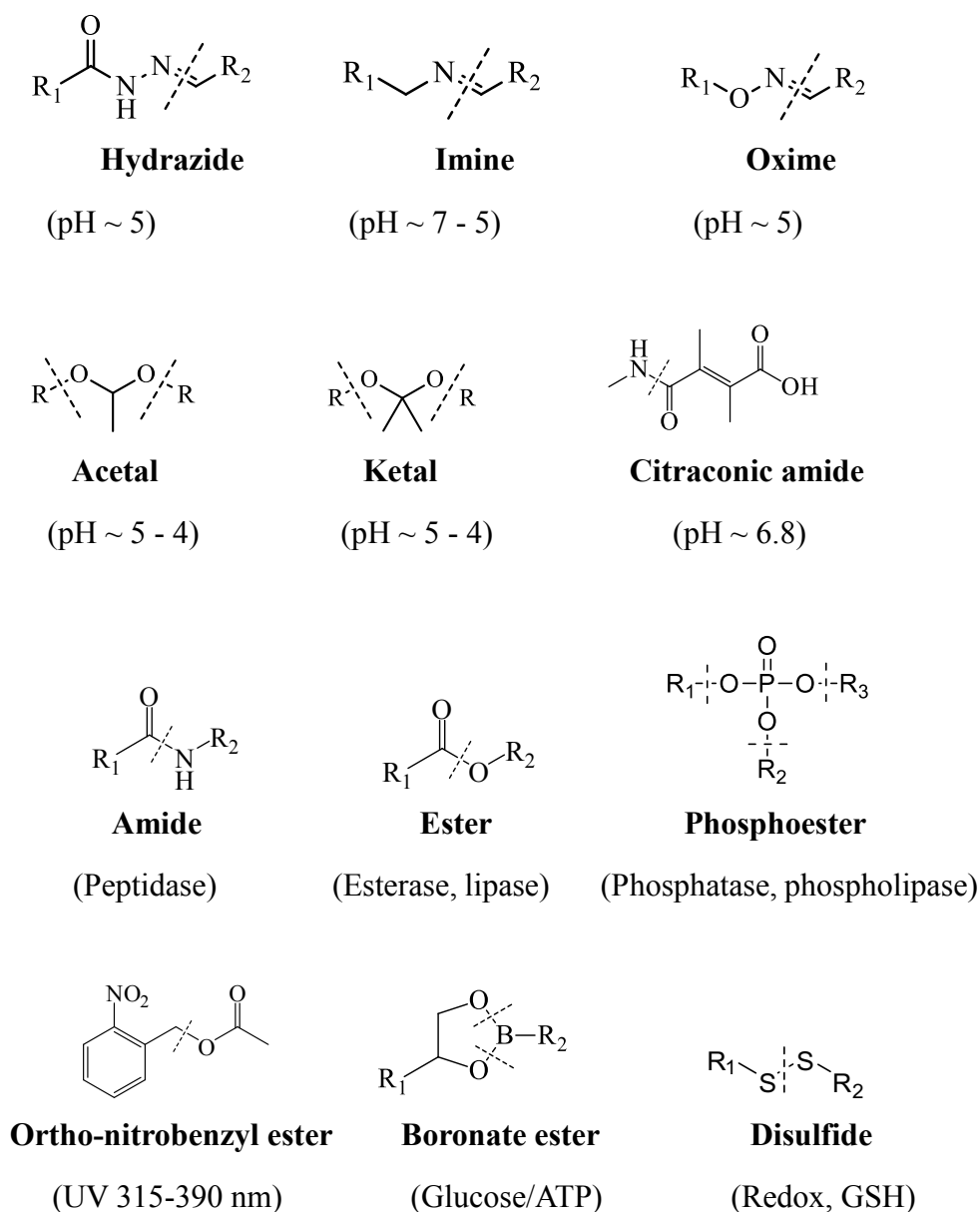


**Figure 1-5.** Structure information and degradation condition of some examples of labile linkers for building degradable DDS.<sup>[43]</sup>

### 1.3 Self-assembled Core-shell Delivery Systems

Polymeric micelles, self-assembled from block copolymers, are the most studied platform for drug delivery. They are superior to their analogs made from small molecules regarding physical and chemical stability.<sup>[44]</sup> These micelles generally provide a core-shell structure, where hydrophobic segments are segregated from the aqueous environment to form a core surrounded by hydrophilic shell. The driving force for micellization is a combination of intermolecular forces, including hydrophobic interaction,<sup>[45]</sup> metal complexation,<sup>[46]</sup> hydrogen bonding,<sup>[47]</sup> and electrostatic interaction.<sup>[48]</sup> Hydrophobic drugs can be physically encapsulated in the hydrophobic core of micelles with enhanced water solubility and bioavailability. In the late 1980s, Kataoka and coworkers<sup>[49]</sup> developed core-shell micelles from PEG-*b*-poly( $\alpha,\beta$ -aspartic acid) copolymer with DOX-conjugated via amide bonds, which could further physically encapsulate DOX via  $\pi$ - $\pi$  stacking. In preclinical studies, these micelles showed a 29-fold larger area under the curve (AUC) of drug concentration versus time in plasma and a 3.4-fold higher accumulation amount in tumor, compared to the free DOX.<sup>[50]</sup> This was the first micelle that proceeded into clinical trials in 2001. Even though the critical micelle concentration (CMC) was significantly lower for polymeric assemblies, kinetic stability issues still need to be addressed for systems based on self-assembly. Disassembly can happen upon high dilution and interaction with plasma components like protein, which could result in a premature drug release.<sup>[16]</sup> Yang and co-workers<sup>[51]</sup> recently studied the effect of kinetic stability of DOX loaded assemble micelles on tumor targeting and antitumor efficacy. The mixed micelle system secured by strong intermolecular H-bonds demonstrated faster and a greater extent of accumulation in tumors and more effective inhibition of tumor growth than the micelles with low kinetic stability. Therefore, kinetic stability is a very important parameter to consider to achieve positive therapeutic outcomes. Another problem associated with assembled systems is that the size of assembled micelle might be significantly increased after drug loading. This could be disadvantageous especially for some applications where size plays a crucial role. To solve aforementioned problems, new types of

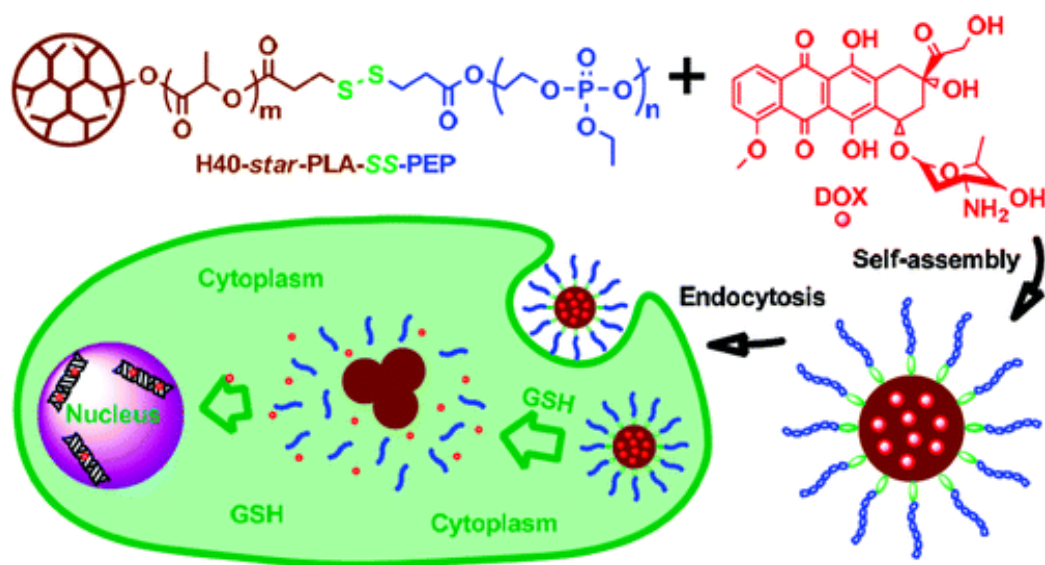
colloidal DDS with more stable structures have been developed including crosslinked micelles,<sup>[52]</sup> unimolecular dendritic core-multishell systems,<sup>[53]</sup> and nanogels.<sup>[54]</sup>

#### **1.4 Dendritic Core-(Multi)shell Systems**

Dendritic core-(multi)shell nanocarriers specifically describe the carriers based on a dendritic polymer core surrounded by many linear or dendritic polymers as shells. The most common dendritic polymers as building blocks for CMS nanocarriers are poly(amido amine) (PAMAM),<sup>[55]</sup> hyperbranched polyesters,<sup>[56]</sup> poly(ethylene imine) (PEI),<sup>[57]</sup> dendritic polyglycerol (dPG).<sup>[58]</sup> The core and shells are connected by covalent bonds, which gives the whole system very good thermodynamical and kinetical stability and remedies a common defect of the assembled nanocarriers that they might disassemble in highly diluted situation. This quality makes dendritic core-multishell systems very attractive for drug delivery. Sometimes dendritic core-multishell systems are also termed “unimicelles,” because they share similar properties with the traditionally assembled micelles. From the structural perspective, they all consist of several segments from the interior core to the exterior shell with a polarity difference between them. It is the same as the traditional micelle, the internal space of the dendritic systems (either the core or inner shell, sometimes both) is non-polar and hydrophobic which can accommodate water-insoluble drugs. The polar and hydrophilic outer shell is for stabilizing the whole system in water. The main difference between those two is the so-called unimicelle, a “micelle” consisting of a single molecule usually around 10-20 nm. In contrast, the traditional micelles are usually 15-100 nm formed by aggregation due to physically intermolecularly interactions. In reality, “unimicelle” cannot be used for all the dendritic core-multishell carriers. Some “unimicelles” can further assemble to form bigger supramolecular aggregates ranging from hundreds of nanometers to micrometers due to the intermolecular interactions.<sup>[59]</sup> In our group, we found that the encapsulation of a certain amount of the Nile red dye could induce the transition from the original single molecular micelle to multimolecular aggregates that were uniformly distributed in a size range from 220 to 250 nm.<sup>[60]</sup> It was further

proven that this aggregation can be converted to single molecular CMS by dilution.<sup>[61]</sup>

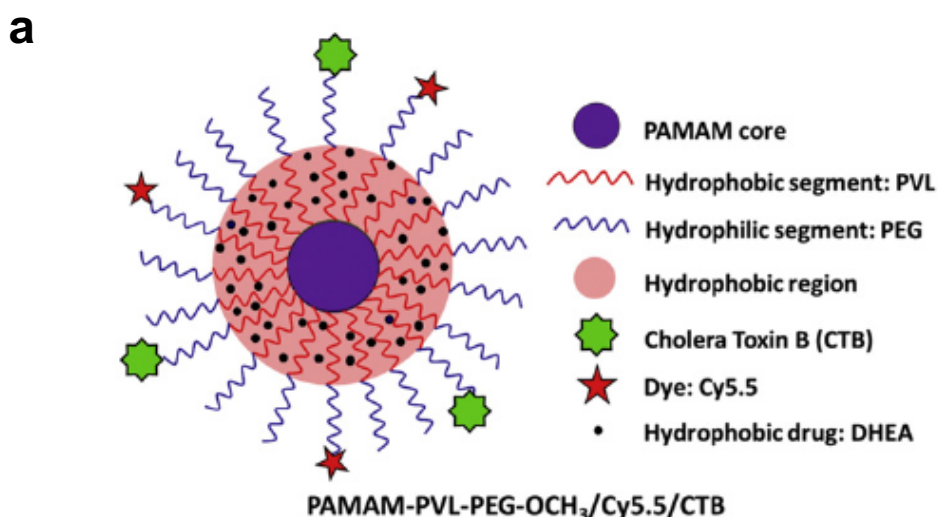
Stimuli-sensitive dendritic core-multishell nanocarriers can be obtained by incorporating sensitive moieties in each segment or by inserting labile linkers at each joint. Yan et al.<sup>[62]</sup> developed a core-multishell system for a glutathione-mediated intracellular drug delivery. The core molecule, a hyperbranched polyester H40, was employed as a macro-initiator for the ring-opening polymerization of L-lactide (LA). Hydrophilic-armed poly(2-Ethoxy-2-oxo-1,3,2-dioxaphospholane) (PEP) were conjugated to the H40-PLA molecules with disulphide linkages (Figure 1-6). Because of its amphiphilic structure, H40-star-PLA-SS-PEP was able to self-assemble into micelles with ca. 70 nm diameters in aqueous solution. Benefiting from the disulphide linkage, the H40-star-PLA-SS-PEP micelles displayed a faster drug release in glutathione-pretreated Hela cells than in non-pretreated cells, which demonstrated the possibility for improved antitumor efficiency of hydrophobic chemotherapeutic drugs.



**Figure 1-6.** Glutathione (GSH) triggered intracellular Dox release from dendritic core-multishell nanocarrier H40-star-PLA-SS-PEP. Figure reprinted from literature.<sup>[60]</sup> Copyright 2011 American Chemical Society.

Based on multiple functional groups on single molecules, multifunctional

nanocarriers can be straightforwardly made from CMS structures. Guo et al.<sup>[63]</sup> developed a retinal ganglion cell (RGCs) targeting system based on multifunctional unimolecular micelles for intraocular drug delivery to prevent RGC loss. Star copolymer poly(amidoamine)–polyvalerolactone–poly(ethylene glycol) (PAMAM–PVL–PEG) was synthesized as the drug delivery platform. The hydrophobic PVL inner shell was able to encapsulate hydrophobic drugs and the hydrophilic PEG shell provided excellent water dispersity. By using difunctionalized PEG, RGC targeting group cholera toxin B domain (CTB) and cy5.5 dye for tracing could be further introduced into the surface of the unimicelle system. The CTB containing group significantly enhanced accumulation and effectively prevent the RGC cells from dying for at least 14 days.



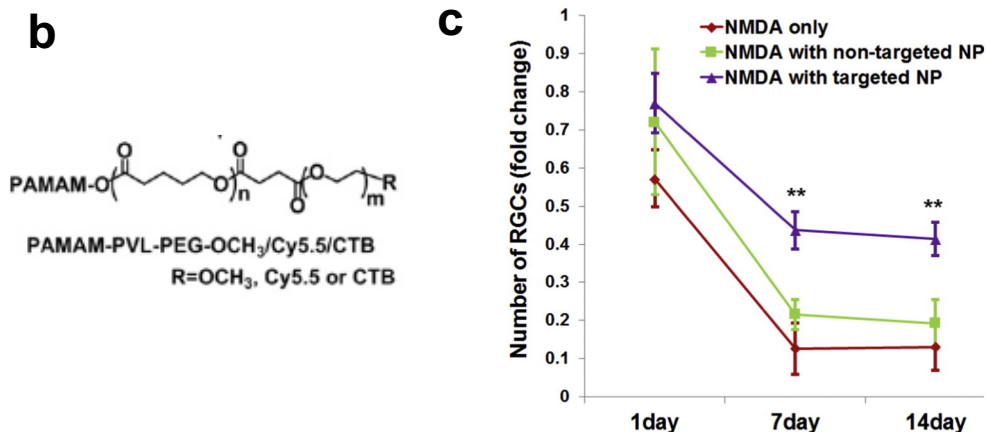


**Figure 1-7.** a) Cartoon illustration of multifunctional unimicelle structure of PAMAM–PVL–PEG–Cy5.5/CTB, with drugs encapsulated in the innershell and targeting groups and dyes on the surface attached. b) Chemical structure of targeted and non-targeted unimicelles. c) The rescue of RGCs by drug loaded unimicelles (NMDA+NPs), compared with the RGCs damaged group (treated with NMDA only)  $n = 7–10$ ,  $**P < 0.01$ . Figure reprinted from literature<sup>[63]</sup> Copyright 2017 Elsevier Science B.V.

Inspired by the polarity variation of liposomes, our group established a type of novel and versatile unimolecular core-multishell (CMS) architecture based on either a PEI<sup>[58b]</sup> or dPG<sup>[60, 64]</sup> core that are conjugated with dense PEGylated alkyl chains as shells (see Figure 1-8). CMS nanocarriers show good solubility in aqueous solution and in most organic solvents. They are able to enhance the solubility of hydrophobic cargos in water and, in contrast, they can also stabilize the hydrophilic cargos in hydrophobic environment. The universal drug loading behavior makes CMS nanocarriers suitable for various biomedical applications. An *in vivo* distribution study showed that dye-loaded CMS were able to selectively accumulate in F9 teratocarcinoma tumor due to the EPR effect.<sup>[57b]</sup> The contrast between tumor and surrounding tissues was significantly increased ( $\sim 3 : 1$ ). Furthermore, it was found that CMS nanoparticles were capable of enhancing different guest molecules to penetrate into a viable skin layer,<sup>[65]</sup> which will be discussed in more detail in Section 1.3. Furthermore these CMS

nanocarriers can be used as templates for *in situ*-forming metal nanoparticles such as platinum, gold, and palladium, which subsequently have been used for catalytic reactions.<sup>[57a, 66]</sup>

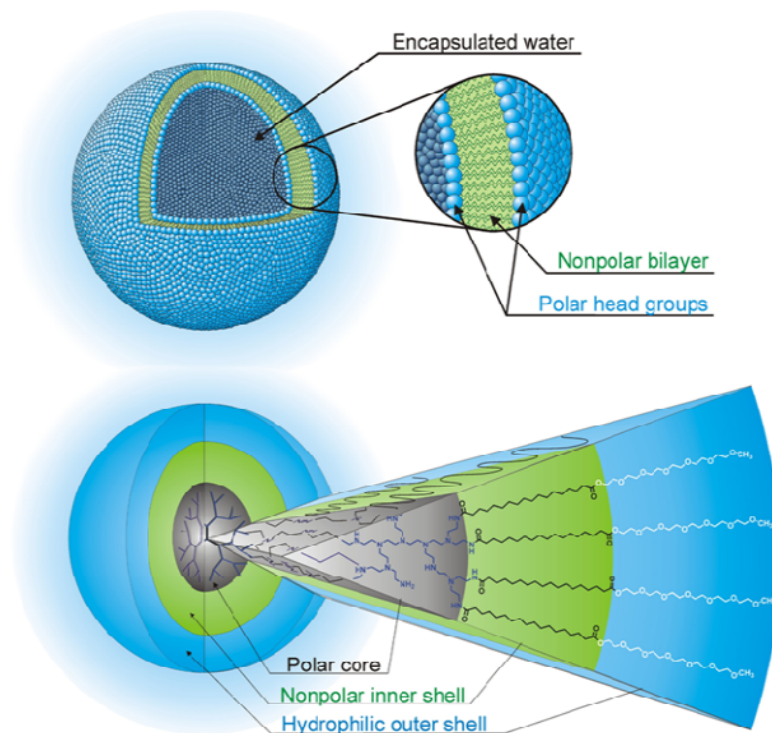


**Figure 1-8.** Cartoon illustration of liposomes (top) and dendritic CMS nanocarriers (bottom) Figure reprinted from the literature<sup>[67]</sup> Copyright 2007 WILEY - VCH Verlag GmbH & Co.

More recently, a pH-responsive core-multishell (CMS) nanocarrier (pH-CMS) was synthesized by introducing an aromatic imine linker between the hydrophobic shell and the hPG core (Figure 1-9).<sup>[68]</sup> The imine linker was relatively stable at pH 7 and rapidly cleaved at pH 5. The DOX-loaded pH-CMS showed higher toxicities than the non-degradable CMS nanocarriers, which might have resulted from a more efficient DOX release caused by the cleavage of the imine bond in the acidic environment within the cellular organelles. Although these CMS nanocarriers have already proven to be



highly versatile, there are still some improvements that need to be made regarding high molecular weight therapeutics loading, controlled release, and long-term toxicity.

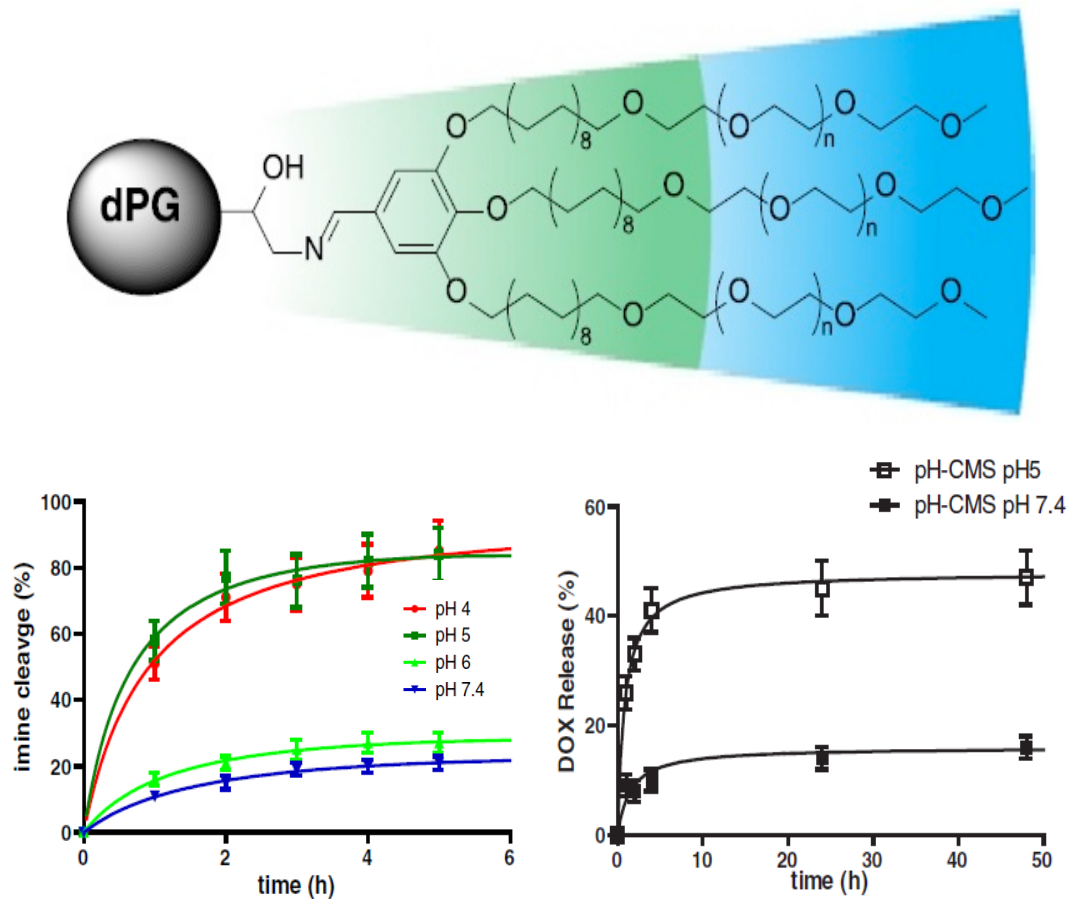


**Figure 1-9.** a) Chemical structure of pH-responsive core–multishell (CMS) nanocarrier, where a pH labile aromatic imine linker was used in between hPG core and mPEG350C18 double shell. b) Cleavage studies of the aromatic imine linker at different pH via  $^1\text{H-NMR}$ ; c) Release kinetics of DOX from pH-responsive CMS nanocarriers at pH 5 and pH 7.4. Figure reprinted from literature<sup>[68]</sup> Copyright 2014 Elsevier Science B.V.

### 1.5 Topical Drug Delivery

Topical drug delivery (TDD) has been considered as a potential alternative to traditional

intravenous and oral drug delivery systems, especially for skin diseases treatment, because of its enhanced therapeutic efficacy as well as high patient compliance.<sup>[69]</sup> The direct application of drugs on the skin can avoid hepatic first-pass metabolism and GI-tract incompatibility and maintain favorable local drug concentrations for prolonged therapeutic effects.<sup>[70]</sup> However, because of its natural function as a barrier for impeding the toxins from the environment from entering body, the skin limits the permeation to a small number of drugs with optimal physicochemical properties (Mw < 500 Da, partition coefficient 1~3).<sup>[71]</sup> Therefore, various TDD systems that can efficiently bypass the skin barrier are greatly interesting for investigations on how to improve the skin penetration of a wide range of drug molecules.

### **1.5.1 Skin Structure**

To overcome the barrier of skin, a comprehensive understanding of skin structures is required. Skin is composed of two distinct layers, epidermis and dermis (Figure 1-10).<sup>[72]</sup> The epidermis can be further subdivided into stratum corneum (SC) and viable epidermis (VE). SC, the outer most and thinnest layer (thickness 10–20  $\mu\text{m}$ ), is the major contributor to the skin barrier function.<sup>[73]</sup> It has a unique hierarchical structure of lipid-enriched matrix with corneocytes embedded, which gives a “brick and mortar” organization.<sup>[74]</sup> Corneocytes, the bricks, are flattened dead cells with crosslinked keratin fibers.<sup>[75]</sup> In human skin, there are about 10 - 20 layers of corneocytes and they are connected by corneodesmosomes, which gives the stratum corneum stability.<sup>[76]</sup> The gaps between corneocytes, about 75 nm both vertically and laterally, are filled with tightly packed lipids.<sup>[77]</sup> The extracellular lipids (mortar) are composed of primarily fatty acids, ceramides, and cholesterol, almost in equal ratios.<sup>[78]</sup> These lipids are able to organize into multiple lamella bilayers and they are less fluidic and permeable compared to most of the other biological membranes based on phospholipid.

The VE layer has multiple cell types and is considered the most biologically active part of skin. In the epidermis, 95% of the cells population are keratinocytes which are responsible for the formation of the self-renewing SC after migrating from the basal layer to the superficial skin.<sup>[79]</sup> Besides keratinocytes, there are also langerhans cells,

dendritic T cells, melanocytes, merkel cells, and so on.<sup>[80]</sup>

Next to the epidermis lies the dermis. The dermis comprised of connective tissues that consist of elastin and collagen fiber networks, which provide the skin's elasticity to support the blood and lymphatic vessels and nerve endings.<sup>[81]</sup> There are also some appendages present on skin, like hair follicles, and sebaceous glands, as well as apocrine and endocrine sweat glands.<sup>[82]</sup>

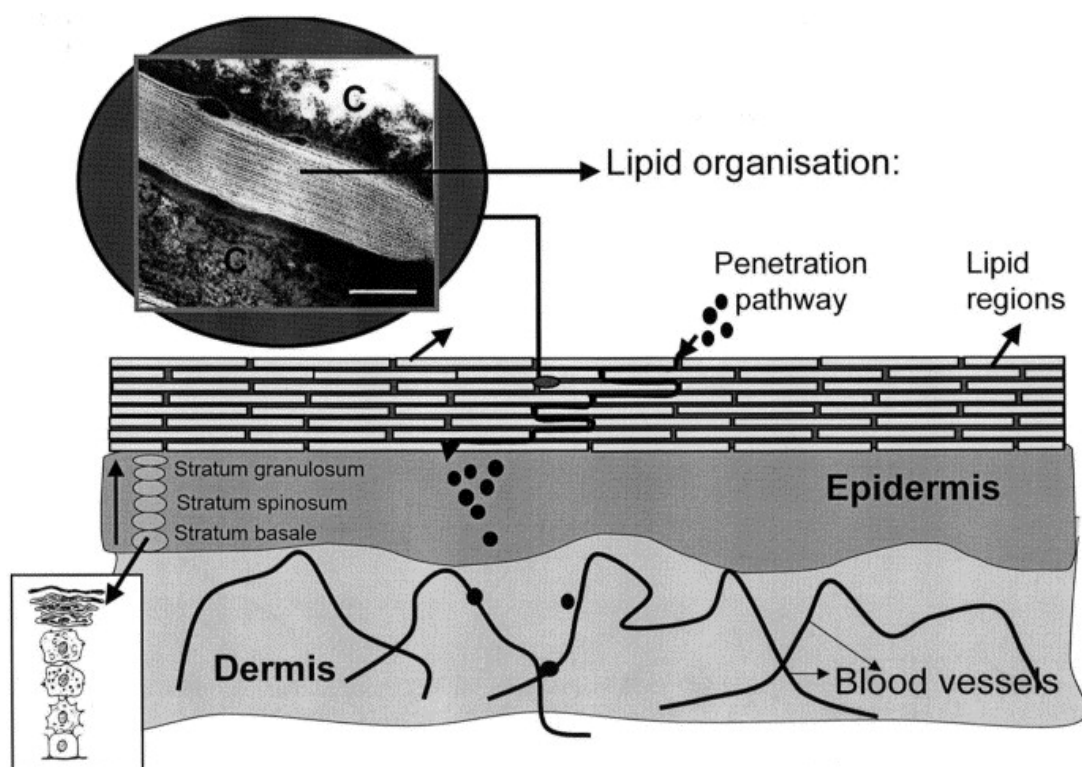


**Figure 1-10.** Cartoon illustration of skin structure. The insertion shows the “brick and mortar” structure in stratum corneum where the corneocytes are embedded in lipid-enriched matrix, C=corneocyte, scale bar=100 nm. Figure is reprinted from literature<sup>[72]</sup>. Copyright 2002 Elsevier Science B.V.

### 1.5.2 Nanoparticulate TDD Systems

Many types of nanoparticles have been reported that enable enhanced penetration of drugs or dyes into skin. The most commonly used types include liposomes,<sup>[83]</sup> solid lipid nanoparticles,<sup>[84]</sup> metal nanoparticles (zinc oxide, titanium dioxide, and gold

nanoparticles),<sup>[85]</sup> polymeric micelles,<sup>[86]</sup> and nanogels.<sup>[87]</sup> TDDSs enhance the diffusion of drugs in skin by altering SC barrier functions via a physicochemical disruption of the SC. They can either act on the polar part by changing the protein conformation on the corneocytes or fluidize the crystalline phase of non-polar lipids. Some TDDSs can work in both ways. The size of these TDDSs are crucial for achieving effective penetration. In general, all but some highly deformable particles sized over 10 nm cannot penetrate into healthy VE but only stay in the SC layer.<sup>[88]</sup> Many studies have pointed out that carriers with a smaller size can diffuse into SC faster and therefore result in a larger amount of skin deposition of encapsulated cargo molecules. Makino et al.<sup>[89]</sup> have studied the size effect of gold nanoparticles on rat skin penetration. The skin penetration experiment demonstrated that the smallest particle (15 nm) showed the highest permeation compared to gold NP particles with 102 and 198 nm, which showed a time lag of 3 h and 6 h, respectively. They found that when the size of the gold NP increased, both the permeability coefficient and diffusion coefficient decreased. Zheng and coworkers<sup>[90]</sup> reported similar results.<sup>[119]</sup> They fabricated curcumin-loaded PLGA nanoparticles with two different sizes (50 and 150 nm) for psoriasis treatment. They found that the drug in 50 nm particles presented a higher penetration into the psoriatic skin and therefore had a better therapeutic effect than with the bigger particles. Surface properties also influences the skin penetration behaviors of carriers. Zhang and coworkers<sup>[91]</sup> have demonstrated the advantage of transactivating transcriptional activator peptide (TAT) functionalized cationic polymeric vesicles for transdermal drug delivery and showed decoration of TAT induced a 2.3-fold and 1.4-fold higher permeation flux of the model drug than the conventional liposome and non-functionalized polymeric vesicles, respectively. Previous studies have shown that TDDS with positive surface charge generally display stronger interactions with SC, which results in a larger amount of carrier deposition and retention in skin than their neutral or negatively charged counterparts. Neutral or negatively charged TDDS, on the other hand, could penetrate deeper and showed a higher permeation rate.<sup>[92]</sup> However, it is hard to say which specifically charged carrier works better enhancing drug

penetration through skin, depending on the individual mechanism of action and also carrier-drug interaction. Many studies have pointed out that the electrostatic interaction between the positively charged liposomes and negatively charged skin surface could enhance the diffusion of drugs<sup>[93]</sup>. Kim et al.<sup>[94]</sup> found cationic flexosome could deliver low-molecular-weight heparin with ten-times higher flux than neutral or anionic counterparts. On the contrary, Hong et al.<sup>[95]</sup> fabricated a series of dendron-based micelles bearing different surface charges. The negative one with the highest drug loading capacity demonstrated a distinguished superiority on enhancing drug penetration. Therefore, the outcome after inclusion of charged groups depending on situation to situation. To summarize the reported information, enhancing material-skin interaction, at the same time, increasing the drug loading capacity could be a way to fabricate high efficient TDDS. In the following part, we will discuss some examples of polymeric nanomaterials as TDDSs.

#### **1.5.2.1 Amphiphilic Linear Block Copolymers**

Amphiphilic block copolymers are the most frequently used materials for enhance the skin penetration of drugs. They can self-assemble into micelles or polymersomes depending on the hydrophilic weight fraction value of the copolymer.<sup>[96]</sup> The most prominent advantage of these block copolymers is their easily tunable hydrophilic-lipophilic balance (HLB), which allows engineering carriers with good drug loading capacity and the desired skin interaction. However, for this kind of carriers, a concentration-dependent assembly-disassembly exists between the aggregates and each individual amphiphile precursor (see Section 1.1).

Kalia et al.<sup>[97]</sup> fabricated polymeric micelles based on biodegradable diblock copolymer methoxypoly(ethylene glycol)-dihexyl-substituted polylactide (mPEG-dihexPLA) for a targeted delivery of tacrolimus (TAC) into the epidermis and upper dermis (Figure 1-11). The high drug loading content ( $23.0 \pm 0.64\%$ ) and long-term stability (over 7 months) indicated that TAC is thermodynamically capable of being encapsulated into mPEG-dihexPLA micelles. Skin permeation experiments showed a 9-fold increase in delivery to porcine skin and a 4-fold improvement with human skin

with the optimized 0.1% micelle formulation, compared to the commercial ointment product Protopic at the same drug concentration.

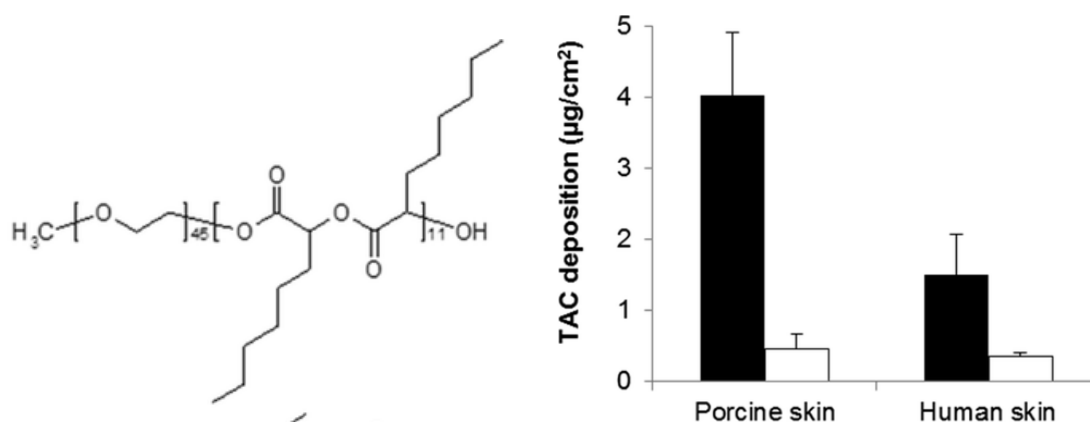


**Figure 1-11.** a) Chemical structure of mPEG-dihexPLA diblock copolymer.; b) tacrolimus accumulation in both porcine and human skin after treatment with micelle formulation (black bar) and Protopic ointment (whitebar) containing the same amount of tacrolimus (0.1% w/w) for 12 hours. Figures reprinted from literature<sup>[97]</sup>. Copyright 2014 American Chemical Society.

### 1.2.2.3 Dendrimers

Dendrimers are treelike-branched polymers with spherical, well-defined chemical structure. Because of the controlled size, multifunctionality, and drug adsorption ability, dendrimers are attractive for a wide range of promising biomedical applications. The most studied dendrimer is poly(amidoamine) (PAMAM) for its potential application in topical drug delivery. Studies have found that the PAMAM and skin interactions are highly size and surface group dependent. Venuganti et al.<sup>[98]</sup> observed the lower generations, for example, G2-NH<sub>2</sub> penetrated faster than the higher ones. G4-NH<sub>2</sub> penetrated better than G3.5-COOH and G4-OH in SC and have proven that cationic dendrimers can alter skin lipids more, thereby reducing skin resistance. The synthesis of dendrimer especially in high generation are complex, instead, Hong et al.<sup>[92]</sup> have developed a PEGylated dendron based micelle (DM) to mimic the structure of

dendrimer (Figure 1-12). Skin penetration experiments showed that all the formulations were effective on enhancing hydrophobic drug penetrating skin. Among them, the delivery flux of the drug by DM with carboxyl surface groups was significantly higher than the one with hydroxyl or amine surface groups, because of the coincidentally high drug loading due to the formation of ion pairs between positively charged drug molecules and negatively charged carriers.

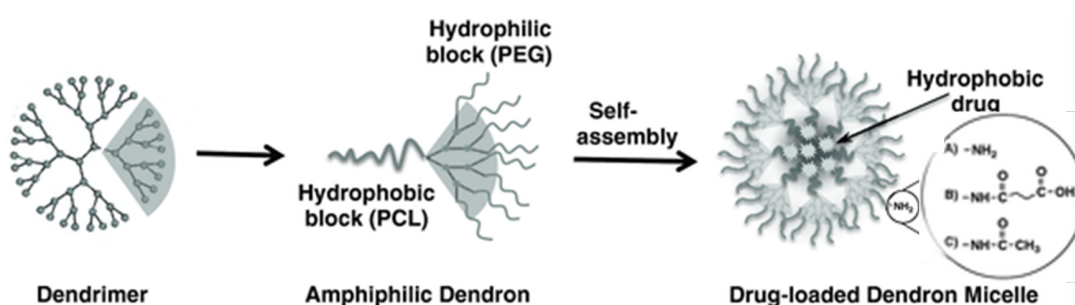


**Figure 1-12.** Structure illustration of micelles assembled from PEGylated dendron-PCL copolymers to mimic the structure of dendrimer. Figures reprinted from literature.<sup>[92]</sup> Copyright 2014 WILEY - VCH Verlag GmbH & Co.

#### 1.2.2.4 Star Polymers

Star polymers represent a type of branched polymer structure, where several linear “arms” surround a branching core. If the arm density is not high enough, star polymers will still self-assemble to form micelles or other structures, similar to linear amphiphiles. However, the reduced CAC very much improves the stability of star polymer assemblies.

Examples of star polymers applied in topical drug delivery are not that often reported. Grayson et al.<sup>[99]</sup> has reported an amphiphilic star copolymer with 6 or 12 arms, which was prepared by directly ATRP of hydrophilic oligo (ethylene glycol)methacrylate and hydrophobic lauryl methacrylate from a bromine-terminated dendrimer core (Figure 1-13). These stars demonstrated improved loading capacity and superiority in the delivery of polar molecules such as rhodamin B through skin,

compared to the 1-arm linear counterpart. The 12-arm star was more efficient than the 6-arm one.

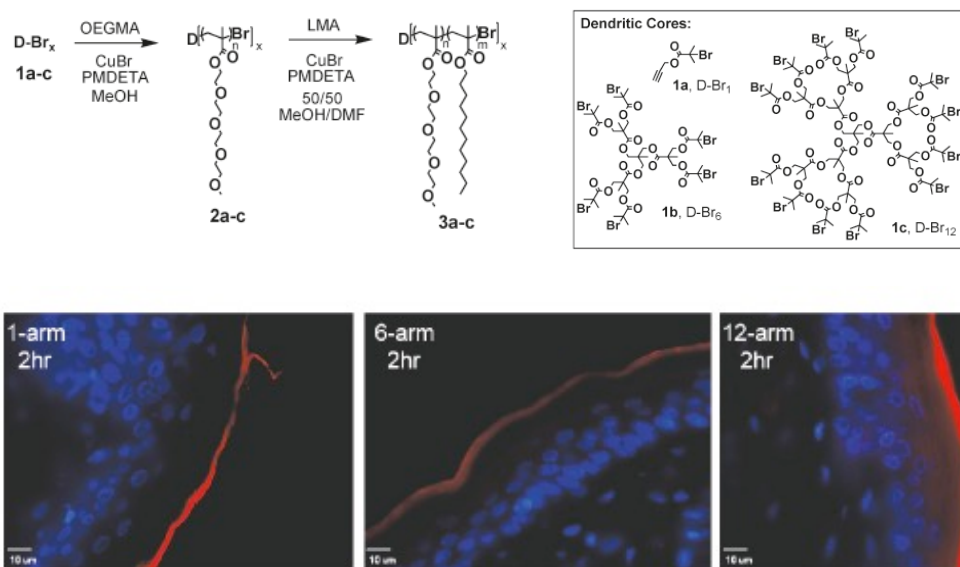


**Figure 1-13.** Synthetic pathway of 1-/6-/12-arms star polymers; fluorescence images of the cross section of porcine skin after application of the star formulations in squalene for delivery of Rohdamine B. Figures reprinted from literature<sup>[99]</sup> Copyright 2011 American Chemical Society.

### 1.2.2.5 Dendritic Core-Multishell Systems

Dendritic core-multishell systems showed the combined advantages of linear amphiphilic polymers, dendrimers, and star polymers. Because of the higher density of the surrounding arms than stars, CMS systems in most of the case can act as “unimicelles,” which is concentration independent. Benefiting from their small size (10 - 20 nm) and flexible structure, dendritic CMS nanocarriers developed in our group have shown significantly more deposition of the various cargos from hydrophilic dye rhodamin B to the anti-inflammatory hydrophobic drug dexamethasone in deep skin layer, compared to other formulations. <sup>[100]</sup> (Figure 1-14) Furthermore, X-ray microscopy gave clear evidence that CMS could target the delivery of dexamethasone



to viable epidermis, whereas the carriers themselves were largely distributed in the lipid lamellae.<sup>[101]</sup> These results demonstrate that CMS nanocarriers are excellent candidates for a safe but effective topical drug delivery.

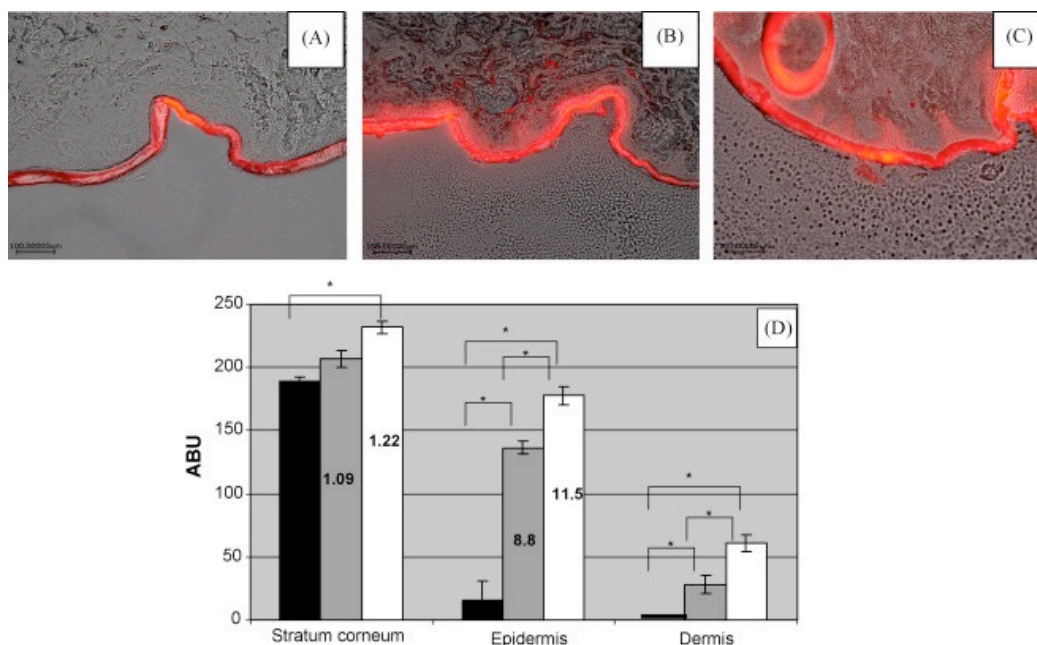


**Figure 1-14.** Cross-section images of porcine skin treated with different Rhodamin B containing formulations for 6 h: 0.004% (w/w) of Rhodamin B loaded (A) base cream, (B) solid lipid nanoparticles, and (C) CMS nanocarriers; (D) the arbitrary pixel brightness values (ABU) in each skin sections via fluorescence images analysis (black bars: cream, grey bars: SLN, white bars: CMS nanocarriers, n = 3). Numbers on the column represent enhancement multiple towards base cream. Figure reprinted from the literature.<sup>[100a]</sup> Copyright 2009 Elsevier B.V.

## Scientific Goals

Because of the natural barrier function of skin, many drugs or other bioactive molecules cannot be delivered to the site of action sufficiently to achieve satisfied therapeutic effects with the conventional formulations via topical administration. The goal of this research is to develop an effective nanocarrier that can overcome the skin barrier and enhance the penetration of bioactive molecules to the site of action.

Polymeric nanocarriers, particularly, dendritic core-multishell (CMS) nanocarriers demonstrate high potential due to their versatility. To further promote its drug loading capacity, especially towards hydrophobic drugs with relatively large molecular size as well as increasing its biocompatibilities, we design and synthesize a degradable CMS with tunable length of inner hydrophobic shell in the first part of our work. The influence of hydrophobicity (or amphiphilicity) on carrier's aggregation behavior, drug encapsulation, release and skin penetration behavior will be discussed in detail. In addition, the skin penetration mechanism and toxicity will be studied.

Protopic, a tacrolimus-containing ointment, has been the only topical formulation of tacrolimus approved by FDA since 2006. It showed a positive clinical outcome in treatment of atopic dermis but could not treat psoriasis. Poor treatment outcomes suggested the ointment formulation was not efficient enough to transport tacrolimus to the skin where the disease is located. In the Chapter 3, our main objective is to formulate tacrolimus stably into the previously optimized CMS nanocarrier and test the in vitro skin penetration, compared to Protopic ointment.

The treatment of skin diseases or wounds is often a combination of processes such as anti-inflammation, anti-bacterial, assisting tissue recovering, scar reducing etc. To realize above mentioned functions at the same time, designing of a platform that can topically deliver payloads with completely different properties such as drugs, proteins, nuclei acid, etc. is necessary. In the final part, the primary objective was to design such a carrier which could transport and release both small hydrophobic drugs but also hydrophilic macromolecules in skin. At the same time, by introducing pH-responsive

moieties, smart nanocarrier will be constructed for on-demand drug release. In addition, the carrier-skin interaction shall be studied to provide an insight into the skin penetration mechanisms.

## Chapter 2. Degradable CMS with Different Hydrophobicity for Efficient Topical Drug Delivery

Part of the opinions have been published in:

F. Du, S. Hönzke, F. Neumann, J. Keilitz, W. Chen, N. Ma, S. Hedtrich, R. Haag, *J.*

*Controlled Release* **2016**, *242*, 42–49

<https://doi.org/10.1016/j.jconrel.2016.06.048>

### Results and Discussion

#### 2.1 Design of hPG-PCL<sub>m</sub>-mPEG CMS Nanocarriers

Polymeric micelles are one of the most promising platforms for topical drug delivery. However, problems including property changes upon drug loading, batch-to-batch quality variation, lack of stability upon dilution or in complex physiological environments, limit their application as a drug carrier. Alternatively, core multishell nanocarriers, where linear amphiphilic copolymers are covalently linked to a dendritic polymer core, have proven to be good candidates that could solve the above-mentioned problems. Previously designed CMS nanocarriers by our group, consisting of a hPG core, C18-alkyl chain inner shell, and mPEG outer shell, allowed the hydrophobic Nile red dye to deeply penetrate viable skin layers.<sup>[102]</sup> However, they lacked the capacity to transport payload with relatively high molecular weights. Moreover, we found that the non-degradable CMS migrated slowly into viable skin layers after being applied on the inflammatory skin model for 24 hours, which might cause toxicity after long-term accumulation.<sup>[103]</sup> Therefore, the CMS nanocarrier has to be biodegradable to avoid accumulation *in vivo* from the perspective of long-term toxicity. Figure 2-1 shows the chemical structure of the CMS nanocarrier we designed. Hyperbranched polyglycerol (hPG) was used as a core because it not only provided multiple functional groups for shell coupling but was also a good skin hydration agent that could help reduce the skin

barrier function. Biodegradable poly( $\epsilon$ -caprolactone) (PCL) was used as the inner shell for hydrophobic drug encapsulation. An easily tunable chain length allowed the encapsulation of payloads with various molecular weights. Ester bonds in the polymer backbone could be also hydrolytically cleaved under physiological conditions. The outer shell was monomethoxypoly(ethylene glycol) (mPEG), which made the whole system dissolve better in water and prevented large aggregates from forming. Each two segments were connected with a ester linker that could be cleaved by enzymes such as esterase, lipase, which are abundant in skin.

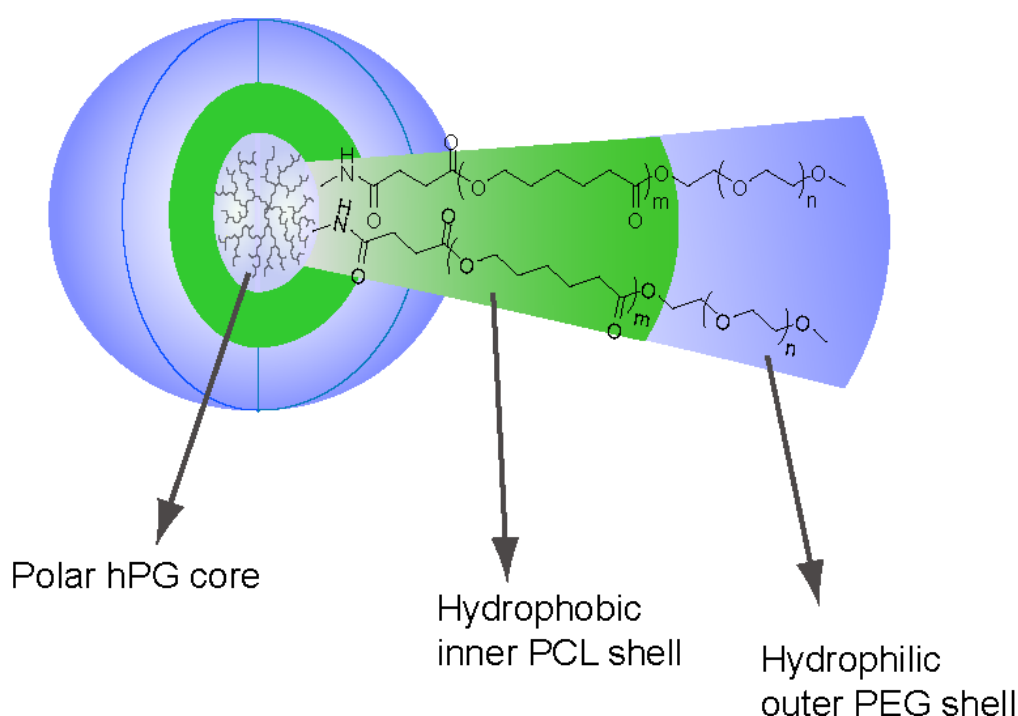
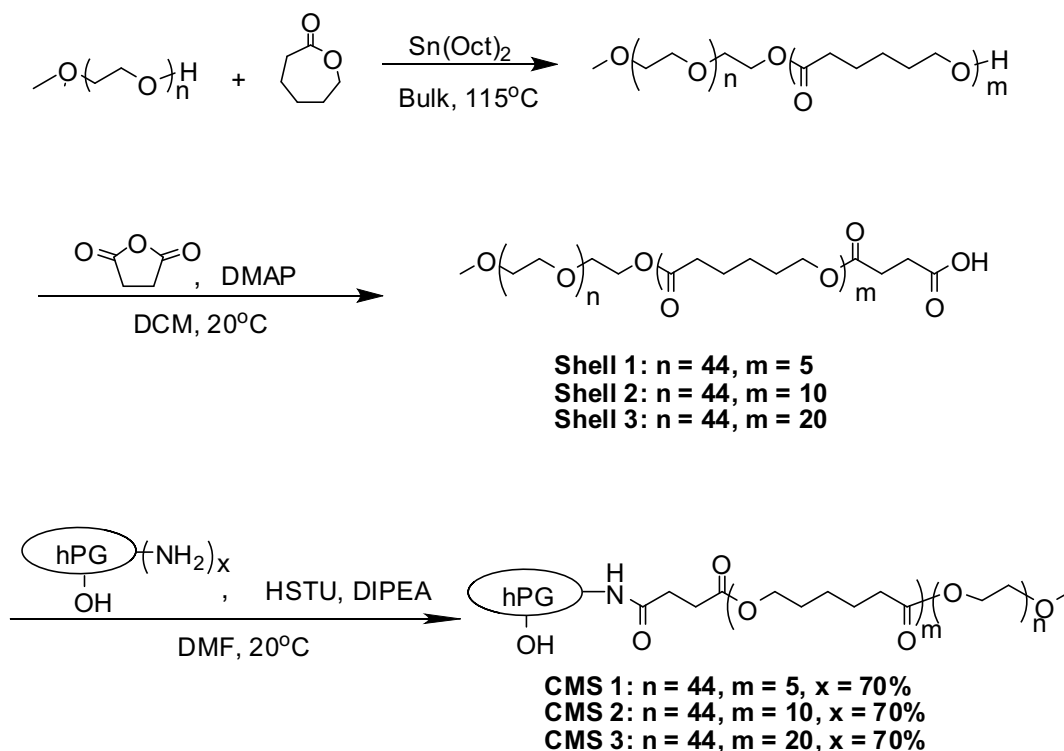


**Figure 2-1.** Structure of biodegradable nanocarriers based on dendritic core-multishell architecture.

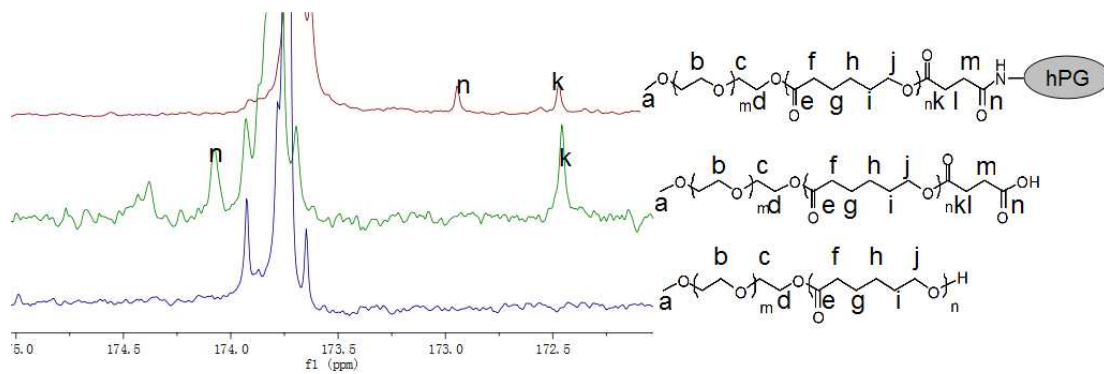
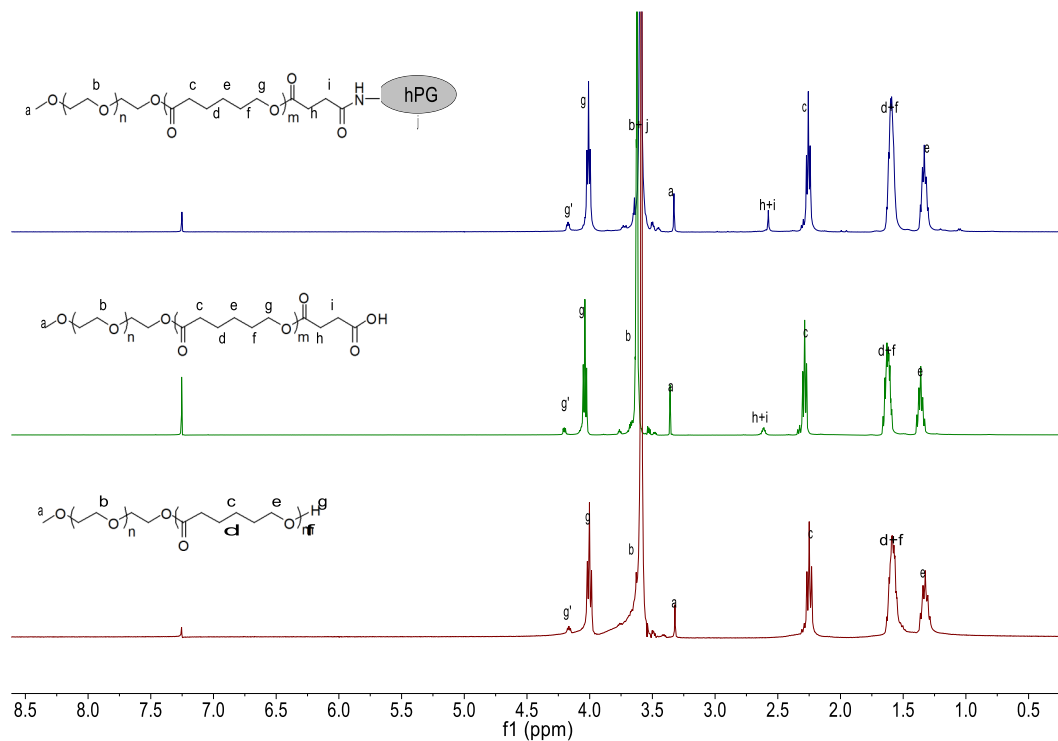
The synthesis was via three steps, including ring-opening polymerization (ROP), succination, and amide-coupling reaction, as shown in Scheme 2-1. The linear block copolymers mPEG-PCL<sub>m</sub>-OH with different polymerization degrees were synthesized via ROP using mPEG as initiator and Sn(Oct)<sub>2</sub> as catalyst.



**Scheme 2-1.** Synthesis steps of biodegradable core multi-shell architectures (CMS) hPG-PCL<sub>m</sub>-mPEG.

From the <sup>1</sup>H NMR spectra (Figure 2-2a), we calculated the number of repeating units in the PCL chains, which were about 5, 10, and 20, respectively. In the next step, the successful succination was confirmed by <sup>1</sup>H-NMR, where a new peak at 2.65 ppm (-COCH<sub>2</sub>CH<sub>2</sub>COOH) appeared. In the final step, carboxylic acid-terminated double shell and amino-terminated hPG core were coupled to form the core-multishell hPG-PCL<sub>m</sub>-mPEG copolymers, which was confirmed by the <sup>13</sup>C-NMR spectra (Figure 2b). The peak at 174.1 ppm originated from the carbonyl group of mPEG-PCL<sub>m</sub>-COOH (-CO-OH) completely shifted to 172.9 ppm, which was assigned to the carbonyl amide (-CONH-) and indicated a successful amide coupling. In FT-IR spectra, the peaks located at 1670 cm<sup>-1</sup> and 1550 cm<sup>-1</sup> attributed to amide band I and band II, respectively, further confirmed the successful synthesis of a hPG-PCL<sub>m</sub>-mPEG core-multishell

copolymer. The average number of conjugated double shells per CMS 1-3 molecule was around 30, calculated according to the molecular weights measured by GPC.



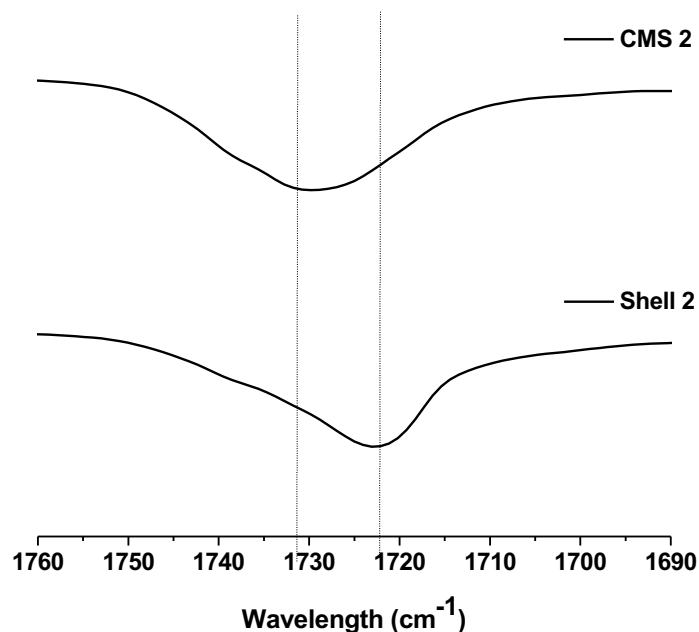


**Figure 2-2.** a).  $^1\text{H-NMR}$  and b)  $^{13}\text{C-NMR}$  spectra of products from each step; c) FT-IR spectra in the range of  $1760\text{-}1690\text{ cm}^{-1}$  showing crystallinity of PCL from the splitting of peak C=O.

DSC results are summarized in Table 2-1. The melting points of the double shell 1-3 were at  $53$ ,  $51$ , and  $46\text{ }^\circ\text{C}$ , respectively. The shells with relatively short PCL chains (shell 1 and 2) had slightly higher melting points, which were mainly attributed to the mPEG segments.<sup>[104]</sup> After the core-shell conjugation, the resulting CMS clearly decreased the melting point to  $43\text{--}48\text{ }^\circ\text{C}$ , which suggested the reduced crystallinity of the CMS nanocarriers compared to their corresponding linear copolymer shells. The reduced crystallinity was further confirmed via a FT-IR spectrometer by monitoring the splitting of peak C=O in PCL backbones. Generally, the bands of amorphous and crystalline phases were located at  $1731$  and  $1723\text{ cm}^{-1}$ , respectively.<sup>[105]</sup> Figure 2-2c showed the FTIR spectra of shell/CMS 2 as an example. In the spectra of CMS 2, the peak intensity at  $1723\text{ cm}^{-1}$  was obviously reduced. On the other hand, the peak at  $1731\text{ cm}^{-1}$  became much stronger compared to the shell, which verified the irregular core



structure of hPG could significantly suppress the crystallization of polyester backbones in the core-multishell architecture.

**Table 2-1.** Characterization of polymers.

Polymer	CL/PEG ratio <sup>a</sup>	$M_n$ (g/mol) ( $\times 10^3$ ) <sup>b</sup>	$M_w$ (g/mol) ( $\times 10^3$ )	PDI ( $M_w/M_n$ )	Arm density (mol <sub>Shell</sub> / mol <sub>CMS</sub> ) <sup>c</sup>	$T_m$ °C	Size <sup>d</sup>	
							$D_h$ (nm) H <sub>2</sub> O	$D_h$ (nm) THF
hPG-NH <sub>2</sub>	-	9.8	17	1.73	-	-	5.5 ± 1.2	-
Shell 1	5	3.4	3.8	1.11	-	53.2	11.8 ± 0.7	1.6 ± 0.4
Shell 2	10	4.4	4.9	1.14	-	51.7	13.7 ± 1.1	1.4 ± 0.7
Shell 3	20	5.5	6.2	1.12	-	46.4	17.9 ± 1.1	2.5 ± 1.3
CMS 1	5	113.7	176.9	1.55	31	47.6	18.4 ± 1.3	16.7 ± 1.4
CMS 2	10	139.3	198.5	1.42	30	48.3	21.9 ± 0.2	15.2 ± 0.5
CMS 3	20	185.5	337.9	1.82	32	43.1	36 ± 6.3	16.8 ± 2.6

<sup>a</sup> The CL/PEG ratios were calculated from <sup>1</sup>H NMR integrals.

<sup>b</sup> Molecular weight and polydispersity index of hPG-NH<sub>2</sub> were measured by GPC in water, and the others were measured in DMF.

<sup>c</sup> The arm densities were calculated based on the equation  $(M_{n(CMS)} - M_{n(hPG)})/M_{n(Shell)}$ .

<sup>d</sup> The hydrodynamic diameter ( $D_h$ ) is given based on the volume distribution. The values represent the maximum of the distribution and the mean standard deviation (n=3).

## 2.2. Self-Aggregation Properties of hPG-PCL<sub>m</sub>-mPEG

Table 2-1 summarizes the sizes of all the copolymers in different solvents measured by DLS, which can give a hint about their multi/uni-molecular aggregation behavior. The size increased, as expected, regardless if they were CMS nanocarriers or the assembled micelles from double-shells by varying the PCL length from 5 to 20 units. Each CMS nanocarrier generally had a larger hydrodynamic size than its corresponding double shell, because of the additional hPG core that was around 5 nm and also the less compact micellar structure. Meanwhile, we have recorded the size of all the polymers also in THF, which is a good solvent for all of these polymers. The CMS nanocarriers could maintain their structures' integrity in THF and showed sizes around 15 - 17 nm. All the double shells disassembled; only single chains (1 - 2 nm) were observed. These

results verified the covalently interconnected structures of the CMS nanocarriers. Notably, the hydrodynamic size of CMS 1 and CMS 2 was very close in size to THF, suggesting that both carriers mainly existed as unimolecular particles in aqueous solution. In the meantime, the hydrodynamic size of CMS 3 (36 nm) was almost two times larger than it was in THF (16.8 nm), which suggested small multi-molecular clusters formed in the aqueous solution. Cryo-TEM image of CMS 2 (Figure 2-3) revealed the presence of monodispersed spherical nanoparticles with diameters ca. 15 nm, which was slightly smaller than the size determined by DLS, probably because of the poor contrast of the PEG outer shell. Based on the above results, we concluded that the uni-/multi-molecular aggregation behavior of CMS carriers could be controlled by varying the Mw ratio of hydrophilic and hydrophobic segments. Many previous studies have found that smaller sized nanocarriers tend to penetrate skin faster. Therefore, maintaining the unimolecular size of CMS nanocarrier might be advantageous.

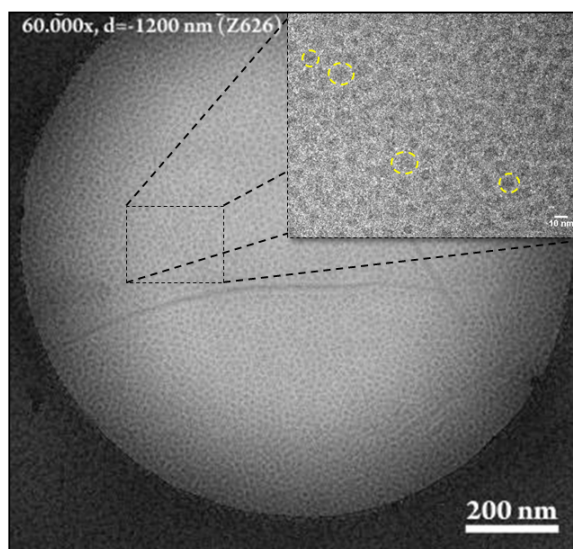


**Figure 2-3.** Cryo-TEM image of CMS 2 in aqueous solution at concentration of 5 mg/mL; The scale bar of the magnified view is 10 nm.

### 2.3. Encapsulation Studies

Dexamethasone, a steroidal anti-inflammatory drug, was used as a model drug for the encapsulation studies. Table 2-2 summarizes the drug-loading capacities (LC) and

encapsulation efficiencies (EE) of all the carriers. Both the LC and EE improved with carriers that had longer PCL chains, which demonstrated that the drug was mainly solvated in the hydrophobic pocket surrounded by the PCL chains. It is noteworthy that a significant increase of LC and EE by CMS nanocarriers was observed, more than the respective linear double shells even though they had the same PCL chain length. For example, a 23% increase of LC was obtained after shell 1 converted to CMS 1. The same for CMS 2 and CMS 3, 60% and 39% increases in LC were obtained, respectively, which signified that dendritic CMS carriers had much higher drug loading capacity than the corresponding linear amphiphilic copolymers. The remarkable improvement on loading capacity by CMS probably was due to their less crystallized hydrophobic phases that could provide more space for drug accommodation. Notably, all the sizes of CMS decreased to different degrees after dexamethasone loading. This phenomenon in the case of CMS 3 was the most obvious, which almost resulted in a 2-fold smaller size than its original. It is possible that the drug could break the multi-molecular CMS aggregates down into unimers during the capsulation process by inserting themselves into the PCL chains, thereby preventing the PCL chains from intermolecular interaction. A similar phenomenon was also reported by another study where pyrene was loaded as a probe into dendritic copolymers.<sup>[106]</sup> On the other hand, drug loading induced a dramatic increase in size for all the shells that were observed except shell 1 which had a very poor drug-loading capacity.

**Table 2-2.** Characterization of drug loaded CMS.

polymer	LC (wt%) <sup>a</sup>	LC (mol <sub>drug</sub> /mol <sub>carrier</sub> )	EE (%)	$D_h$ <sup>b</sup> (nm)
Shell 1	1.3	0.113	13.4	12.2 ± 0.9
Shell 2	1.5	0.169	14.8	80.1 ± 5.7
Shell 3	2.3	0.3	23.0	125.6 ± 49.1
CMS 1	1.6	4.6	15.8	19.0 ± 1.0
CMS 2	2.4	10	23.6	17.2 ± 0.3
CMS 3	3.2	15.2	32.2	19.9 ± 0.2

<sup>a</sup> The drug loading capacity was calculated based on equation  $LC \text{ wt}\% = W_{\text{loaded drug}} / W_{\text{polymer}} \times 100$ , note: Free Dexa amount in water has been deducted during calculation, which is 51  $\mu\text{g/ml}$  by measuring a blank sample via HPLC.

<sup>b</sup> The hydrodynamic diameter ( $D_h$ ) is given based on the volume distribution. The values represent the maximum of the distribution and the mean standard deviation (n=3).

## 2.4. Drug Release Study

Cumulative release profiles of dexamethasone from CMS 1-3 were assessed by using the dialysis method in PBS (pH 7.4) at 37 °C. The release occurred following a biphasic profile, as shown in Figure 2-4. Burst release of dexamethasone within initial 4 h was observed from all the three CMS nanocarriers followed by a sustained release until a plateau was achieved. CMS 1 showed the fastest release rate, with 87% of drug released in first 2 hours. In the same period, the drug release amount from CMS 2 and 3 was 57% and 53%, respectively. The burst release might be attributed to the large surface area-to-volume ratio of CMS nanocarrier that could facilitate drug diffusion. We know that relatively fast drug release in SC allows a quick and sufficient drug accumulation at the disease site for therapeutic reaction.<sup>[107]</sup> However, it also suggests the interaction between the carrier (especially the hydrophobic segments) and dexamethasone was not strong enough so that drug leaking could happen in the liquid formulation during storage, especially for carriers with short PCL chains. This problem should be addressed in the future study.

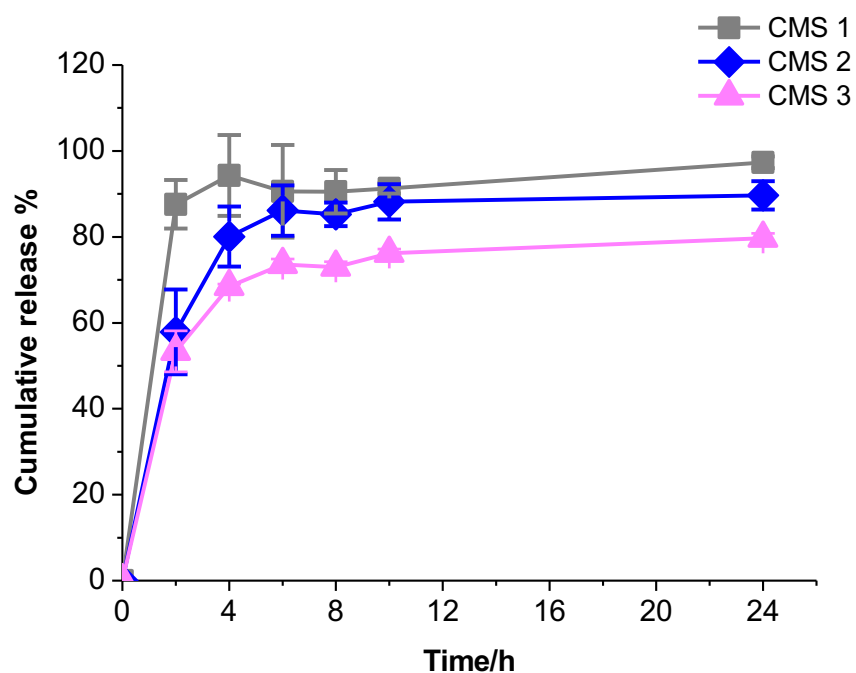


**Figure 2-4.** Release profile of Dexamethasone from CMS nanocarriers. (CMS 1: grey; CMS 2: blue; CMS 3: pink).

## 2.5. Skin Penetration

Nile red was loaded as a probe into the CMS nanocarriers for skin penetration studies. An oil-in-water base cream with the same amount of Nile red was used as a control. The fluorescence microscopy images of the cross-sections of intact human skin after treatment for 6 h with all the formulations are shown in Figure 2-5a. With the conventional base cream, the observed weak red signals from Nile red were mainly located in the SC layer. Intensive Nile red signals, which diminished from the SC to the deep skin layers, were observed for all the tested CMS nanocarriers. The amounts of Nile red in each skin sections were quantified by reading the pixel brightness, as shown in Figure 2-5b. CMS nanocarriers induced a 3- to 4-fold higher amount of Nile red that accumulated in SC and dermis layer. A 4- to 7-fold higher amount was found in the VE layer compared to the base cream, which indicated the CMS nanocarriers were much more efficient than the base cream on drug delivery through skin. To have a close comparison of the three CMS nanocarriers, the CMS 2 with the medium PCL chain

length was superior, which was probably related to its small unimolecular size and proper hydrophobicity. The smaller size allowed a faster diffusion in skin. Proper hydrophobicity determines the interaction power between carriers and skin surface. CMS 3 had a significantly larger size (~ 36 nm) and CMS 1 was probably not hydrophobic enough to effectively interact with skin lipid, therefore it could not enhance Nile red penetration as well as CMS 2.

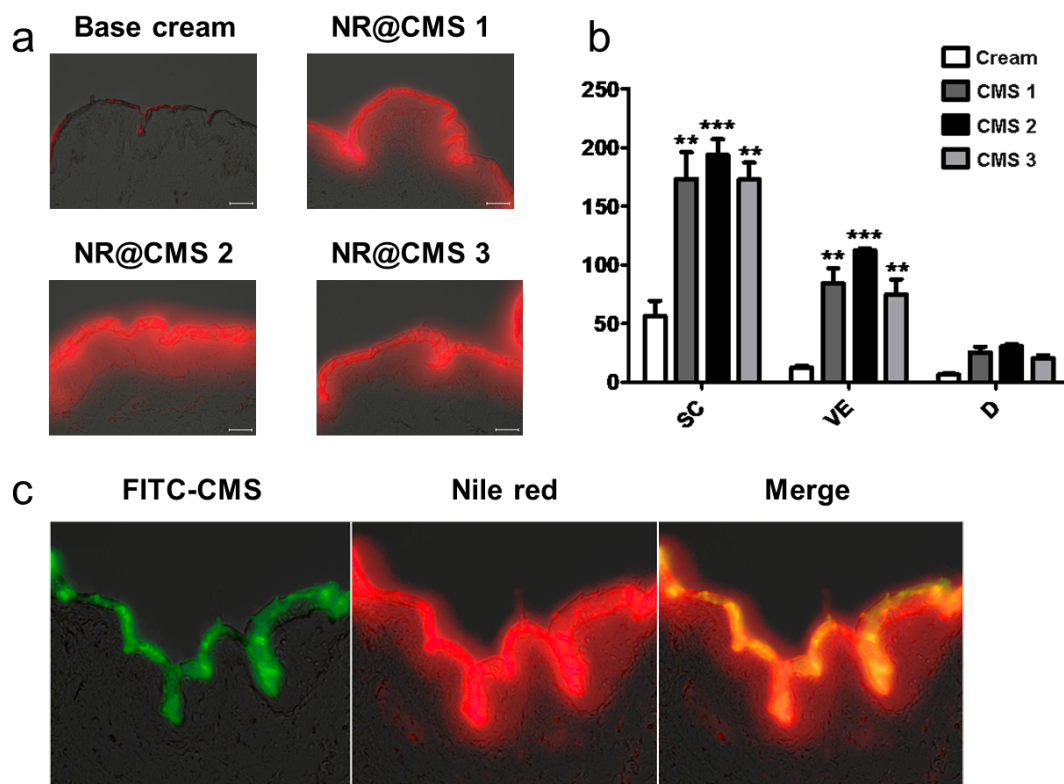


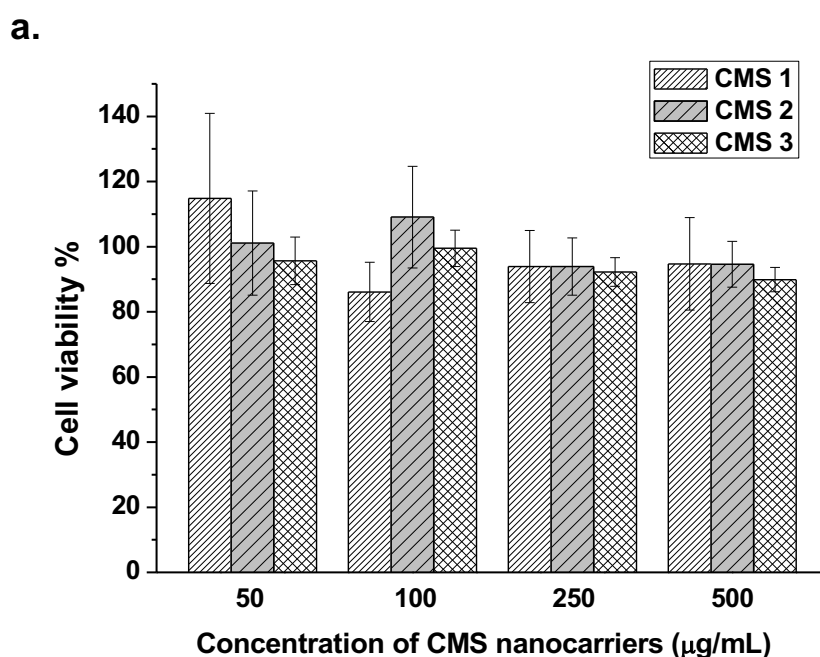
**Figure 2-5.** a) Visualization of skin penetration behaviors of Nile red loaded CMS nanocarriers (NR@CMS1-3), compared to commercial cream in human skin; b) Quantified Nile red amounts in different skin layers (SC: stratum corneum; VE: viable epidermis; D: dermis); c) Skin penetration of NR@FITC-CMS 2, observed in FITC and Nile red channel, respectively. The scale bar is 100  $\mu$ m.

In order to see how CMS nanocarriers enhanced the Nile red penetration into skin, we tested Nile red penetration again with FITC-labeled CMS 2, as shown in Fig. 2-5c.

As observed before, Nile red signals faded again from the SC layer into the deep epidermis layers, whereas the FITC signals were only from the SC layers. From this result, we could confirm that the CMS nanocarriers themselves could not cross SC to deep skin layers, however, they could transport the Nile red through the SC, where Nile red was released and further diffused to the epidermis and upper dermis.

## 2.6. Cytotoxicity

Since nanocarriers could have exposed themselves to viable skin cells, we studied the cytotoxicity of the CMS nanocarriers using MTT and RTCA assays. MTT (Fig. 2-6a) results showed above 90% cell viability after 24 h incubation with all the three CMS nanocarriers, even at concentrations up to 500  $\mu\text{g/ml}$ . We further used RTCA to confirm the cytotoxicity by monitoring the real time cell index (RTCA) value in presence of CMS nanocarriers incubation. As shown in Figure 2-6b, a reduction of the CI values with CMS nanocarriers incubation was not observed compared to the one without any treatment during the two-day measurement. These results indicated that CMS nanocarriers showed very good biocompatibilities.



**b.**

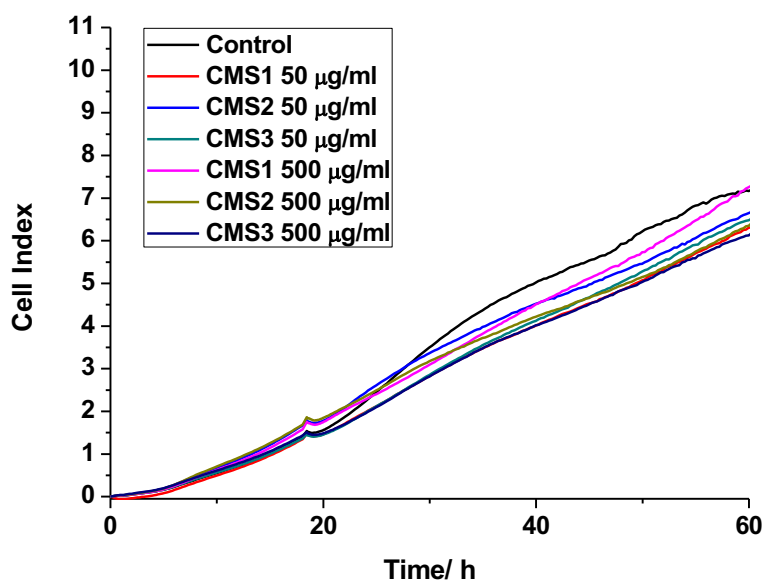


**Figure 2-6.** a) Cell viability of HaCat cells determined by MTT assay for 24 h (n=3). The cell viability of untreated control was set to be 100%; b) cytotoxicity measured by real time cell index analysis (RTCA);

## 2.7 Cellular Uptake

The cellular uptake of CMS-FITC nanocarriers towards HaCaT cells was studied with confocal microscopy. To have an idea how intensive the uptake by HaCaT cells was, we also tested the uptake towards macrophages as a positive control. As shown in Figure 2-7, the CMS signals could be already detected in macrophages at 4 hours incubation; the signals became very intensive with a prolonged incubation time up till 24 h. In contrast, hardly any CMS signals could be detected after 4-hours incubation and, even with 24-hours incubation, limited CMS was detected intracellularly, which meant the internalization of CMS nanocarriers towards the HaCaT cells was unfavorable. It was probably due to the neutral surface charge and a high PEG density coverage on the surface of CMS. The low cellular uptake of CMS might explain the low cytotoxicity we found before. Meanwhile it can also be a hint that penetration of the CMS nanocarriers was unfavorable by the transcellular route because of the low



affinity between the CMS nanocarriers and the surface of keratinocytes.

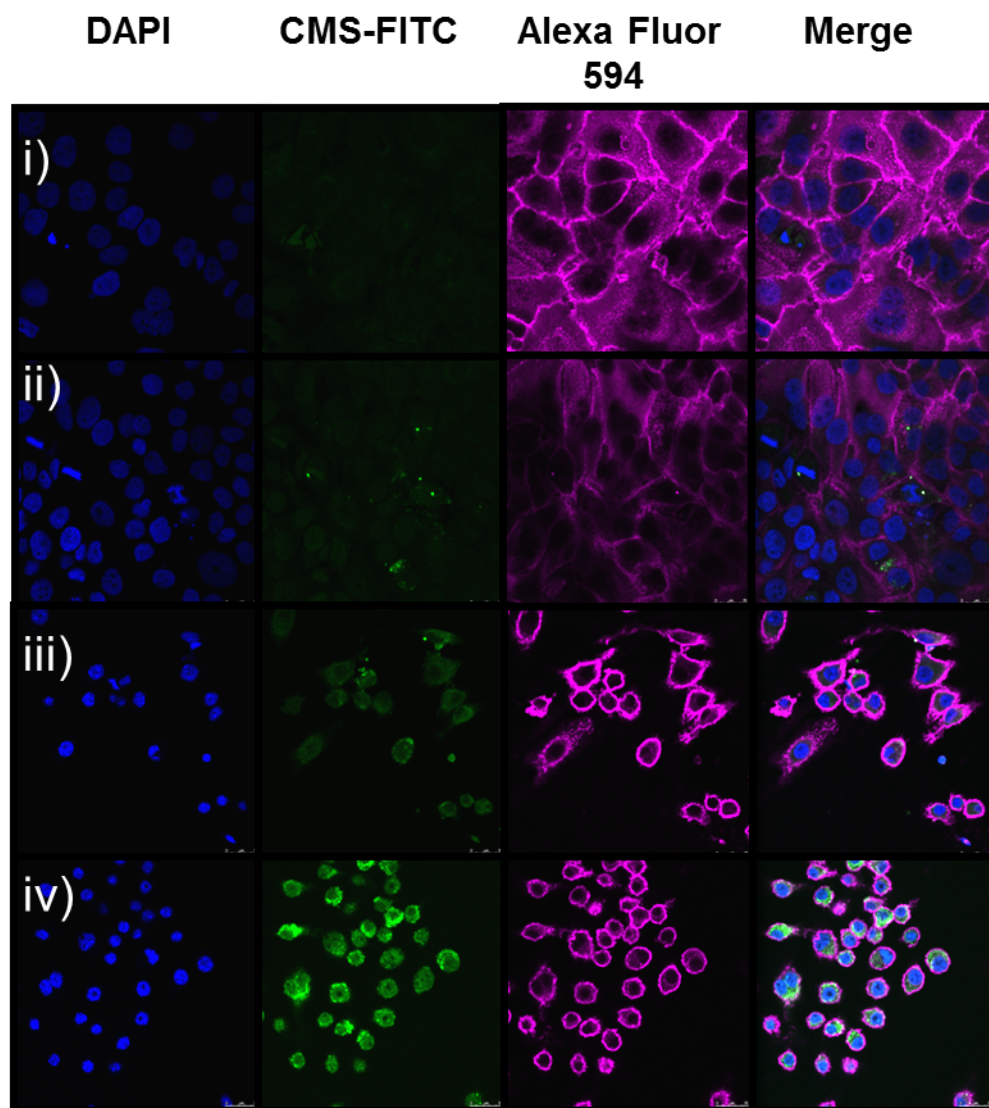


**Figure 2-7.** Cellular uptake study of CMS 2 towards HaCat cells (keratinocytes) after 4h (i), 24h (ii) and towards macrophages after 4h (iii), 24h (iv).

## 2.8 Bovine Corneal Opacity and Permeability (BCOP) Test

The BCOP test was performed to assess the irritation potential of CMS, whereby ethanol and TiO<sub>2</sub> nanoparticles were selected as a positive control which could induce irritation effects on different levels as previously reported.<sup>[108]</sup> Normally, when the *in*

*vitro* irritation score (IVIS) of the tested agent was less than 3, it could be classified to the non-irritation category. An IVIS beyond 55 means the substance could induce severe eye damage. As shown in Figure 2-8, the IVIS values for ethanol and TiO<sub>2</sub> nanoparticles were respectively 118 and 27, which means they were located in the range that could induce severe and slight eye irritation. The IVIS from the CMS nanocarrier was below 3 and could therefore be concluded that it did not have an irritating potential on body tissue.

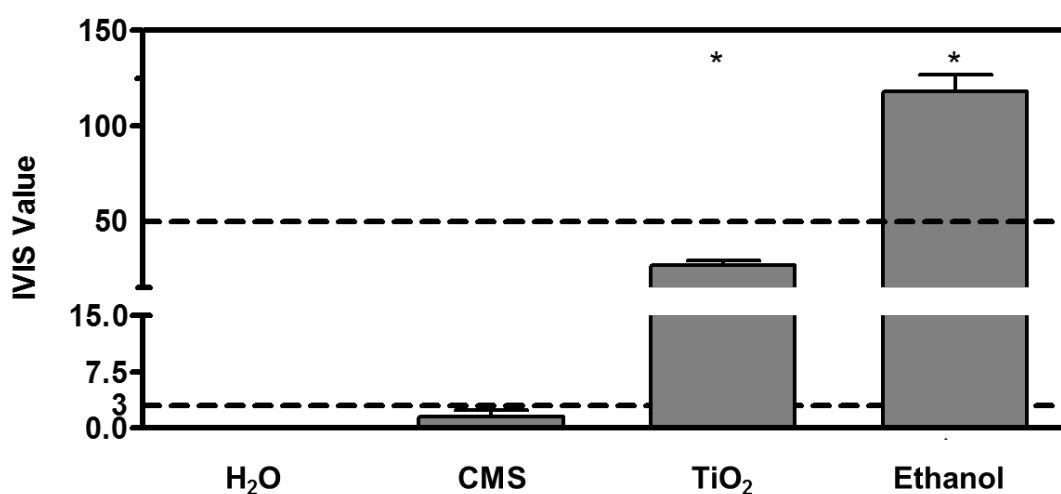


**Figure 2-8.** Eye irritation potential of CMS nanocarriers at the concentration of 5mg/mL via BCOP assay. Mean ± SEM, n= 3.

## Conclusion

In summary, biodegradable CMS nanocarriers were designed and synthesized. The fabrication of CMS nanocarriers with different parameters was straightforward, which allows an easy scaling up. CMS nanocarriers showed the combined advantages of excellent stability and improved drug-loading capacity over their corresponding linear counterpart. By increasing the length of PCL chain from 5 to 20 units, the drug-loading capacity of CMS nanocarriers increased. All the three CMS nanocarriers in this study had hydro diameters in the range of 18-36 nm. The small size and amphiphilicity benefited the interaction of CMS with horn layer and thus resulted in a remarkably

enhanced skin penetration of Nile red. The unfavorable internalization of the CMS nanocarriers towards keratinocytes suggested that they entered the SC most likely by the intercellular lipid pathway (Figure. 2-9). The penetration of CMS nanocarriers themselves into viable skin layers was not found for at least 6 hours incubation. Moreover, they showed little toxicity against keratinocytes for all the tested concentrations and no irritations to bovine eyes, which suggested that they could be safely used for topical drug delivery.

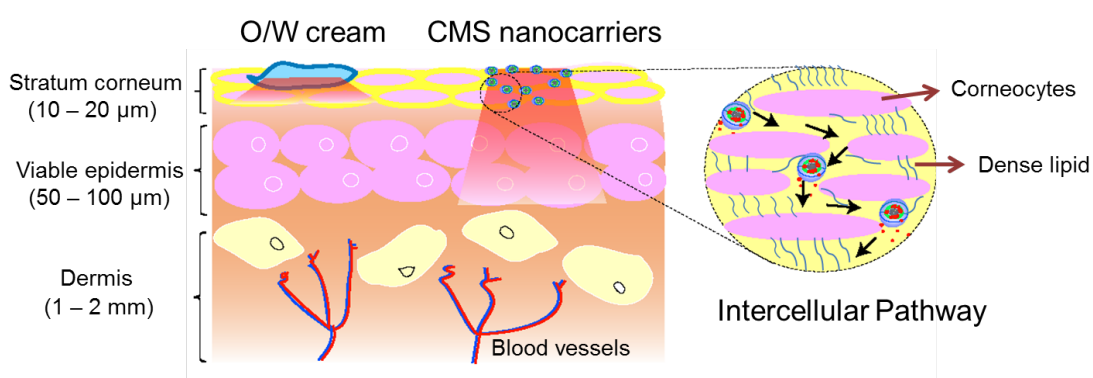


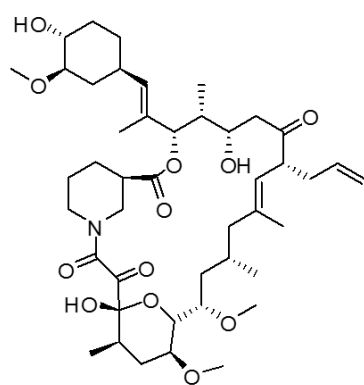
**Figure. 2-9.** The suggested penetration enhancement mechanism: Large amount of cargo was transported by CMS into skin by interacting with skin lipids. The released cargo penetrated into deep skin layers and CMS itself stays at superficial stratum corneum layer of skin.

# Chapter 3. Skin Penetration of Tacrolimus-containing CMS Formulations

## Results and Discussion

### 3.1 Comparison of Different Drug Loading Methods

CMS nanocarriers, although they showed significantly better drug loading capacity than the linear block copolymers, the drug loading efficiency was still relatively low. Different encapsulation methods were first screened to efficiently encapsulate Tacrolimus with a relatively high molecular weight ( $M_w$  804 g/mol) (Figure 3-1a). Here we compared the results of drug loading from three common methods, as shown in Figure 3-1b. Miniemulsion was the most efficient way to achieve the highest tacrolimus encapsulation efficiency (93%), almost 18-fold higher than the stirring method. Even though the sonification method was also quite efficient (85%), precipitation occurred from that sample after only 1-day storage. Whereas, the sample containing a higher tacrolimus amount made with the miniemulsion method could be stably stored for several weeks.



**Tacrolimus**  
 $M_w$ : 804.0 Da  
Log P: 5.28

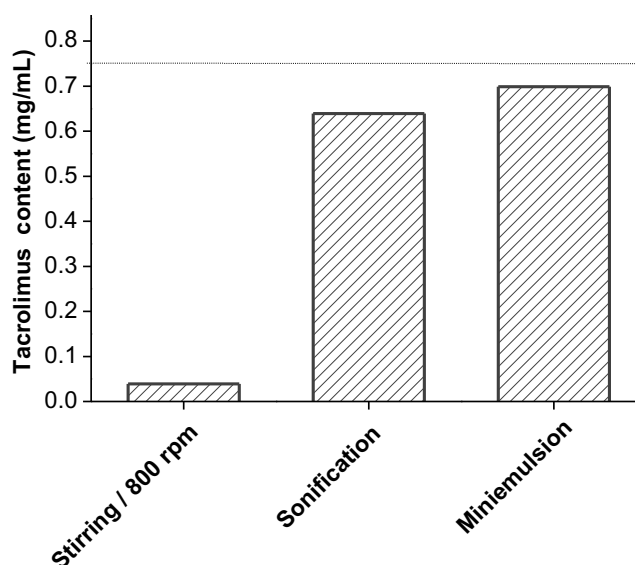


**Figure 3-1.** a). Chemical structure and physicochemical properties of Tacrolimus; b) Encapsulated Tacrolimus amount in 5 mg CMS nanocarriers in 1 mL of H<sub>2</sub>O via different drug loading methods measured by HPLC; the dash line represents the total amount of tacrolimus for each encapsulation study.

### 3.2 Formulation Preparation with Different Tacrolimus Contents

Afterwards, we prepared a series of formulations with different tacrolimus amounts using the miniemulsion method. The tacrolimus loading capacity (LC), actual content, and encapsulation efficiency (EE) are summarized in Table 3-1. The highest LC and EE was achieved when the drug-to-carrier ratio was set at 15%, whereby the loaded concentration of tacrolimus was 0.70 mg/mL, 58-fold higher than its natural solubility (0.012 mg/mL). Below this ratio, almost all the feed drug could be encapsulated into CMS 2 solution. In order to compare with Protopic, CMS formulation with the same amount of tacrolimus (0.03 % w/w) was prepared for the following study. Its size and stability were monitored via DLS, as shown in Figure 3-2. The tacrolimus loaded CMS displayed an average size ca. 28 nm after one-day preparation and negligible change in the size over 17 days demonstrated good stability of the tacrolimus-containing CMS formulation.

**Table 3-1.** Preparation of formulations containing different amount of tacrolimus.

Entry	C <sub>CMS 2</sub> mg/mL	Theoretical LC wt%	Actual LC wt%	C <sub>drug</sub> mg/mL	EE%
1	5	10	9.9	0.50	99.5
2	5	15	13.9	0.70	92.9
3	5	20	14.25	0.71	71.3
4	5	30	10.18	0.51	33.9

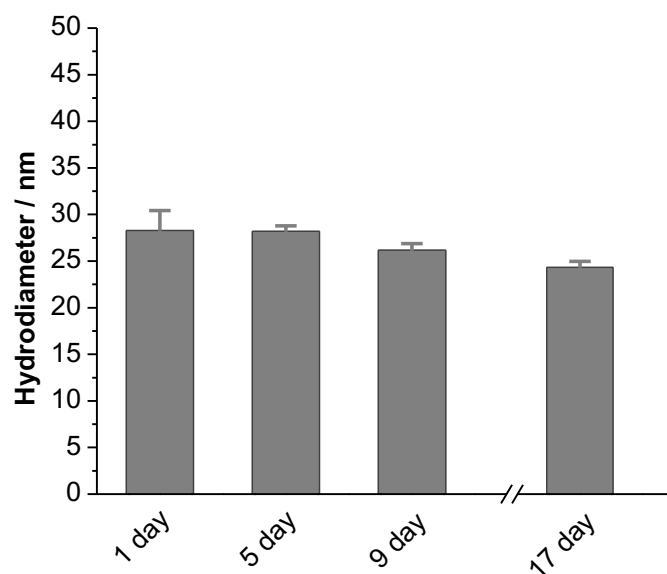


**Figure 3-2.** The size change of CMS formulation containing 0.03 % tacrolimus over time monitored via DLS.

### 3.3 Release Study

The release of tacrolimus from CMS 2 was monitored over 168 h in PBS (pH 7.4) at 32 °C by the dialysis method. As shown in Figure 3-3, a sustained release profile was obtained, where around 30% of tacrolimus was released from the nanocarrier within 168 h. No burst release at the initial stage indicated that tacrolimus was stably encapsulated in the inner part of CMS. On the other hand, we should keep in mind that a too strong affinity between drug and carrier might also have hindered the drug's further penetration into deep skin layers.

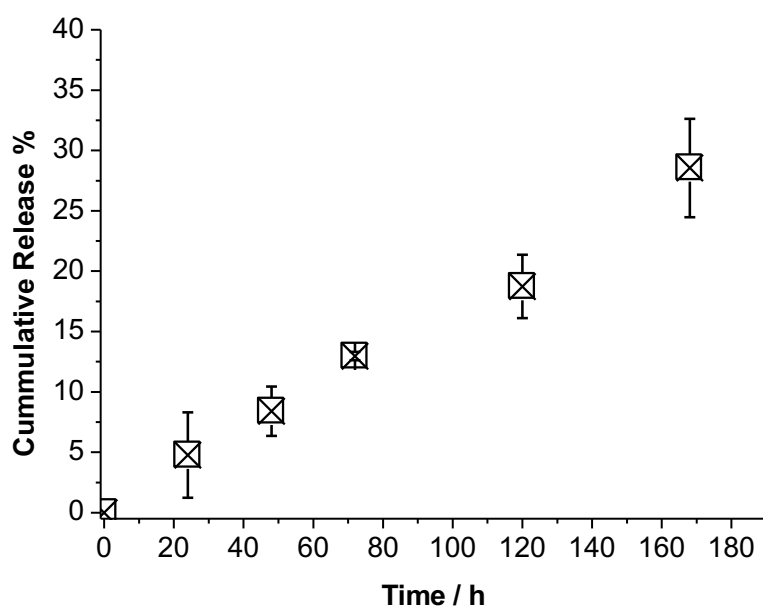


**Figure 3-3.** Release profile of tacrolimus from CMS nanocarrier in PBS (pH 7.4) at 32 °C.

### 3.4 *In vitro* Skin Penetration of Tacrolimus-Containing Formulations

Penetration experiments of CMS and Protopic formulation containing the same amount of tacrolimus (0.03% w/w) were carried out on freshly received human skin from operations at two different time points. As shown in Figure 3-4, the tacrolimus amount delivered by the CMS formulation to each skin layer was significantly higher than the Protopic. Especially in the SC and VE, the deposited tacrolimus amount was 6-fold higher than Protopic at 24 hours treatment and the gap was further increased with 48 hours treatment. The significantly increase of the deposited drug amount induced by prolonging incubation time, on the other hand, indicated there was still room to improve the affinity between CMS and skin surface, because 48-hour continuous treatment was not realistic from a clinical perspective. Taking a close look at the drug distribution after 48 hours treatment, however, we found most of the tacrolimus from the CMS-treated sample located in the SC layer (ca. 70% of the skin-deposited amount) and only ~ 30% of tacrolimus was successfully delivered to VE and dermis layer where it was supposed to perform. A comparison of these numbers to another published result, where a

polymeric micelle based on amphiphilic block copolymer showed the target ratio (drug amount in VE and dermis layer divided by total skin deposition amount) for topical tacrolimus delivery as high as 70%, the off-target ratio in our case was relatively high, most likely due to the slow release of drug from the CMS carrier as previously discussed. Based on above results, designing improved nanocarriers with fast interaction with skin and efficient release could be an interesting direction to work on in the future.

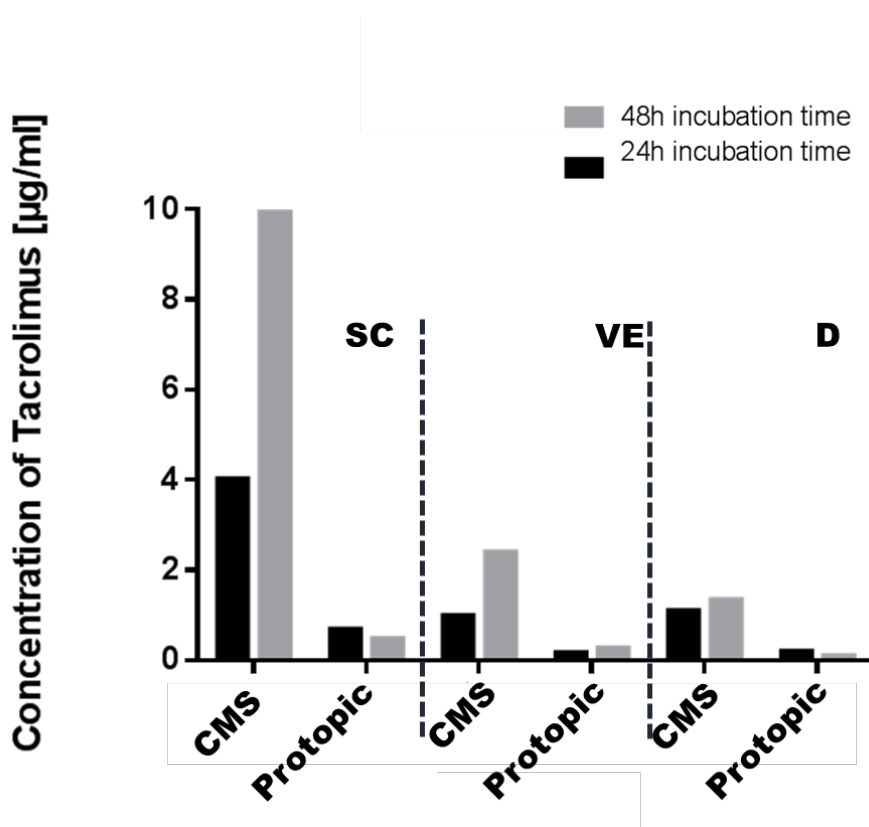


**Figure 3-4.** Deposition amount of Tacrolimus in each skin layer (SC: stratum corneum; VE: viable epidermis; D: dermis) delivered by CMS and Protopic ointment after 24 and 48 hours application on intact fresh received human skin.

## Conclusion



We have successfully prepared a stable, tacrolimus-loaded CMS formulation that has comparable tacrolimus content with the commercial product Protopic. The bioavailability of tacrolimus was significantly enhanced by the CMS nanocarrier, which demonstrated its great potential as a topical vehicle for treatment of inflammatory disease like psoriasis. On the other hand, only 30% of the tacrolimus delivered by CMS had reached VE and dermis layer where the sites of action supposed to be and the rest were all deposited in the SC layer, perhaps because of the slow release of tacrolimus from the CMS carriers, which needs to be improved in future studies.

## **Chapter 4. Cationic CMS as Potential Platform for Topical Multi-payloads Delivery.**

### **Results and Discussion**

#### **4.1. Design of Core-multishell Unimicellar Systems**

Previous studies have shown that CMS nanocarriers could efficiently facilitate the diffusion of hydrophobic drugs/dyes into skin due to its small size and proper amphiphilicity. However, its lack of capacity for delivering macromolecules limited its application field as topical drug carrier. Herein, we designed and synthesized a CMS decorated with lipocationic DEA moieties in the innershell (CMS-DEA). DEA is a small molecule containing a tertiary amino group, which is slightly protonated at neutral pH (pH 7.4) and completely protonated at acidic pH (pH 5.5). The protonation-deprotonation process results in a polarity change of the polymer backbone, which can be used as trigger drug release. Moreover, introducing of the cationic moieties enables the CMS carrier to efficiently bind to macromolecules especially those bearing negative charge. Additionally, a number of studies have shown that positively charged carrier is more efficiently than neutrally or negatively charged carriers on topical drug delivery because of the strong electrostatic interactions with skin.

Using charged, especially cationic materials as building blocks to synthesis TDDs is still a subject of debate. The most important problem associated with cationic carriers is the toxicity. To avoid this problem, precisely tuning the DEA composition is necessary to achieve good biocompatibility. Furthermore, the biodegradable polymer backbone facilitates elimination of materials, which improves its safety as TDDs. The chemical structures of both the cationic CMS carrier was shown in Figure 4-1. For comparison, we also synthesized CMS carrier without charge groups (CMS-PCL).

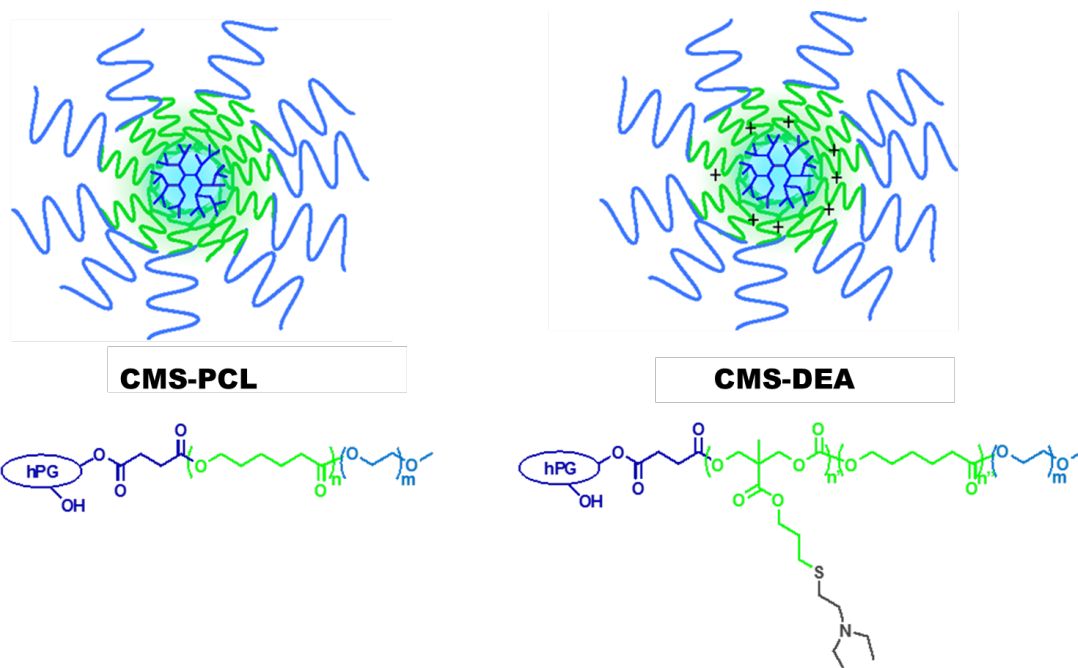
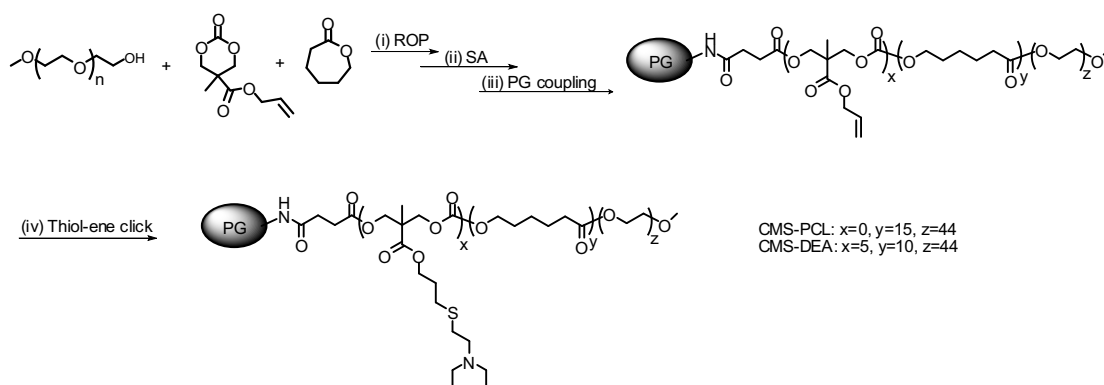


**Figure 4-1.** Structures of CMS without charged units CMS-PCL and CMS with lipocationic tertiary amino groups CMS-DEA.

The synthetic pathways of CMS carriers were shown in Scheme 4-1. CMS-PCL was prepared by a classic three-step protocol. First, we did a ring-opening polymerization of  $\epsilon$ -caprolactone using PEG as a macroinitiator in the presence of  $\text{Sn}(\text{Oct})_2$  catalyst to yield amphiphilic block copolymer mPEG-PCL, a so-called double shell. By reacting with an excess amount of SA, the terminal hydroxy group of the double shell was then converted into carboxyl group, which could further react with the aminated hPG core to produce a CMS-PCL copolymer. In order to introduce DEA, we needed to think about a strategy to synthesize a functional polyester inner shell. Successful ROP of amine-bearing lactones by the common used catalysts are rarely reported. Alternatively, copolymerization of CL monomer with other functional monomers such as cyclic carbonates, followed by post-functionalization, could be a very straightforward strategy. MAC, a commercial allyl-bearing cyclic carbonate was chosen, which allowed easy post-functionalization with a wide range of molecules containing thiol groups via a highly efficient thiol-ene addition reaction. Conversion of the comonomers was determined by  $^1\text{H-NMR}$  analysis at different time points during

the polymerization (Figure 4-2a/b). Although a higher consumption rate of CL than MAC was observed, the difference was not all that significant, which indicated a random copolymer that was produced via tin-catalyzed ROP. The number of repeating units of MAC and CL in each double shell, which was around 5 and 10, calculated from the  $^1\text{H-NMR}$  was quite in line with the feeding ratio. After the amide coupling, the produced allyl-functionalized CMS architecture was further modified with DEA via thiol-ene click reaction. In the  $^1\text{H NMR}$  spectra (Figure 4-2c), peaks that originated from the vinyl group at 5.25 - 5.35 ppm and 5.85 - 5.95 ppm almost disappeared. At the same time, new peaks at 1.9 and 2.6 - 2.8 ppm showed up which indicated the successful modification of DEA on CMS. The conversion of double bond was estimated to be 90% according to the  $^1\text{H-NMR}$  spectra. Further structure information about CMS nanocarriers were summarized in Table 4-1.



**Scheme 4-1.** Synthetic pathway of CMS nanocarriers: (i)  $\text{Sn}(\text{Oct})_2$ , bulk,  $110^\circ\text{C}$ , 16 h; (ii) succinic anhydride (SA), DMAP, THF, r.t., 48h; (iii) PG- $\text{NH}_2$  (DF=15%), HSTU, DIPEA, DMF, r.t., 4 days; (iv) DMPA, DEA, THF/ $\text{H}_2\text{O}$ , 4 h.

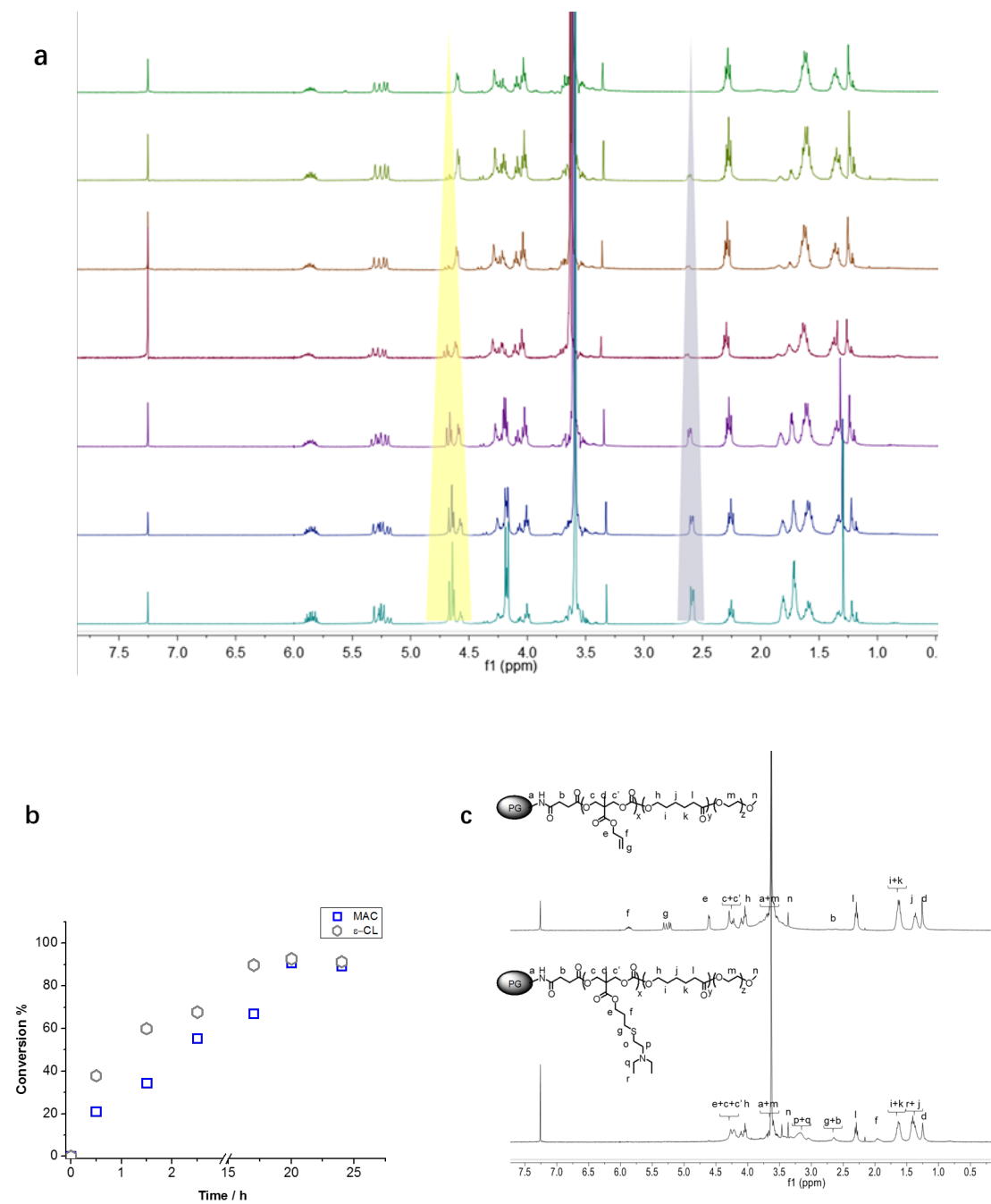


**Figure 4-2.** a)  $^1\text{H-NMR}$  spectra of reaction mixture during copolymerization at different time points; b) the conversion of comonomers against time; c)  $^1\text{H-NMR}$  spectra of CMS-MAC and CMS-DEA.

## 4.2. Aggregation Properties of CMS

The multi/uni-molecular aggregation behaviors of CMS were then studied by a size comparison measured by dynamic light scattering (DLS) in different solvent systems

(Milli Q and THF). THF was chosen because it was a medium polar solvent, which could solubilize well both the polar and non-polar parts of CMS. Therefore, the size determined in THF was thought to be close to the size of a single molecule. All the results of the measurements are summarized in Table 4-1. The size of CMS-PCL in aqueous solution was 2-fold larger than its size in THF, which indicated some small clusters consisting of two or three molecules might have formed. The size for CMS-DEA was constant in both solvent systems, so we concluded that it mostly existed as unimolecular micelles in MilliQ-water.

**Table 4-1** Characterization of polymers.

Polymer	PEG:CL :DEA <sup>a</sup>	Number of arms <sup>b</sup>	$M_n$ <sup>c</sup> (kDa)	PDI ( $M_w/M_n$ )	Size <sup>d</sup>	
					$D$ (nm) H <sub>2</sub> O	$D$ (nm) THF
hPG-NH <sub>2</sub>	-	-	5.0	1.49	2.4 ± 1.5	-
CMS-PCL	1:15:0	5.3	51.4	1.4	30.8 ± 1.6	10.8 ± 1.8
CMS-DEA	1:10:5	6.0	55.7	1.5	13.4 ± 0.3	10.7 ± 0.6

<sup>a</sup>The ratio of PEG:CL:DEA were calculated from <sup>1</sup>H-NMR integrals.

<sup>b</sup>The number of arms were calculated from <sup>1</sup>H-NMR integrals

<sup>c</sup> Molecular weight and polydispersity index of CMS-PCL was measured in DMF by GPC, and the others were measured in water.

<sup>d</sup>The diameter ( $D$ ) is given based on the volume distribution. The values represent the maximum of the distribution and the mean standard deviation

Cryo-TEM observations displayed the spherical nanoparticles with an average diameter of ~12 nm for CMS-DEA and slightly bigger size for CMS-PCL ca. 20 nm (Figure 4-3 a,b), which were in agreement with the DLS results. The size and zeta potential of both CMS nanocarriers in aqueous solutions were further monitored at different pH, as shown in Figure 4-3c,d. In acidic pH 5.5 - 6.5 (pH of skin surface),

CMS-DEA displayed a single molecular size  $\sim 13$  nm and a positive charge 10 mV. When increasing the pH value to slightly basic range (pH 7.4 - 8), the positive charge gradually disappeared to 0 mV and the size of CMS-DEA grew to 22 nm, which indicated the charge played an important role in preventing CMS from self-packing intermolecularly. In the case of CMS-PCL, pH had a negligible influence on both size and zeta potential when the error bar had been taken into consideration.

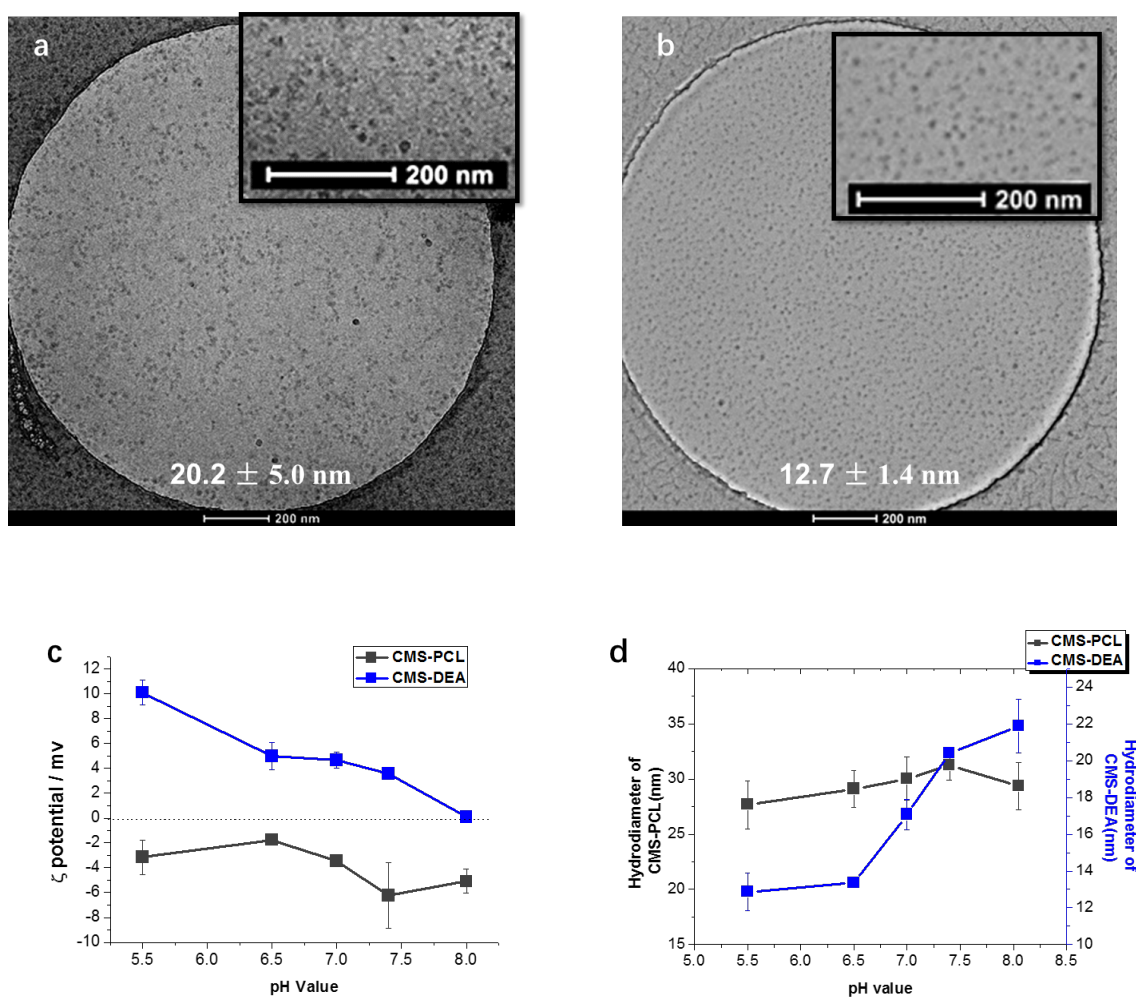


**Figure 4-3.** Cryo-TEM of CMS-PCL a) and CMS-DEA b) nanocarriers at 3 mg/mL; The scale bar is 200 nm. The inserted numbers were the average size of 30 arbitrary particles; Changes of zeta potential c) and size d) of CMS-PCL (black) and CMS-DEA (blue) in PB buffer (10 mM) with different pH value.

### 4.3. Encapsulation and Release Studies

The anti-inflammatory drug tacrolimus was selected as a model for the encapsulation studies. Tacrolimus is a hydrophobic drug with molecular weight 804 Dalton and partition coefficient logP 5.28 (predicted by ChemAxon MarvinView 17.24). Its physiochemical properties were far out of the favorable range, which indicate low skin penetration on its own. The drug was loaded into CMS carriers by using miniemulsion method. As shown in Table 4-2, efficient drug loading for both carriers were obtained. CMS-DEA displayed higher drug loading capacity (14 wt%) than CMS-PCL (10 wt%), probably because the additional lipocationic side groups could reduce the crystallinity of the polyester chains to afford more space for drug accommodation. Besides, tacrolimus was a relatively polar molecule with 3 H-bond donors and 11 H-bond accepters. Inserting tertiary amino side groups could slightly increase the polarity of the inner shell, which led to better solubilization of tacrolimus. After drug loading, sizes of both carriers were slightly increased, demonstrating some small aggregate formed. FITC-BSA was selected as an example of biomacromolecule to test the binding capacity of both CMS nanocarriers. As a result of combination of electrostatic interaction and hydrophobic interaction, CMS-DEA showed higher binding capacity than CMS-PCL which also showed good binding capacity mainly because of the hydrophobic interaction.



**Table 4-2.** Characterization of Tacrolimus-CMS and BSA-CMS nanocarriers

Polymer	Tacrolimus loading			BSA loading		
	LC <sup>a</sup> wt%	LC (mol/mol)	Size	BC <sup>b</sup> wt%	BC (mol/mol)	Size
CMS-DEA	14	9.0	29 ± 12	75.6	0.64	14.3 ± 0.9
CMS-PCL	10	7.0	41 ± 10	66.3	0.52	29.7 ± 2.4

<sup>a</sup> The drug loading capacity was calculated based on equation  $LC \text{ wt}\% = W_{\text{loaded drug}} / W_{\text{polymer}} \times 100$ ;  $LC \text{ (mol/mol)} = N_{\text{loaded drug}} / N_{\text{polymer}}$ .

<sup>b</sup> The protein binding capacity was calculated based on equation  $BC \text{ wt}\% = W_{\text{bind protein}} / W_{\text{polymer}} \times 100$ ;  $BC \text{ (mol/mol)} = N_{\text{bind protein}} / N_{\text{polymer}}$ .

The release of tacrolimus was investigated under different pH values (Figure 4-4). Almost linear release profiles were obtained in all the systems, demonstrating the release of Tacrolimus was mainly driven by diffusion. No initial burst release was observed in any case, demonstrating good stability of tacrolimus loaded CMS nanocarrier. At pH 7.4, tacrolimus was slowly released from CMS-DEA with 29% released amount in 78 h. Due to further increased polarity of the inner shell after the complete protonation of tertiary amino groups, an accelerated drug release was observed from CMS-DEA at acidic pH, which showed 69% drug release within 78 h. In the meanwhile, the release profile of CMS-PCL at acidic pH was similar as it under neutral condition. The slower release rate at pH 7.4 (storage condition) and higher drug loading capacity revealed that tacrolimus was thermodynamically more likely to be encapsulated into CMS-DEA than CMS-PCL. The pH responsive release property of CMS-DEA enables it a smart drug carrier which can stably encapsulate drugs during storage and release them on demand.

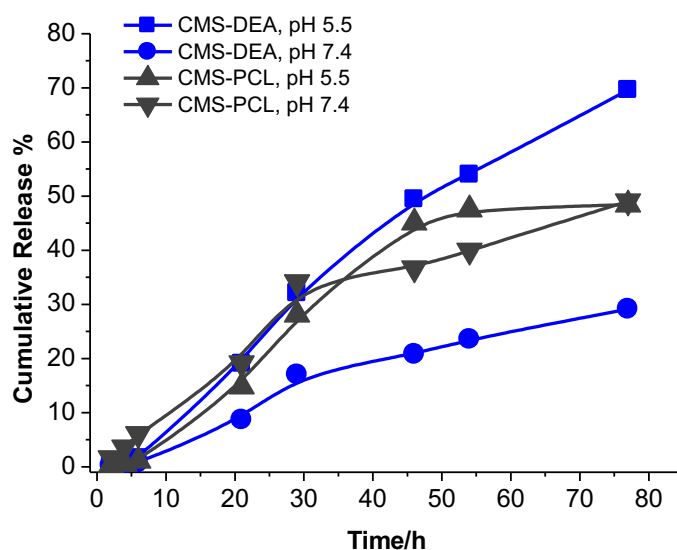


**Figure 4-4.** Release of tacrolimus from CMS-PCL (grey) and CMS-DEA (blue) in buffer solutions with different pH.

#### 4.4. QCM-D Study on Interactions between CMS and SC Model

Natural SC lipids consist of three major components, namely, ceramides, cholesterol, and free fatty acids, which are almost equimolarly contributed. By mimicking the natural SC structure, we built a SC model onto a quartz crystal with gold electrodes via a published method.<sup>[109]</sup> Shifts of frequency ( $\Delta f$ ) and dissipation ( $\Delta D$ ) after CMS absorbed on SC are shown in Figure 4-5a,b. The drops in frequency in both cases indicated that both CMS were attached to the SC lipids and no changes of  $\Delta f$  were observed after water rinsing, indicated that the attachment of CMS to SC is irreversible. Interestingly, the kinetics as shown were clearly different. A sudden decrease in frequency and rapidly achieved saturation after the CMS-DEA solution pumped in, compared to the stepwise decrease manner in the case of CMS-PCL, demonstrated a much faster attachment of CMS-DEA to skin lipids, which was probably driven by strong electrostatic force. To evaluate the interaction in more detail,  $\Delta D$  was plotted as against  $\Delta f$ , as shown in Figure 4-5c. In the initial phase, the slope from CMS-DEA curve was much smaller than from CMS-PCL, which pointed out a higher density and more compact film formed with CMS-DEA when the added mass was the same,

demonstrating CMS-DEA probably flattened after deposited on the skin lipids (Figure 4-5d). In the second phase of the curve from CMS-DEA, the slope was close to zero, demonstrating a very rigid nearly saturated film was formed so that additional mass didn't cause any shifts on the dissipation.<sup>[110]</sup> The final larger adsorption amount and less compact film formed in the case of CMS-PCL presumably attributed to aggregation, where many water molecules were trapped and thus caused an increased mass.

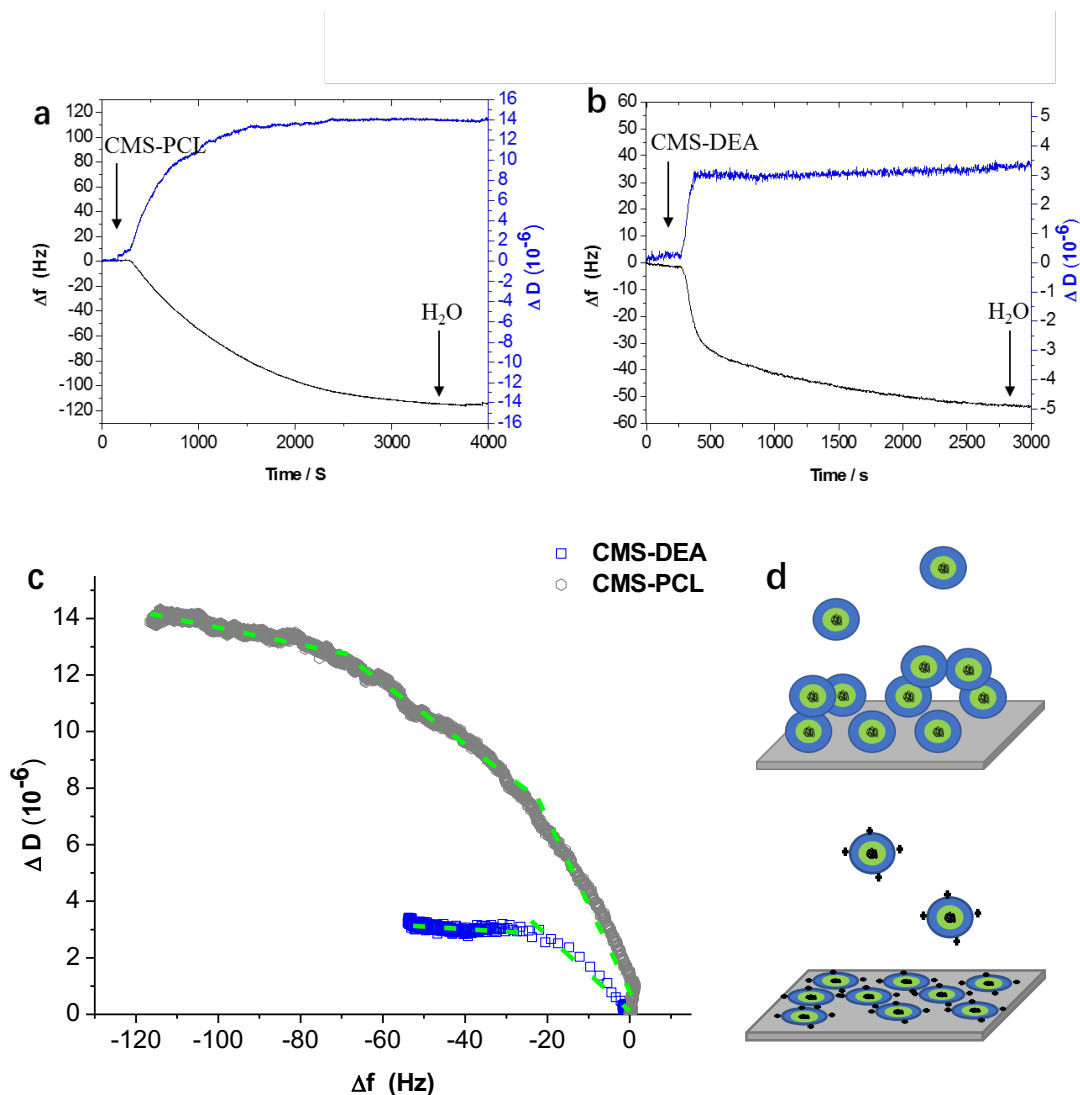


**Figure 4-5.** Changes in resonant frequency (black) and dissipation (blue) of model SC lipid coated quartz crystal as a function of time after introducing a) CMS-PCL and b) CMS-DEA carrier solutions at concentration 0.025 mg/mL. c) QCM data of CMS-PCL (black) and CMS-DEA (blue) are plotted as  $\Delta D$  vs  $\Delta f$ . The slopes of these two lines

(green dash) are fitted by Origin, represent the viscoelasticity of the substrates. (d) The possible configuration of CMS-PCL (top) and CMS-DEA (bottom) nanocarriers deposited on skin lipids.

#### 4.5. ATR-FTIR Study on Interactions between CMS and Isolated SC from Human Skin

We further used the ATR-FTIR technique to study the interactions between CMS carriers and SC by monitoring the conformation changes in both lipids and protein regions of isolated SC after CMS solution treatment. Pure water was used as control. A positive shift of  $2920\text{ cm}^{-1}$  and  $2850\text{ cm}^{-1}$  corresponding to asymmetric and symmetric stretching vibration of  $\text{CH}_2$ , respectively, in the lipids' tails indicated a fluidization of lipids.<sup>[111]</sup> As summarized in Figure 4-7, the most prominent shifts toward higher wavenumbers were observed for CMS-DEA-treated SC samples, indicating highest level of disordered lipids' structure. While the disturbing effect was less induced by CMS-PCL and no significant effect of  $\text{H}_2\text{O}$  on lipids' fluidization was noticed. Therefore, we could conclude that the payload penetration with both CMS carriers occurred intercellularly by disturbing lipids to a different extent.

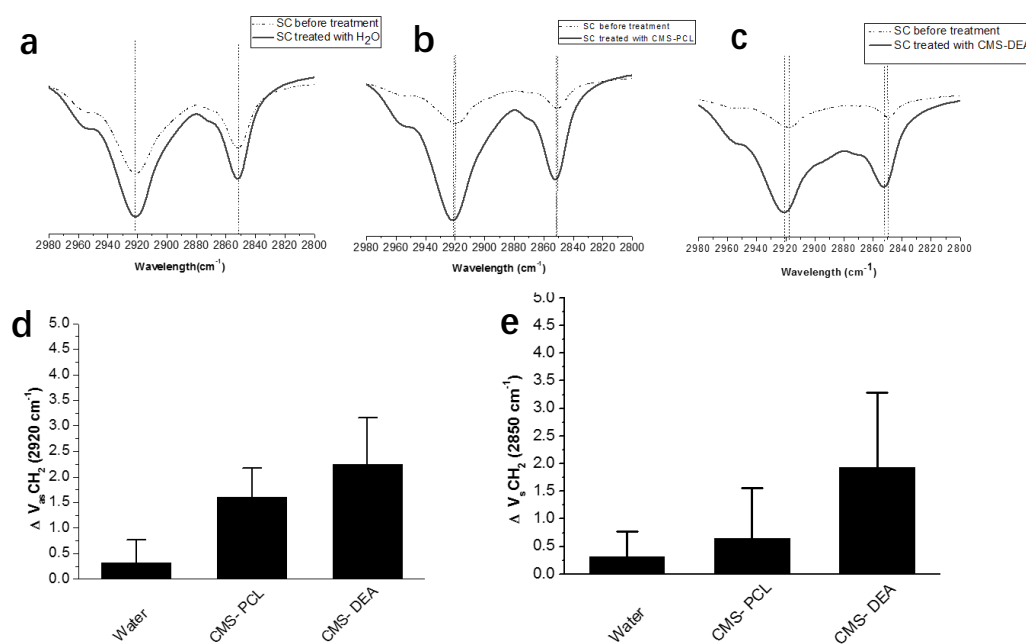


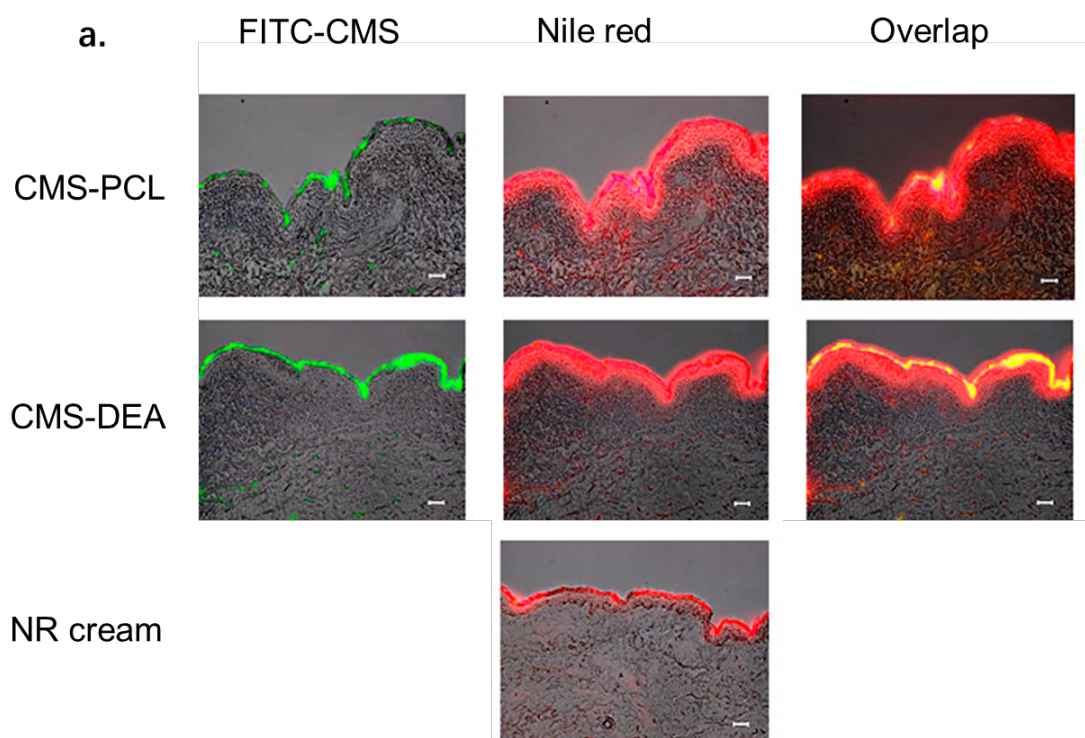
**Figure 4-6.** FTIR spectra of skin lipid region ( $3000\text{--}2800\text{ cm}^{-1}$ ) recorded before (dot) and after (solid) treating with a)  $\text{H}_2\text{O}$ , b). CMS-PCL, c) CMS-DEA; Quantification of peak shifting at d)  $\text{CH}_2$  asymmetric ( $2920\text{ cm}^{-1}$ ) and e) symmetric ( $2850\text{ cm}^{-1}$ ) stretching vibration

#### 4.6. Skin Penetration of CMS Containing Different Payloads

For clarifying the skin penetration enhancement effect, we started from Nile red as a tested payload. Two Nile red-loaded CMS nanocarriers labeled with FITC (CMS-FITC) were applied on intact human skin, and an oil-in-water base cream was used as a control. The fluorescence microscopy images of the cross-sections of skin after 6 h treatment are shown in Figure 4-8a. Both CMS could induce a large amount of Nile red to penetrate from SC to VE layers, because we could see strong red signals from Nile red detected in SC and VE layer in both cases. By the way of contrast, very weak Nile red signals only located on the topmost SC layer was observed with the base cream. FITC signals from the CMS themselves, on the other hand, were mainly captured in the SC layer, which demonstrated that both CMS could not pass through SC but could enhance the released Nile red to further penetrate into the deeper skin layers. Figure 4-8b shows the accumulated amount of Nile red in each skin section by quantifying the brightness of pixels. We found both CMS induced much a higher amount of Nile red to accumulate in different skin layers compared to base cream formulation. However, there was not any difference between these two CMS carriers regarding Nile red penetration, even though CMS-DEA interacted with skin much stronger as we discussed before. It is possible because of the lower Nile red loading capacity of CMS-DEA (0.1 wt%) than CMS-PCL (0.17 wt%), so the actual amount of Nile red transported by both CMS to skin at the same time were comparable. Additionally, because of the very low loading content in both cases, rapid diffusion of Nile red out of both carriers into skin lipids could easily happen, which made the difference more difficult to be observed.

A similar phenomenon was also observed by Hong et al.<sup>[95]</sup> They developed a dendron-based micelle with different end groups, which did not show any penetration

difference for the coumarin-6 dye, but it did induce a significant difference in the permeation of the drug Endoxifen. Even though we could not directly say which nanocarrier was better concerning the properties of drugs, nevertheless, based on our findings together with published results, we know efficient skin disruption, high drug loading capacity and efficient release can lead to optimal penetration enhancement of small lipophilic compounds. Thereby, case-by-case investigations are necessary to find the best candidate for the individual drug.



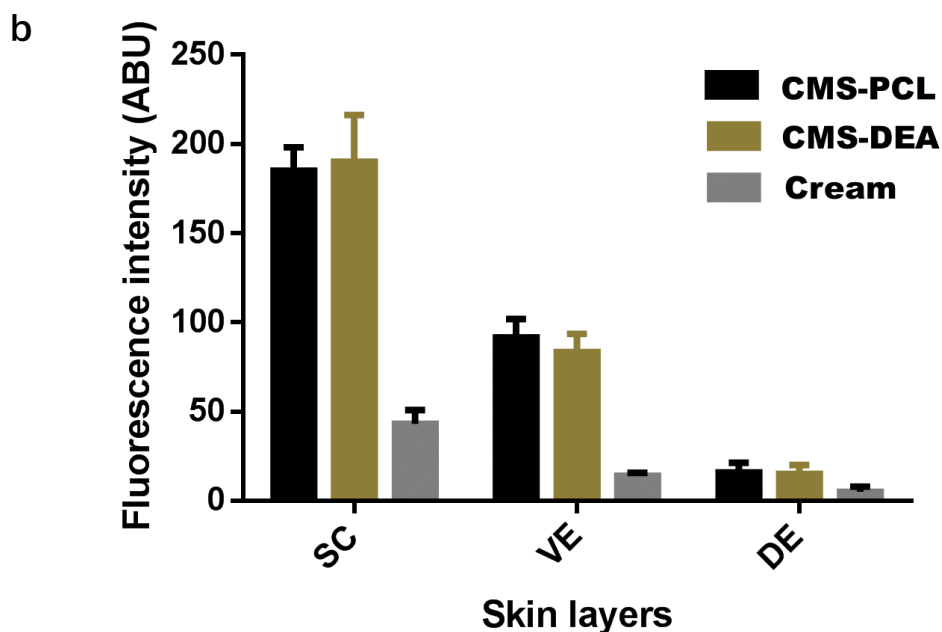


**Figure 4-7.** Visualization of skin penetration behaviors of Nile red loaded FITC-CMS, compared to commercial cream in human skin for 6 h treatment (green: FITC channel, red: Nile red channel). b) Quantified Nile red amount in different skin layers. (SC: stratum corneum; VE: viable epidermis; D: dermis, n = 3)

Normally charged carriers are more advantageous over neutral carriers on transmembrane delivery of biomacromolecules such as nucleic acids, peptides and proteins. In order to see whether this was applicable as well to topical delivery, we further tested CMS formulations containing bovine serum albumin labeled with FITC (BSA-FITC) on tape-stripped skin to mimic the destroyed skin environment and the same amount BSA-FITC-containing PBS solution was used as control. Figure 4-9 shows the cross-sections of stripped skin after 6 hours application. The green fluorescence signals are from BSA while the red signals are from rhodamine B-labeled CMS nanocarriers, and blue signals are from cell nuclei of the viable epidermis and dermis stained with DAPI. The strongest fluorescence intensity of BSA-FITC was observed through the whole stratum corneum when applied with CMS-DEA probably because of the strong affinity between CMS-DEA with skin. On the other hand, the BSA-FITC signals captured with CMS-PCL was even weaker than the control,

demonstrating forming complex with CMS-PCL can hinder the penetration of BSA probably due to the increased size compared to the free BSA. Both carriers stayed at SC without further penetrating viable skin layers even in damaged skin, demonstrating the small possibility of causing skin irritation. To conclude, above results proved that CMS-DEA could also be a potential candidate for topical biomacromolecules' delivery, for example, in wound healing or fungi infection.

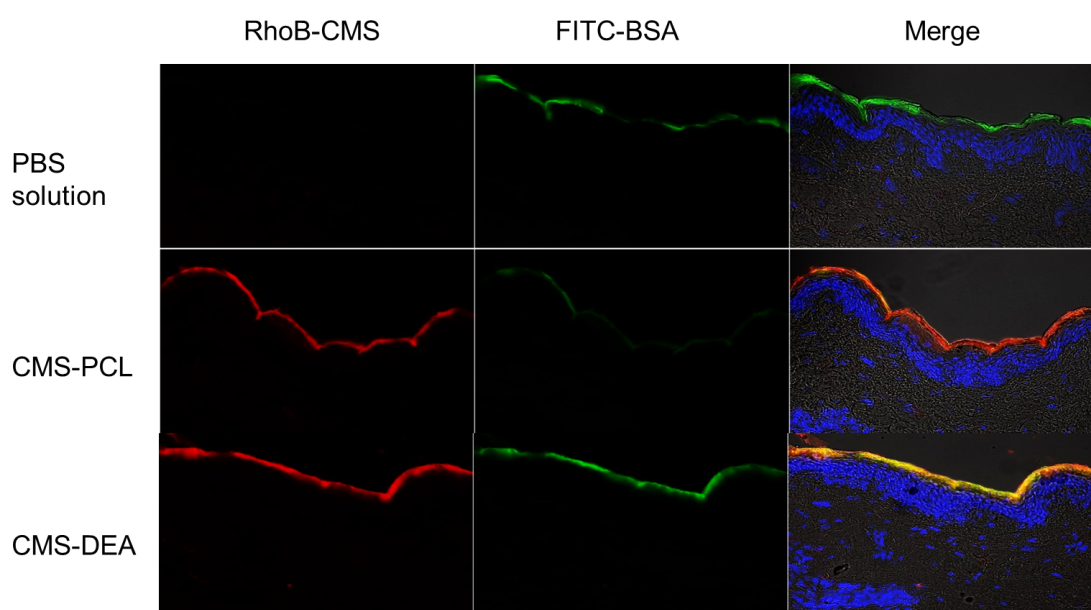


**Figure 4-8** Visualization of skin penetration behaviors of FITC-BSA loaded RhoB-CMS, compared to FITC-BSA in PBS solution on tape-stripped human skin for 6 h treatment (green: FITC channel, red: Rhodamine B channel).

#### 4.7 Cytotoxicity

The balance between effectiveness and toxicity is an important consideration in designing drug delivery systems to overcome biological barriers. MTT (Figure 4-10) results showed that the CMS-PCL nanocarriers have little toxicity even at high concentrations up to 500  $\mu\text{g/ml}$  after 24 h incubation against HaCaT cells. Introducing DEA moieties decreased the cell viability at higher concentrations. However, the biocompatibility has been largely improved compared to many other cationic carriers



such as PEI. The optimum balance could be achieved by further adjusting the functional degree of cationic moieties in the future studies.

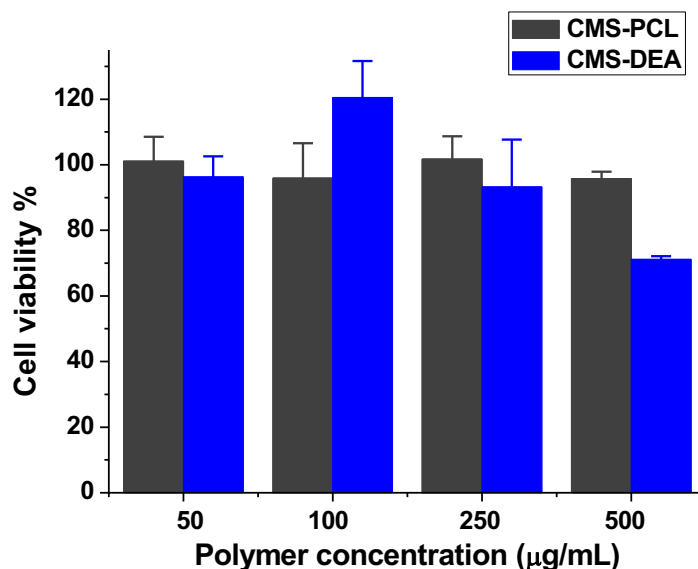


**Figure 4-9.** HaCat cell viability after treating with CMS nanocarriers at different concentrations for 24 h measured by MTT assay.

## Conclusion

In summary, the CMS nanocarrier with lipocationic charge moieties (CMS-DEA) was specifically designed for topical multi-payloads' delivery. It showed a stronger skin lipid interaction driven by both electrostatic and hydrophobic force compared to the CMS without charge moieties (CMS-PCL). Both carriers penetrated skin by disturbing the intercellular lipids in SC and could vastly enhance Nile red penetration compared to the cream formulation. CMS-DEA is more efficacious to transport biomacromolecules such as BSA into skin. Summing up, CMS-DEA showed penetration enhancement in both small lipophilic compounds and biomacromolecules, which demonstrates its potential as a universal platform for topical therapy.

## Chapter 5. Experimental Part

### Materials

hPG amine (Mn 10 kDa) with 70% amination and hPG amine (Mn 5 kDa) with 10% amination were provided by technician.  $\epsilon$ -Caprolactone (97%) was purchased from Sigma-Aldrich and was freshly distilled prior to use. Stannous 2-ethylhexanoate ( $\text{Sn}(\text{Oct})_2$ ), 5-methyl-5-allyloxycarbonyl-1,3-dioxan-2-one (MAC), succinic anhydride, 4-dimethylamino pyridine (DMAP), 2-(dimethylamino)ethanethiol hydrochloride (DEA), 2,2-dimethoxy-2-phenylacetophenone (DMPA), diisopropylethylamin (DIPEA), poly(ethylene glycol) methyl ether (mPEG,  $M_n \sim 2000 \text{ g mol}^{-1}$ ), *O*-(*N*-succinimidyl)-*N,N,N',N'* tetramethyluronium-hexafluorophosphate (HSTU), and Fluorescein isothiocyanate (FITC), Rodamine B (RhoB), ceramide (CER), cholesterol (CHO), and palmitic acid (PA), were purchased from Sigma-Aldrich and used as received.

### Characterizations

NMR spectra were recorded at 25 °C on a Bruker ECX 400 and ECP500 spectrometers. The molecular weight was measured by gel permeation chromatography (GPC) using DMF with 0.3% LiBr and 0.6% acetic acid or water as the mobile phase at a flow rate of 1 mL min<sup>-1</sup>. FTIR spectra were recorded on a JASCO FT/IR-4100 spectrometer with a resolution of 4 cm<sup>-1</sup> and averaged over 32 scans. Dynamic light scattering (DLS) was used to measure the size of the carrier. The measurements were carried out at 25 °C using a zetasizer Nano-ZS 15 equipped with a 633 nm He–Ne laser from Malvern Instruments. The morphologies of carriers were observed with cryogenic transmission electron microscopy (Cryo-TEM). Samples were prepared on copper grids (400 mesh) and visualized by a FEI CM12 electron microscope. The analysis of images was using the software Image J. QCM was carried out on Q-Sense E1, Sweden with a flow rate at 0.1 mL/ min, and the temperature was 25 °C. The samples were at the concentration of 0.025 mg/mL. Dexamethasone were quantified by high performance

liquid chromatography (HPLC) using a Knauer Smartline-HPLC system. The sample was passing through a rp-18 column (250 mm x 4 mm, 5  $\mu$ m particle size) and detected by a UV-Vis detector ( $\lambda$ = 245 nm). The mobile phase used was acetonitrile and water mixture (40:60, v/v) at the flow-rate of 1 mL min<sup>-1</sup>. The tacrolimus content was determined by LC-MS using the stable isotopically labeled internal standard [<sup>13</sup>C1,d4]Tacrolimus (Alsachim, Illkirch-Graffenstaden, France)]. Briefly, 45  $\mu$ L of sample solution was first mixed with 5  $\mu$ l [<sup>13</sup>C1,d4]Tacrolimus (1  $\mu$ M in methanol) as internal standard and then centrifuged at 9,500 x g for 3 min. Supernatants were subjected to LC-MS on an Agilent 1260 Infinity LC system equipped with an Agilent Poroshell 120 EC-C18 column (2.7  $\mu$ m, 3.0  $\times$  50 mm) together with an Agilent 6490 triple quadrupole-mass spectrometer (Agilent, Waldbronn, Germany). The mobile phase was 90% of Aqueous ammonium formate (20 mM, pH 3.5) and 10% of methanol at a flow rate of 0.4 mL/min.

## **5.1 Degradable CMS with Different Hydrophobicity for Efficient Topical Drug Delivery**

### **5.1.1. Synthesis of Hydroxy-terminated Double Shell mPEG-PCL<sub>m</sub>-OH**

Hydroxy-terminated double shell mPEG-PCL<sub>m</sub>-OH was synthesized by ROP of  $\epsilon$ -CL monomer using mPEG as an initiator in the presence of a catalytic amount of Sn(Oct)<sub>2</sub>. Briefly, mPEG (0.5 mmol) was dried at 70 °C under high vacuum for 16 hours. After being cooled to r.t., a calculated amount of distilled  $\epsilon$ -CL and Sn(Oct)<sub>2</sub> was injected into a flask under argon atmosphere. After exchanging three times the vacuum and argon, the polymerization proceeded at 120 °C for 1 day under argon protection, then quickly was cooled down to r.t. The polymer was then dissolved in 10 ml of DCM containing one drop of acetic acid and precipitated into a large volume of cold diethyl ether. The precipitates were collected by filtration and dried under hv for 24 hours (yield: > 90 %).

**mPEG-PCL<sub>5</sub>-OH**

<sup>1</sup>H NMR (400 MHz, Chloroform-d)  $\delta$  = 4.16 – 4.08 (m, 2H), 3.96 (t, 9H), 3.54 (s, 252H), 3.27 (s, 3H), 2.21 (m, 10H), 1.54 (m, 20H), 1.29 (m, 10H).

**mPEG-PCL<sub>10</sub>-OH**

<sup>1</sup>H NMR (400 MHz, Chloroform-d)  $\delta$  = 4.21 – 4.15 (t, 2H), 4.01 (m, 19H), 3.91 – 3.39 (m, 215H), 3.33 (s, 3H), 2.26 (m, 19H), 1.60 (m, 46H), 1.40 – 1.23 (m, 18H).

**mPEG-PCL<sub>20</sub>-OH**

<sup>1</sup>H NMR (400 MHz, Chloroform-d)  $\delta$  = 4.16 (m, 2H), 4.00 (t, 39H), 3.59 (m, 226H), 3.32 (s, 3H), 2.25 (m, 38H), 1.58 (m, 65H), 1.40 – 1.24 (m, 39H).

**5.1.2. Synthesis of Acid-terminated Double Shell mPEG-PCL<sub>m</sub>-COOH**

mPEG-PCL<sub>m</sub>-OH (0.3 mmol) and DMAP (0.6 mmol) were dissolved in 20 mL of anhydrous THF. Succinic anhydride (3 mmol) was subsequently added. The reaction system was stirred at r.t. for 2 days. Afterwards, the reaction mixture was placed in freezer overnight to precipitate the excess amount of succinic anhydride, which was subsequently removed by filtration. The filtrate was concentrated and precipitated into large volume of cold solvent mixture of methanol and diethyl ether (1:5, v/v) for three times (yield: > 70 %).

**mPEG-PCL<sub>5</sub>-COOH**

<sup>1</sup>H NMR (400 MHz, Chloroform-d)  $\delta$  = 4.20 – 4.11 (m, 2H), 3.98 (t, 9H), 3.57 (s, 204H), 3.30 (s, 3H), 2.54 (m, 3H), 2.25 (m, 9H), 1.56 (m, 19H), 1.39 – 1.22 (m, 9H).

**mPEG-PCL<sub>10</sub>-COOH**

<sup>1</sup>H NMR (500 MHz, Chloroform-d)  $\delta$  = 4.20 – 4.12 (m, 2H), 4.00 (t, 21H), 3.58 (s, 196H), 3.31 (s, 3H), 2.55 (m, 4H), 2.24 (m, 23H), 1.58 (m, 45H), 1.39 – 1.22 (m, 23H).

**mPEG-PCL<sub>20</sub>-COOH**

<sup>1</sup>H NMR (500 MHz, Chloroform-d)  $\delta$  = 4.25 – 4.15 (m, 3H), 4.04 (t, 41H), 3.62 (s, 224H), 3.36 (s, 3H), 2.66 – 2.55 (m, 4H), 2.37 – 2.21 (m, 43H), 1.62 (m, 86H), 1.43 – 1.28 (m, 40H).

### 5.1.3. Synthesis of Core-multishell Copolymers HPG-PCL<sub>m</sub>-mPEG

mPEG-PCL<sub>m</sub>-COOH (0.3 mmol) was dissolved in dry DMF (5 ml) containing DIPEA (1.2 mmol), followed by adding HSTU (0.4 mmol). The reaction was stirred at r.t. for 2 days under argon protection to activate the acid. 1 ml of DMSO solution containing amine-terminated hyperbranched polyglycerol (hPG-NH<sub>2</sub>, 0.2 mmol) was injected into the reaction mixture, which was kept stirring for another 2 days. The reaction mixture was then purified by dialysis against the mixture of MeOH and DCM (1:1, v/v) for 24 hours using the dialysis bag (MWCO 4 kDa). Thereafter, the solution in dialysis bag was dried. Precipitation fractionation was used to remove free double shells. Briefly, the crude CMS was redissolved in 10 ml of DCM at 45 °C. At the same time, hexane was added slowly until the solution turned cloudy. After several hours at r.t, two separate layers were observed, which could easily be separated. The bottom gel-like layer, which was the CMS phase, was collected. After repeating 3 times, CMS polymers with high purity could be achieved. (Yield: ~ 50 %).

#### hPG-PCL<sub>5</sub>-mPEG

<sup>1</sup>H NMR (500 MHz, Chloroform-d) δ = 4.32 – 4.13 (m, 9H), 4.03 (t, 10H), 3.62 (s, 235H), 3.36 (s, 3H), 2.65 – 2.55 (m, 1H), 2.28 (t, 10H), 1.62 (m, 25H), 1.36 (t, 13H).

#### hPG-PCL<sub>10</sub>-mPEG

<sup>1</sup>H NMR (500 MHz, Chloroform-d) δ = 4.17 (t, 2H), 4.00 (t, 19H), 3.59 (s, 194H), 3.32 (s, 3H), 2.57 (s, 3H), 2.25 (t, 19H), 1.69 – 1.48 (m, 40H), 1.32 (m, 19H).

#### hPG-PCL<sub>20</sub>-mPEG

<sup>1</sup>H NMR (500 MHz, Chloroform-d) δ = 4.17 (m, 3H), 4.01 (m, 36H), 3.33 (s, 3H), 2.58 (s, 2H), 2.26 (m, 35H), 1.60 (m, 74H), 1.40 – 1.26 (m, 41H).

### 5.1.4 Synthesis of Fluorescein Isothiocyanate (FITC) labelled CMS Nanocarriers

50 mg of CMS was dissolved in 5 mL of anhydrous DMF. 5 mg of FITC in 300 μL of DMF was slowly added to CMS solution during stirring. The reaction was running overnight at r.t. Afterwards, the unreacted FITC was removed by gel filtration using

Sephadex-G25, followed by dialysis against MeOH to afford FITC labelled CMS nanocarrier. The successful conjugation was proved by TLC.

#### **5.1.5. Preparation of Aqueous Dispersions of CMS Nanocarriers**

5 mg of CMS were weighted in glass vial, to which 1 ml of MilliQ water was added. CMS 1 could dissolve in water directly after several minutes' incubation, while the other two were heated in a water bath at 55 °C for 2 minutes to get clear solutions. To avoid big aggregations, the solutions were further ultrasonicated for 10 min.

#### **5.1.6. Drug Encapsulation**

Dexamethasone was encapsulated via the film-uptake method. Briefly, 100 µL of the dexamethasone stock solution (5 mg/ML in actone) were transferred into each small glass vial of sample. After the solvent completely evaporated under vacuum, 1 mL of the CMS solution (5mg/mL) or MilliQ water was added as a control, followed by stirring at 800 rpm for 24 h. In the end, the excess dexamethasone was filtered by 0.45 µm RC filters to produce Dexa@CMS. The dexamethasone-loaded CMS were kept at 4 °C prior to use.

#### **5.1.7. Release Studies**

Release of dexamethasone from CMS 1-3 was performed in phosphate-buffered saline (PBS, pH 7.4) for 24 h at 37 °C while shaking (New Brunswick Scientific Co. Int.) 0.6 ml of Dexa @CMS 1-3 was transferred into a dialysis bag (MWCO 3.5 kDa), which was sunk into 15 mL of PBS. At each time point, 5 mL of dialysis media was withdrawn and the same volume of fresh PBS was added. The released dexamethasone amount was determined by HPLC. Experiments were performed in triplicate.

#### **5.1.8. Cell Viability Assays**

The cell compatibility of CMS nanocarriers was determined by evaluation of the viability or cellular index of HaCaT cell line via both MTT and real-time cell analysis (RTCA) assay. In MTT assay, the cells were seeded into 96-well plates at an initial density of 10,000 cells/well and incubated for 24 h. Afterwards, the culture medium

was replaced with 100  $\mu\text{L}$  of fresh medium containing various concentrations of CMS nanocarriers (0, 50, 100, 250, and 500  $\mu\text{g}/\text{mL}$ ). The cells were incubated for 24 h in the presence of materials. After that, 20  $\mu\text{L}$  of MTT solution was added per well to treat the cell for 2 hours and then the old culture medium was abandoned and replaced with 100  $\mu\text{L}$  of DMSO per well to dissolve the blueish formazan crystals. The optical density was measured at 490 nm by a microplate reader. For RTCA, E-plate 96 (Roche, Mannheim, Germany) containing 50  $\mu\text{L}$  of culture medium in each well was first measured as a background. Afterwards, HaCaT cells were seeded at a density of 10,000 cells/well and incubated for 24 h, followed by adding CMS nanocarrier solutions at various concentrations from 0-500  $\mu\text{g}/\text{mL}$ . The cell proliferation and viability was recorded at time intervals of 15 min within a 48h treatment by the cell electronic sensor (CES) system.

#### **5.1.9. Cellular Uptake**

HaCaT and J774A.1 cells (mouse macrophages) were seeded with density in  $2.5 \times 10^4$  cells/well on a 24-well plate and cultured for 24 h, followed by treatment with FITC-CMS 2 for an additional 4 h and 24 h, respectively. The cell nuclei and membrane were stained with DAPI and Alexa Fluor 594 for 30 min, followed by thorough rinsing with PBS to remove the free dyes. CLSM was used for observing the cellular uptake and Leica Application SuiteX software was used for data analysis.

#### **5.1.10. Skin Penetration**

The fluorescent dye Nile red was selected as the probe to visualize the topical delivery behavior of both CMS nanocarriers. All the formulations was prepared by physically encapsulating Nile red into CMS 1-3 and FITC-CMS 2 via the above-described film-uptake method. A conventional base cream with the identical Nile red concentration (0.0004%) was prepared as a reference. Intact human skin was thawed and punched into pieces with 2 cm diameter, subsequently placed onto Franz cells with the SC layer towards the air and the dermis in contact with the PBS-filled receptor, and stirred at 500 rpm, 33.5 °C. After ca. 30 min to achieve equilibrium, 35.4  $\mu\text{L}$  of each formulation was

then applied onto the skin surface. After 6 h incubation, the skin surface was gently rinsed with PBS, followed by embedding into a tissue freezing medium and stored at -80 °C.

For data evaluation, the skin discs were cut into vertical slices of 8 µm thickness using a freeze microtome. The slices were observed using the fluorescence microscope with both normal light and fluorescence light (red channel: 1/10 s) channel. The relative dye content in each layer of skin per sample was determined by reading the value of arbitrary pixel brightness units (ABU) with BZ image analysis software. Experiments were repeated with three independent donors.



## **5.2 Skin Penetration of Tacrolimus-containing CMS Formulations**

### **5.2.1 Tacrolimus Loading Study**

#### **5.2.1.1 Tacrolimus Loading with Three Different Methods**

750 µg of tacrolimus was taken from the stock solution and put into a small glass vial and dried completely under high vacuum. 1 mL of CMS 2 solution (5 mg/mL) was added, followed by strong stirring at 500 rpm for 16 hours. Then the excess drug was removed by filtration (RC filter, 0.45 µm) and the supernatant was collected and kept at 4 °C.

Another method was to take 750 µg of tacrolimus from stock solution into small glass vial and dry it completely under high vacuum. 1 mL of CMS 2 solution (5 mg/mL) was added, followed by sonification for 1 hour. After that, the solution was passed through the RC filter with pore size 0.45 µm and the supernatant was collected and kept at 4 °C.

The third method was to dissolve 750 µg of tacrolimus and 5 mg CMS together in 200 µL of DCM. The mixed solution was subsequently injected into 1 mL of MilliQ water under ultrasonification (100 W, model W-220f, from Heat Systems-Ultrasonics, Inc.) for 3 mins to form an emulsion. DCM was then removed by rotary evaporator until the solution was completely clear. The final solution was then adjusted with water to 1 mL and kept at 4 °C overnight. The unloaded drug was then removed by filtration (RC filter, 0.45 µm) and the supernatant was collected and kept at 4 °C.

#### **5.2.1.2 Preparations of Formulations with Different Tacrolimus Content**

CMS with different Tacrolimus-loading contents was prepared via the emulsion method. Briefly, a calculated amount of tacrolimus was mixed with 5 mg CMS in 200 µL of DCM. The mixed solution was subsequently injected into 1 mL of MilliQ water under ultrasonification (100 W, model W-220f, from Heat Systems-Ultrasonics, Inc.) for 3 mins to form an emulsion. DCM was then removed by rotary evaporator until the solution was completely clear. The final solution was then adjusted with water to 1 mL

and kept at 4 °C overnight. The unloaded drug was then removed by filtration (RC filter, 0.45 µm) and the supernatant was collected and kept at 4 °C. The loading content was measured by LC-Mass.

### **5.2.2 Release Studies**

We used a dialysis method to study the drug release. Briefly, 0.3 mL of the tacrolimus-loaded CMS solution was placed in a dialysis bag with a molecular weight cut-off (MWCO) of 8 - 10 kDa. The dialysis bag was then immersed in 10 ml of PBS. Drug release studies were carried out in a shaker (New Brunswick Scientific Co. Int.) with 100 rpm at 32 °C. The whole accepted solution was periodically replaced with the same volume of fresh PBS. All the samples were freeze-dried and redissolved in 1 mL of ethanol. After centrifugation for 10 mins at 10,000 rpm to remove the salts, the supernatant was collected and quantified by LC-MS.

### **5.2.3 *In Vitro* skin Penetration of Tacrolimus**

Penetration of Tacrolimus was performed on fresh Human skin with surface area of 2.5 cm<sup>2</sup> in franz cell set-up. 36 µL of CMS formulation and Protopic ointment (containing 0.03% tacrolimus) were applied on the skin surface for 24 or 48 h. After each treatment, the skin was cleaned and excess amount of formulation was removed. Thickness of each skin layer was determined by H&E staining. Each skin layer was separated by horizontally cutting depending on the predetermined thickness. The separated layers were homogenised and the containing tacrolimus was extracted with 400 µL EtOH. After centrifuge for 5 min, the supernatant was subjected to LC-MS.

### 5.3 Cationic CMS as Potential Platform for Topical Multi-payloads Delivery.

#### 5.3.1 Synthesis of Hydroxy-terminated Double Shell mPEG-P(MAC-co-CL)-OH

Hydroxy-terminated double shell were synthesized by ROP of  $\epsilon$ -CL and MAC comonomers using mPEG as initiator in the presence of a Sn(Oct)<sub>2</sub> catalyst. Briefly, mPEG (0.5 mmol) was dried at 70 °C for 24 hours under vacuum. After cooling to r.t., a calculated amount of  $\epsilon$ -CL, MAC monomers, and Sn(Oct)<sub>2</sub> was added. After exchanging the vacuum argon three times, the reaction was stirred for 16 hours at 110 °C, followed by quickly cooling to r.t. 10 mL of DCM together with one drop of acetic acid were added to dissolve the polymer, followed by precipitation in a large volume of ice-cold diethyl ether and dried under vacuum for 1 day. (Yield > 80%).

##### mPEG-PCL<sub>15</sub>-OH

<sup>1</sup>H NMR (400 MHz, Chloroform-d)  $\delta$  = 4.16 (m, 2H), 4.00 (t, 33H), 3.32 (s, 3H), 2.25 (t, 31H), 1.58 (m, 65H), 1.41 – 1.22 (m, 31H).

##### mPEG-P(MAC<sub>5</sub>-co-CL<sub>10</sub>)-OH

<sup>1</sup>H NMR (400 MHz, Chloroform-d)  $\delta$  = 5.87 (m, 6H), 5.38 – 5.17 (m, 13H), 4.61 (d, 13H), 4.39 – 4.16 (m, 17H), 4.15 – 3.99 (m, 28H), 3.87 – 3.42 (m, 230H), 3.37 (s, 3H), 2.30 (m, 27H), 1.63 (m, 52H), 1.37 (m, 31H), 1.29 – 1.18 (m, 16H).

#### 5.3.2 Synthesis of Acid-terminated Double Shell mPEG-P(MAC-co-CL)-COOH

mPEG-P(MAC-co-CL)-OH (0.5 mmol), DMAP (1 mmol), and succinic anhydride (2.5 mmol) were dissolved together in 100 mL of anhydrous THF. The reaction was stirred at r.t. for 2 days. Thereafter, the reaction mixture was transferred into a dialysis bag (MWCO 2kD) and dialysis against the mixed solvent of MeOH and DCM (1:1 v/v). The pure product was dried under vacuum for 1 day. (Yield > 70 %).

##### mPEG-PCL<sub>15</sub>-COOH

<sup>1</sup>H NMR (400 MHz, Chloroform-d)  $\delta$  = 4.27 – 4.19 (m, 2H), 4.05 (t, 38H), 3.85 – 3.42 (m, 264H), 3.37 (s, 3H), 2.62 (d, 5H), 2.30 (m, 39H), 1.64 (m, 80H), 1.48 – 1.29 (m, 33H).

### **mPEG-P(MAC<sub>5</sub>-co-CL<sub>10</sub>)-COOH**

<sup>1</sup>H NMR (400 MHz, Chloroform-d)  $\delta$  = 5.86 (m, 7H), 5.34 – 5.14 (m, 16H), 4.59 (d, 15H), 4.34 – 4.15 (m, 23H), 4.14 – 3.97 (m, 31H), 3.61 (s, 231H), 3.35 (s, 3H), 2.57 (d, 2H), 2.28 (t, 31H), 1.67 – 1.49 (m, 54H), 1.42 – 1.29 (m, 29H), 1.26 – 1.15 (m, 24H).

### **5.3.3 Synthesis of Dendritic Core-multishell Copolymers hPG-P(MAC<sub>m</sub>-co-CL<sub>n</sub>)-mPEG and hPG-PCL<sub>n</sub>-mPEG.**

mPEG-P(MAC<sub>m</sub>-co-CL<sub>n</sub>)-COOH (0.3 mmol) was dissolved in 5 ml of dry DMF, which contained DIPEA (1.2 mmol). HSTU (0.4 mmol) was then added. After stirring at r.t. for 2 days, 1 mL DMSO-containing aminated hyperbranched polyglycerol (hPG-NH<sub>2</sub>, 0.6 mmol) was added to the reaction mixture and stirred for another 2 days. The reaction mixture was purified by dialysis against the mixture of MeOH and DCM (1:1, v/v) for 24 hours using the dialysis bag (MWCO 4 kDa). Thereafter, the product was collected and dried. To remove free double shells, precipitation fractionation was used. Briefly, the crude CMS product was redissolved in 10 ml of DCM at 45 °C. At the same time, hexane was slowly added until the solution turned cloudy. After kept several hours at r.t, two separated layers were observed, which could easily be separated. The bottom gel-like layer, which is the CMS phase, was collected. After repeating 3 times, CMS polymers could be achieved with high purity. Synthesis of CMS-PCL was carried out in the same way. (Yield: ~ 50 %)

### **hPG-PCL<sub>15</sub>-mPEG (CMS-PCL)**

<sup>1</sup>H NMR (500 MHz, Chloroform-d)  $\delta$  = 4.20 (t, 2H), 4.03 (t, 34H), 3.62 (s, 228H), 3.35 (s, 3H), 2.60 (s, 2H), 2.47 (s, 1H), 2.28 (t, 32H), 1.62 (m, 65H), 1.36 (m, 32H).

### **hPG-P(MAC<sub>5</sub>-co-CL<sub>10</sub>)-mPEG (CMS-DEA)**

<sup>1</sup>H NMR (400 MHz, Chloroform-d)  $\delta$  = 5.87 (m, 7H), 5.40 – 5.16 (m, 18H), 4.61 (d, 17H), 4.47 – 4.16 (m, 20H), 4.17 – 3.96 (m, 27H), 3.63 (s, 233H), 3.37 (s, 3H), 2.62 (s, 2H), 2.30 (m, 31H), 1.75 – 1.48 (m, 76H), 1.37 (m, 37H), 1.26 (d, 19H).

### **5.3.4 Synthesis of Dendritic Core-multishell Copolymers hPG-P(DEA<sub>m</sub>-co-CL<sub>n</sub>)-mPEG**

Briefly, the allyl-functionalized CMS (0.2 mmol of allyl group), DEA (2.0 mmol), and a catalytic amount of DMPA were dissolved in 30 mL of the mixed solvent of THF and water (1:1 v/v), followed by argon bubbling for 5 min to remove dissolved oxygen. The mixture was stirred at room temperature for 4 hours under UV radiation (254 nm, 1.29mW/cm<sup>2</sup>). The mixture was placed in a dialysis bag (MWCO 2 kDa) and dialyzed against water/methanol (1:1 v/v) mixture for 2 days and pure water for 1 day. Samples in the dialysis bag was collected and freeze-dried to give the final product.

#### **hPG-P(DEA<sub>5</sub>-co-CL<sub>10</sub>)-mPEG**

<sup>1</sup>H NMR (400 MHz, Chloroform-d)  $\delta$  = 4.24 (d, 69H), 4.07 (m, 35H), 3.63 (s, 224H), 3.37 (s, 3H), 3.18 (s, 67H), 3.05 (s, 2H), 2.64 (s, 16H), 2.30 (q, 32H), 1.96 (s, 15H), 1.64 (m, 77H), 1.39 (m, 76H), 1.25 (t, 22H).

### **5.3.5 Synthesis of Dye Labelled Dendritic Core-multishell Copolymers.**

FITC labelled CMS were prepared via the same procedure as described in section 5.1.4. Rhodamine B labelled CMS (RhoB-CMS) were prepared by ester coupling reaction. Briefly, Rhodamine B (2.6 mg, 6  $\mu$ mol), DCC (0.7 mg, 3  $\mu$ mol) was dissolved in 5 mL of anhydrous DMF. CMS (50 mg, 1  $\mu$ mol) together with catalytic amount of DMAP was added to the reaction mixture. The reaction was stirring overnight at r. t. The unreacted Rhodamine B was removed by gel filtration b using Sephadex-G25, followed by dialysis against MeOH to afford Rhodamine B labelled CMS nanocarriers. The successful conjugation was proved by TLC.

### **5.3.6 Drug Encapsulation**

Tacrolimus, an anti-inflammatory drug with molecular weight 804 Da, was encapsulated by the miniemulsion method. Briefly, 150  $\mu$ L of Tacrolimus stock solution in DCM at 5 mg/mL concentration was well mixed with 100  $\mu$ L of CMS in DCM at the concentration of 50 mg/mL. The mixture solution was then slowly injected into 1 mL

of Milli-Q water to form an emulsion during high powered ultrasonification (100 W, model W-220f, from Heat Systems-Ultrasonics, Inc., 3 min), and cooled by an ice bath. Afterwards, the DCM was completely removed by rotary evaporator at 30 °C for about 30 mins. The final solution was then adjusted with water to 1 mL and kept at 4 °C overnight. The non-encapsulated drug was removed by passing through 0.45 µm RC filters. The loading content was measured by LC-MS.

### **5.3.7 FITC-BSA Binding.**

CMS was first dissolved in PBS at 1 mg/mL. 100 µL of FITC-BSA (10 mg/mL in PBS) was added to 1 mL CMS solution, followed by vortex for 30 seconds. The unbounded BSA was removed by ultrafiltration using Amicon ultrafiltration membrane (100 kDa). The filtrate was collected and the unbounded protein was quantified by fluorescence spectroscopy. The binding protein amount was calculated by using the total amount of protein minus the unbounded protein amount.

### **5.3.8 Release Studies of Tacrolimus from CMS Nanocarriers.**

The drug release studies were performed at 32 °C in phosphate buffer at both pH 5 and 7.4. 0.3 mL of tacrolimus-loaded CMS solution was placed in each dialysis bag (MWCO 8-10 *kDa*). The dialysis bags were immersed into 10 mL of the above-mentioned phosphate buffer solution. The release setup was kept in an incubator shaker (New Brunswick Scientific Co. Int.) at 32 °C, with shaking speed 100 rpm. The whole accepted solution was periodically removed and the fresh media with the same volume was replenished. The amount of released Tacrolimus was determined by LC-MS.

### **5.3.9 CMS-SC Interaction Measurements Using QCM**

Quartz crystal microbalance with dissipation (QCM-D, Q-Sense E1, Sweden) was used to test the interaction between CMS carriers and the SC model on the surfaces. By the monitoring the changes in resonance frequency ( $\Delta F$ ) of a piezoelectric quartz crystal as a function of time, the adsorption mass and diffusion rate could be calculated. The surface rigidity could be estimated from the ratio of D/F.

SC models on a quartz crystal sensor were prepared via spray coating using an airbrush (Evolution solo, Harder & Steenbeck, Germany). First a lipid solution was prepared by dissolving an equimolar of PA, CHO, and CER, and in a mixed solvent of hexane and ethanol (2:1 v/v) at a concentration of 4.5 mg/mL. The prepared lipids solution was subsequently applied on the quartz crystals' surface using an airbrush to yield a thin layer of model SC membrane. The model SC on substrates was dried under vacuum for one day before use.

The lipid-coated, quartz-crystal sensors were inserted into the flow chamber (QFM 401, QSense, Sweden, internal volume of 40  $\mu$ L), to which MilliQ water was subsequently pumped in at a flow rate 0.1 mL/min until baseline equilibration was achieved. Then CMS carriers at concentration 0.025 mg/mL were pumped into the chamber at the same flow rate until another equilibrium was achieved, which took about 50 min and was followed by rinsing with water again. The flow rate during all the experiments was kept constantly at 0.1 mL/min, and the temperature was 25 °C. F and D were recorded at different overtones from 3 - 13. Only the plot at third overtone appeared.

### **5.3.10 Fourier-Transform-Infrared (FTIR) Spectroscopy Measurements**

The SC from intact human skin was separated according to a previously reported procedure. Isolated SC was washed by PBS for 3 times and dried at room temperature for 3 days. After they were completely dry, the SC layers were cut into pieces with 0.5 cm diameter and placed into a 24-well culture plate. FTIR spectrum was recorded for each pre-treatment piece as blank. Then the SC layers were incubated with 200  $\mu$ L of CMS aqueous solution (5mg/mL) for 24 h and pure water was used as negative control. Afterwards, the SC was rinsed with PBS and dried at room temperature for 3 days. The FTIR spectrum was recorded again for each sample and compared with its own pretreated spectrum. The experiment was performed in triplicate with three different donors.

### **5.3.11 Cell Viability Assays**

The cytotoxicity of CMS nanocarriers was assessed by evaluation of the viability of HaCaT cell line and adult skin keratinocytes by MTT test. Briefly, cells were seeded on 96-well plates at an initial density of 10,000 cells/well and incubated for 24 h. Afterwards, the culture medium each well was replaced with 100  $\mu$ L of fresh medium containing various concentrations of CMS nanocarriers (0, 50, 100, 250, and 500  $\mu$ g/mL). Cells were then incubated for another 24 h in the presence of the materials. After that, 20  $\mu$ L of MTT solution was added per well to treat the cell for 4 hours and then the old culture medium was abandoned and replaced with 100  $\mu$ L of DMSO per well to dissolve the produced blueish formazan crystals by cells. The optical density was measured at 570 nm by a microplate reader.

### **5.3.12 Skin Penetration**

The fluorescent dye Nile red was selected as the first payload to visualize the topical delivery behavior of both CMS nanocarriers. The formulation containing 0.0004% Nile red was prepared by the film-uptake method (section 5.1.6). A conventional base cream with the identical Nile red concentration was prepared as a reference. Intact human skin was thawed and punched into pieces with 2 cm diameters, subsequently placed onto Franz cells with the SC layer towards the air allowing the dermis to be contact with the PBS-filled in receptor, and stirred at 500 rpm. After ca. 30 min to achieve equilibrium, 35.4  $\mu$ L of each formulation was then applied onto the skin surface. After 6 h incubation, the skin surface was gently rinsed with PBS, followed by embedding into a tissue-freezing medium and stored at -80  $^{\circ}$ C.

For visualizing penetration of BSA-FITC, a similar protocol was used with a minor modification. Briefly, the same amount of BSA-FITC was mixed with both CMS at 2.5 mg/mL and applied directly on taped stripped human skin (30 times stripped) for 6 h incubation in Franz cell. A BSA-FITC-containing PBS solution served as the control. After incubation, the skin surface was rinsed, which was followed by embedding into a tissue-freezing medium and stored at -80  $^{\circ}$ C.



For data evaluation, the skin discs were cut into vertical slices of 8  $\mu\text{m}$  thickness using a freeze microtome. The slices were observed using the fluorescence microscope with both normal and fluorescence light (red channel: 1/10 s) channel. The relative dye content in each layer of skin per sample was determined by reading the value of arbitrary pixel brightness units (ABU) with BZ image analysis software. Experiments were repeated with three independent donors.

## Summary and Outlook

### Summary

This dissertation aimed at designing biodegradable CMS nanocarriers which could efficiently deliver bioactive molecules into skin. Fundamental studies of the interactions between CMS nanocarriers and therapeutics, or CMS with skin layers were carried out. Specifically, drug loading, release and skin penetration behaviors of CMS with hydrophobicity were first investigated. Derived from this basic CMS structure, cationic CMS which could delivery both hydrophobic drugs and biomacromolecules were further developed. This dissertation contains three parts.

In the first part, in order to find the optimal CMS carrier for topical application, a series of degradable CMS (CMS 1-3) with different hydrophobicity were synthesized. The influence of hydrophobicity on single-/multi-molecular aggregation behaviors were studied. CMS 1 and 2 were mainly unimolecular micelles in aqueous solution. By further increasing hydrophobicity, CMS 3 started forming some small clusters. Whereas, the corresponding linear shells assembled into small micelles by intermolecular interactions. The multi-molecular micelles were broken down immediately in THF (less polar environment than water), while unimolecular systems showed good stability. The model drug Dexamethasone was encapsulated by CMS and shells via film uptake method. With increased hydrophobicity, drug loading capacity was increased. CMS showed significantly increased drug loading capacity compared to the corresponding shell counterparts. All the three CMS encapsulate dexamethasone in an unimolecular way, confirmed by DLS, while large aggregates formed by the shells upon drug loading. The release profiles of CMS 1-3 were also compared. CMS 1 displayed only burst release, while the other two showed biphasic release profiles. The release of dexamethasone from CMS was decelerated by increased hydrophobicity. The *in vitro* skin penetration experiment showed all the three CMS could successfully deliver Nile red to deep skin layers and could significantly enhance the deposition of Nile red in each skin layer, compared to conventional cream formulation. Among the three

candidates, CMS 2 showed the best performance. The penetration pathway of CMS nanocarriers were most likely occurred in intercellular lipids, because of the amphiphile nature of CMS and also the low affinity between CMS nanocarriers and corneocytes (terminally differentiated keratinocytes), proved by cellular uptake study towards keratinocytes. The cytotoxicity test showed CMS were non-toxic towards HaCat cells and the BCOP test showed CMS didn't cause any irritation to bovine eyes. In addition, CMS nanocarriers were proved SC impermeable. Therefore, we could conclude that CMS can be used as safe and efficient carriers for topical drug delivery.

In the second part, we focused on *in vitro* skin penetration of tacrolimus loaded CMS formulation. Tacrolimus were efficiently loaded into CMS nanocarriers by miniemulsion method. Stabled CMS formulation containing comparable Tacrolimus amount as the commercial product Protopic ointment were successfully prepared. Tacrolimus was released from CMS nanocarriers in a sustainable manner without initial burst release (ca. 30% drug released within 7 days). *In vitro* skin penetration showed that CMS could significantly increase the deposition amount of tacrolimus in each skin layer and the enhancement effect was more significant with increased treatment time.

In the third part, cationic CMS bearing lipophilic tertiary amino groups (CMS-DEA) was designed for topical multi-payloads delivery. For comparison, CMS without charge groups (CMS-PCL) was also synthesized. Due to the protonation and deprotonation process of the tertiary amine, size and zeta-potential of CMS-DEA was significantly influenced by pH value, while negligible changes were observed in the case of CMS-PCL. To demonstrate the universality of CMS nanocarriers, both hydrophobic drug tacrolimus and hydrophilic biomacromolecule BSA were selected as models to test the loading capacity. CMS-DEA displayed more superiority in both payloads loading. Tacrolimus release from CMS-DEA was responsible to the change of pH value. Accelerated drug release was observed at acidic pH than at neutral pH, which enables it a smart carrier for on-demand drug release. On the other hand, the release from CMS-PCL is independent on pH. Interactions between CMS carriers and SC lipids were assessed via QCM. A faster and stronger interactions between skin and CMS-DEA

were observed due to electrostatic force. At the same time, CMS-DEA also displayed stronger fluidization effect on intercellular lipids than CMS-PCL, determined by ATR-FTIR. In the end, to prove the concept, both Nile red and FITC-BSA were selected as probes to test skin penetration. CMS-DEA facilitated comparable skin deposition of Nile red as CMS-PCL, both of which were much better than the conventional cream. However, CMS-DEA displayed much higher efficiency than CMS-PCL or blank control without carrier on FITC-BSA delivery. Both CMS carriers were proved mainly staying at the SC layer without further penetration even in damaged SC, demonstrating less probability to cause skin irritation. Introducing of the DEA groups slightly increased the cytotoxicity, which can be expected from cationic material. However, compared to the other reported cationic carriers such as PEI, the biocompatibility of CMS-DEA was much improved and can be further improved by tuning the functional degree of DEA groups or using other tertiary amines with isoelectric point (pI) value lower than 7.4.

## **Outlook**

This dissertation demonstrated that CMS nanocarriers were very promising candidates for topical drug delivery. But they are still far away from practical applications. For example, a formulation should be further developed which can easily fix CMS solution on skin. *In vivo* therapeutic effects should also be tested. So far, the degradation of the systems described in this dissertation by skin enzymes only limited to the ester-linker between core and double shell. The degradation of polyesters takes a long time from weeks to years depending on the composition, which could not be used as a trigger for drug release in this case. Since release rate significantly influence the penetration rate of therapeutics, degradation-triggered-release systems should be developed in future studies.

## **Zusammenfassung**

Ziel der Arbeit war die Entwicklung bioabbaubarer CMS Nanocarrier, welche den Transport von biologisch aktiven Molekülen in die Haut ermöglichen sollten. Es wurden grundlegende Studien zu Wechselwirkungen zwischen CMS Nanocarriern und Therapeutika, sowie zwischen CMS Nanocarriern und Hautschichten durchgeführt.

Im ersten Teil der Arbeit wurde eine Serie von abbaubaren CMS Nanocarriern entwickelt (CMS 1 - 3), welche sich in der Hydrophobizität ihrer Hülle unterschieden. Eine Untersuchung des Aggregationsverhaltens ergab, dass die CMS mit steigender Hydrophobizität ihrer Schale eine vermehrte Tendenz zur Bildung von CMS-Clustern aufweisen. Im Anschluss wurde das Transportverhalten der CMS 1- 3 untersucht. Mit Hilfe der Filmmethode konnte Dexamethason in den CMS 1 - 3 in wässriger Lösung verkapselt werden. Unter Verwendung von Dynamischer Lichtstreuung (DLS) wurde nachgewiesen, dass die Aufnahme von Dexamethason auf das unimolekulare Transportverhalten der CMS 1 - 3 zurückzuführen ist. Zudem konnte gezeigt werden, dass die Beladung der CMS mit Dexamethason mit steigender Hydrophobizität der Schale zunimmt, wo hingegen die Geschwindigkeit der Freisetzung steigender Hydrophobizität der Schale abnimmt. Die Testung der Hautpenetration der CMS 1 - 3 wurde *in vitro* durchgeführt. Um die Eindringtiefe der CMS visuell bestimmen zu können, wurden diese mit dem Farbstoff Nilrot beladen. Mit Hilfe der CMS 1-3 konnte Nilrot erfolgreich in tiefe Hautschichten transportiert werden und im Vergleich zu herkömmlichen Cremes in jeder Hautschicht stark angereichert werden. Aufgrund der amphiphilen Struktur von CMS Nanocarriern findet die Hautaufnahme vermutlich in interzellulären Lipiden statt. Die zelluläre Aufnahme in Keratinozyten belegte die geringe Affinität von CMS und Corneozyten (endständig differenzierte Keranozyten). CMS Nanocarrier zeigten keine Zytotoxizität gegenüber HaCat-Zellen und es konnte keine Reizung von Rinderaugen beim BCOP-Test beobachtet werden. Zusätzlich können die CMS Nanocarrier aufgrund der IC-Impermeabilität als sichere und effiziente Carrier für die topische Wirkstofffreisetzung verwendet werden.

Im zweiten Teil fokussierten wir uns auf die *in vitro* Penetration in die Haut Tacrolimus-geladenen CMS Nanocarriern. Tacrolimus wurde effizient in CMS

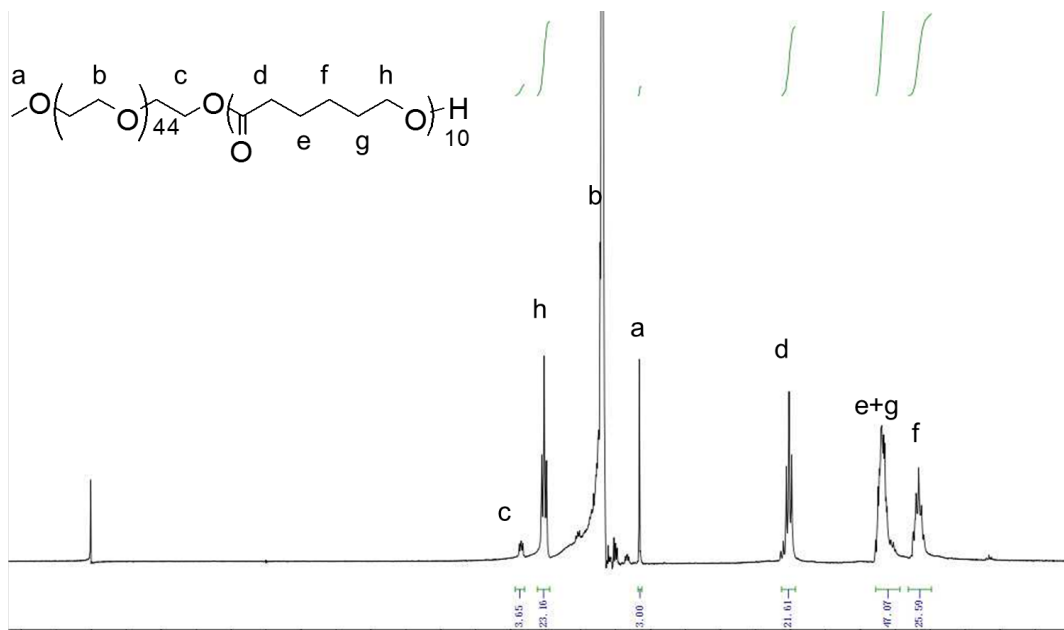
Nanocarrier mit Hilfe der Miniemulsionsmethode verkapselt. Stabile CMS Formulierungen mit einem vergleichbaren Tacrolimus-Gehalt wie das kommerziell erhältliche Produkt Protopic iontment wurden erfolgreich hergestellt. Tacrolimus wurde nicht schlagartig sondern kontinuierlich aus den CMS Nanocarriern freigesetzt (Freisetzung von ca. 30% Wirkstoff innerhalb von 7 Tagen). Die in vitro Penetration in die Haut zeigte, dass CMS Nanocarrier die Freisetzung von Tacrolimus in jeder Hautschicht signifikant erhöhen konnten und der Effekt sogar nach längerer Behandlungszeit verstärkt wurde.

Im dritten Projekt wurden kationische CMS mit lipophilen, tertiären Aminogruppen (CMS-DEA) für die topische Freisetzung von verschiedenen Substanzen konzipiert und zum Vergleich wurde ein CMS ohne geladene Gruppen (CMS-PCL) hergestellt. Aufgrund von Protonierung und Deprotonierung des tertiärenamins wurden Größe und Zetapotential des CMS-DEA signifikant durch den pH-Wert beeinflusst, während nur vernachlässigbare Änderungen im Fall des CMS-PCL beobachtet werden konnten. Um die Vielseitigkeit der CMS Nanocarrier zu demonstrieren, wurden der hydrophobe Wirkstoff Tacrolimus und das hydrophile Biomakromolekül BSA als Modelle für die Testung der Ladekapazität ausgewählt. CMS-DEA zeigte eine deutlich bessere Ladekapazität für beide Moleküle als das neutrale CMS-PCL. Die Freisetzung von Tacrolimus aus CMS-DEA wurde stark von der Änderung des pH-Wertes beeinflusst. Eine erhöhte Wirkstofffreisetzung wurde bei einem saurem pH-Wert beobachtet, womit der Carrier als smarter Carrier für die schlagartige Wirkstofffreisetzung eingesetzt werden kann. Im Gegensatz dazu ist die Wirkstofffreisetzung aus dem neutralen CMS-PCL unabhängig vom pH-Wert. Interaktionen zwischen CMS Carriern und SC Lipiden wurden mittels QCM bewertet, wobei aufgrund von elektrostatischen Kräften schnellere und stärkere Interaktionen zwischen Haut und CMS-DEA beobachtet werden konnten. Zur gleichen Zeit zeigten CMS-DEA bei ATR-FTIR-Messungen einen stärkeren Fluidisierungseffekt auf interzellulären Lipiden als CMS-PCL. Schließlich wurden sowohl Nilrot und FITC-BSA als Proben für die Penetration in die Haut verwendet. CMS-DEA ermöglichte

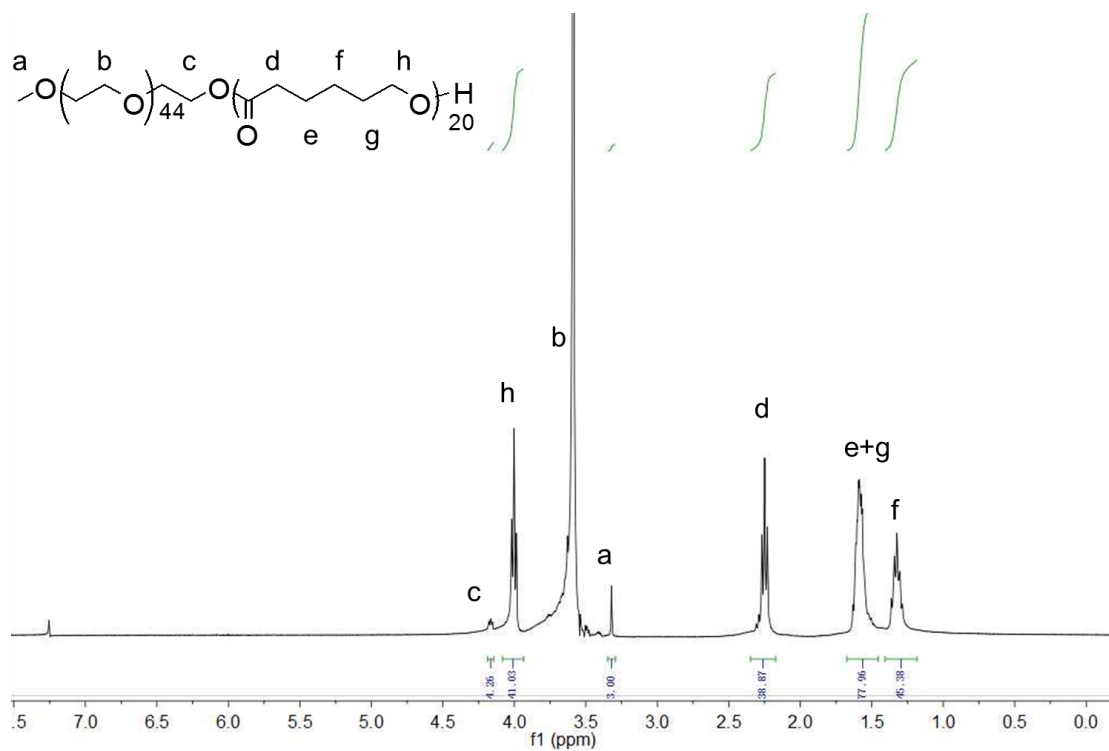
vergleichbare Freisetzungen von Nilrot wie CMS-PCL, während beide Substanzen besser waren als die konventionelle Creme. CMS-DEA zeigte jedoch bei der Freisetzung von FITC-BSA eine höhere Effizienz als CMS-PCL oder die Kontrolle ohne Carrier. Beide Carrier verblieben in der SC-Schicht ohne eine weitere Penetration in beschädigte SC-Schichten und zeigten somit eine geringe Hautreizung. Die CMS-DEA Carrier zeigten eine gute Bioverträglichkeit und eine geringfügige Zytotoxizität vergleichbar mit anderen Nanocarriern beispielsweise PEI, welche auf die kationischen Gruppen zurückzuführen ist. Die Bioverträglichkeit von CMS-DEA Nanocarriern kann weiter verbessert werden durch die Änderung des Funktionalisierungsgrades der DEA-Gruppen oder die Verwendung von tertiären Aminen mit einem Isoelektrischer Punkt (pI)-Wert kleiner als 7.4.



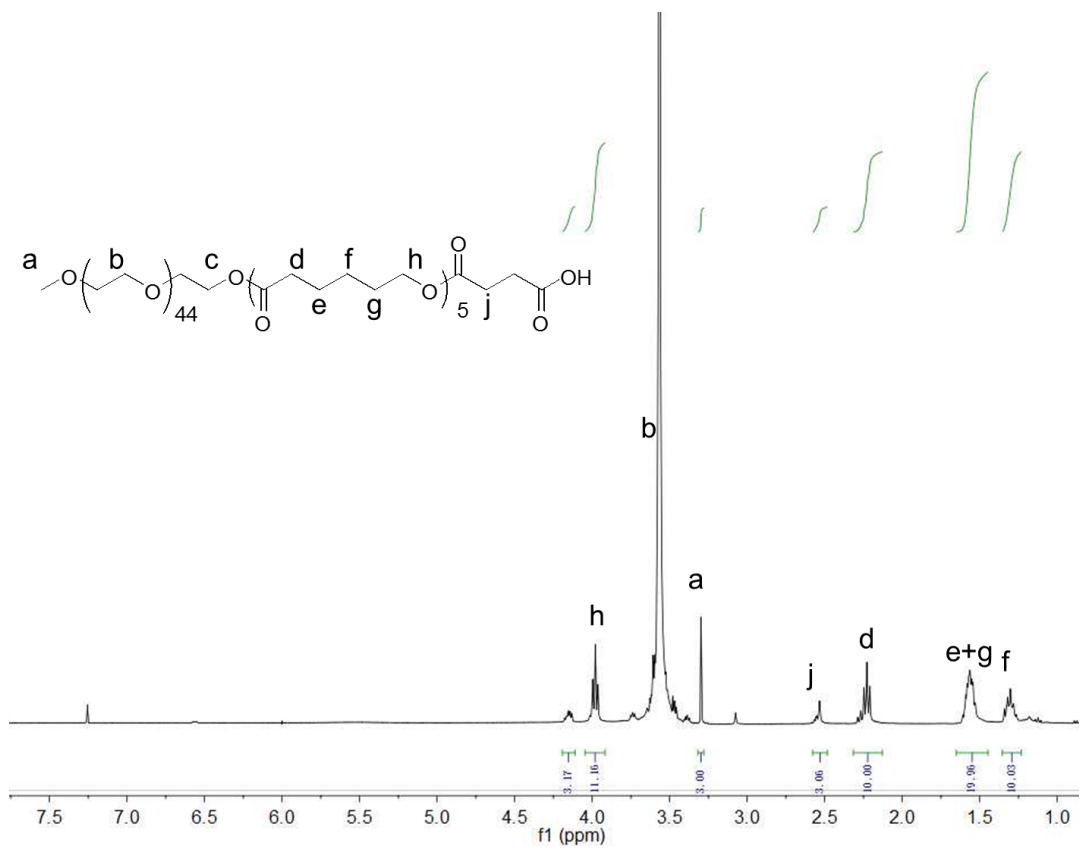




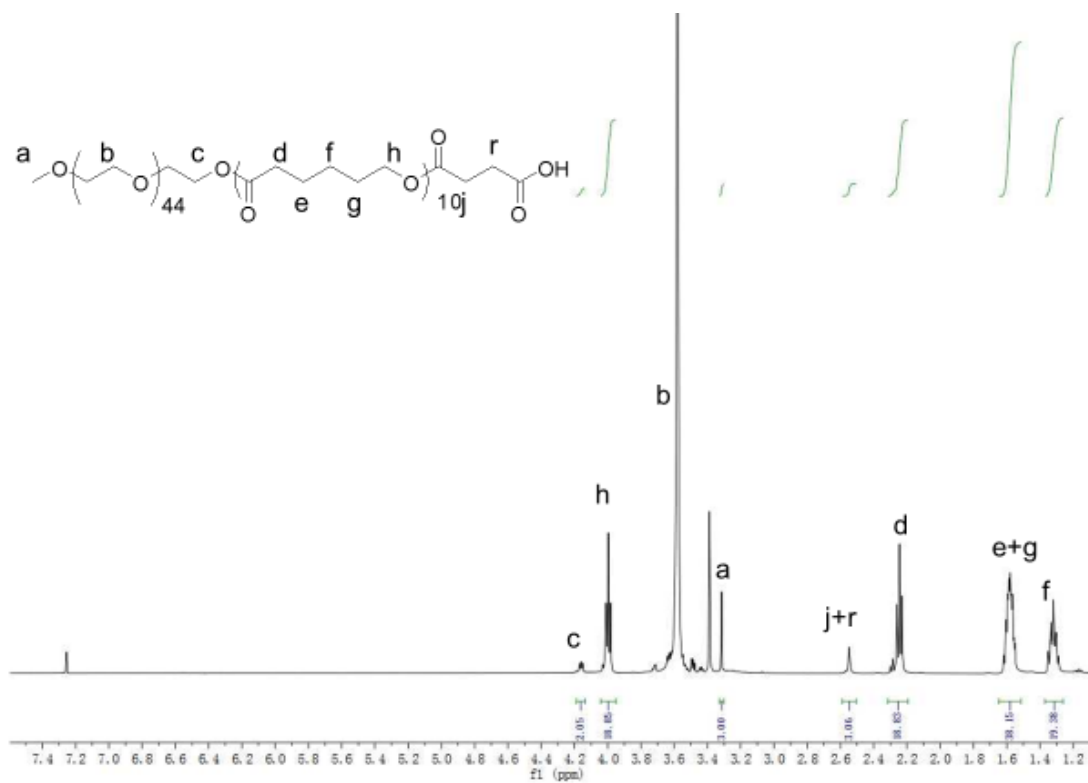
<sup>1</sup>H-NMR spectra (CDCl<sub>3</sub>, 298 K) of mPEG-PCL<sub>10</sub>-OH



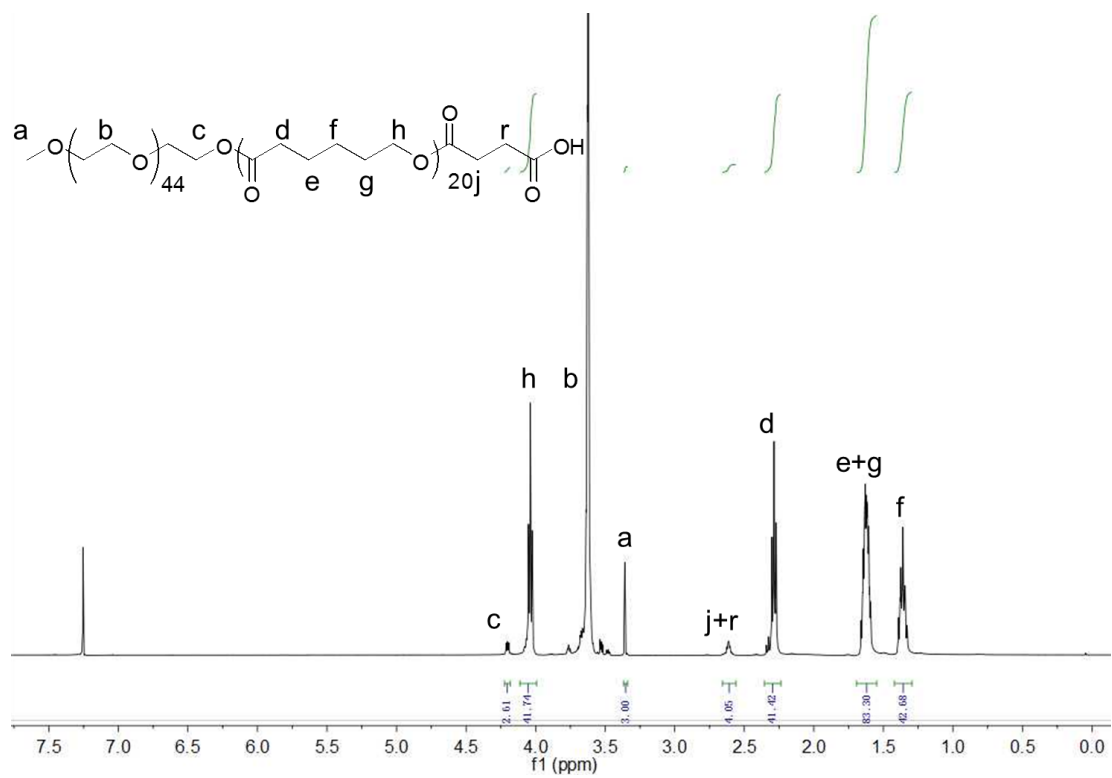
$^1\text{H-NMR}$  spectra (CDCl<sub>3</sub>, 298 K) of mPEG-PCL<sub>20</sub>-OH



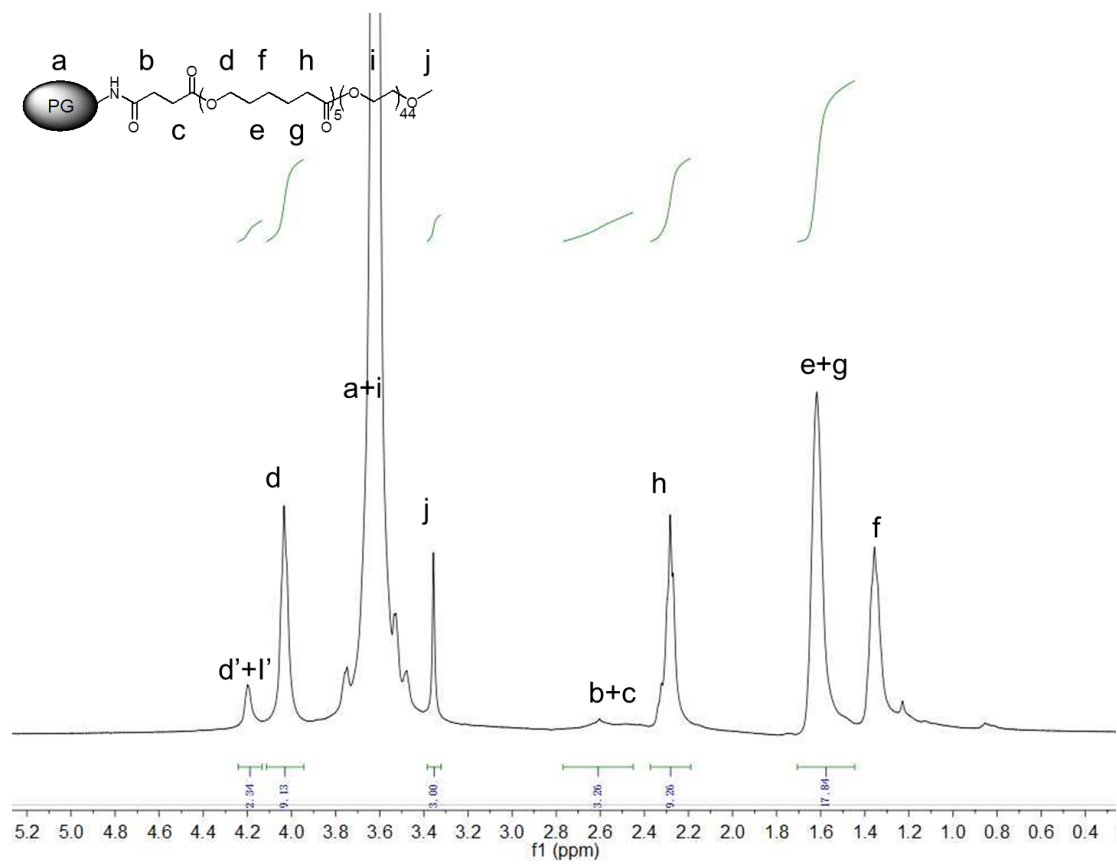
<sup>1</sup>H-NMR spectra (CDCl<sub>3</sub>, 298 K) of mPEG-PCL<sub>5</sub>-COOH



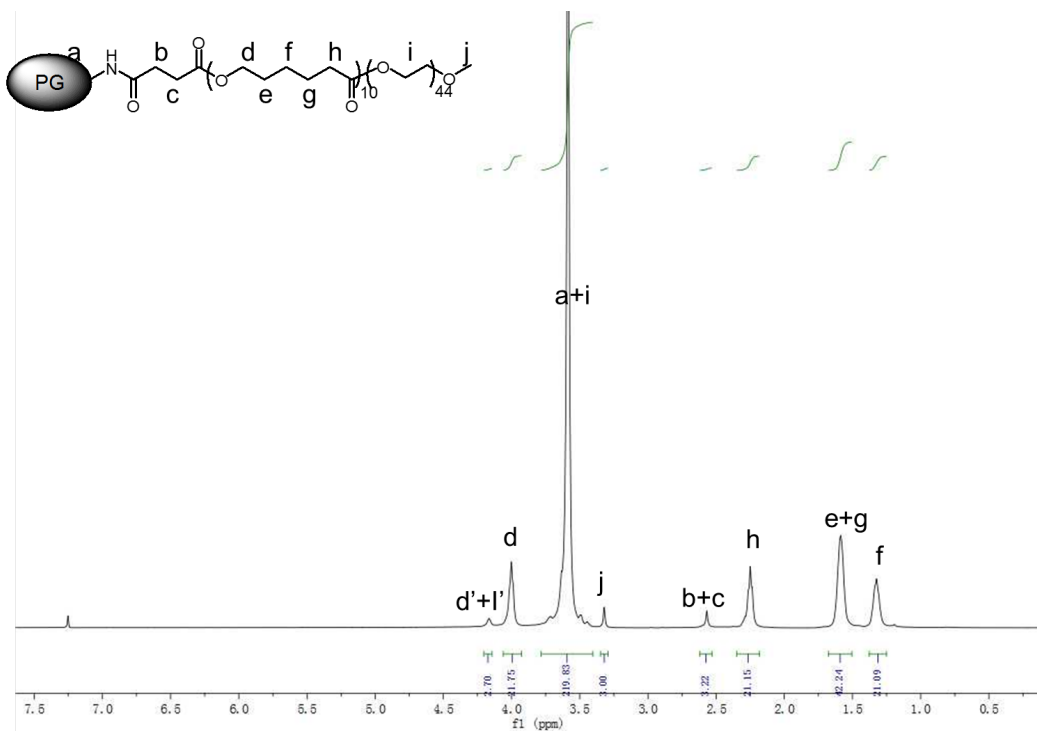
<sup>1</sup>H-NMR spectra (CDCl<sub>3</sub>, 298 K) of mPEG-PCL<sub>10</sub>-COOH



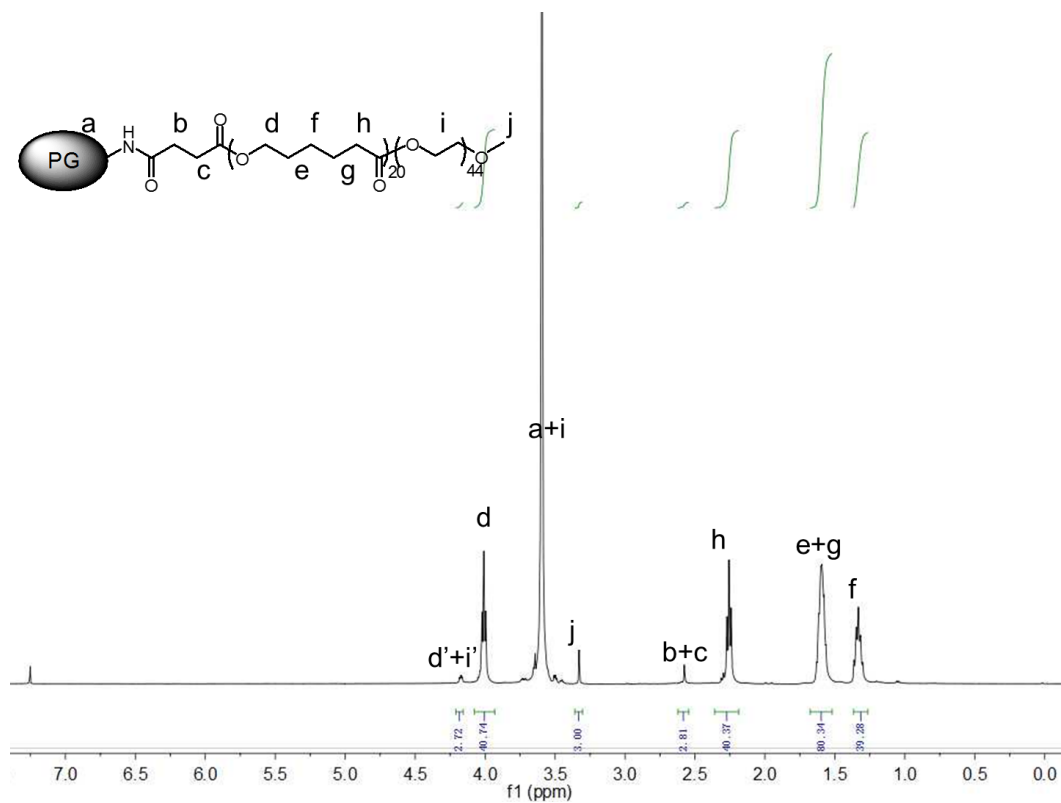
<sup>1</sup>H-NMR spectra (CDCl<sub>3</sub>, 298 K) of mPEG-PCL<sub>20</sub>-COOH



$^1\text{H-NMR}$  spectra (CDCl<sub>3</sub>, 298 K) of hPG-PCL<sub>5</sub>-mPEG (CMS 1)

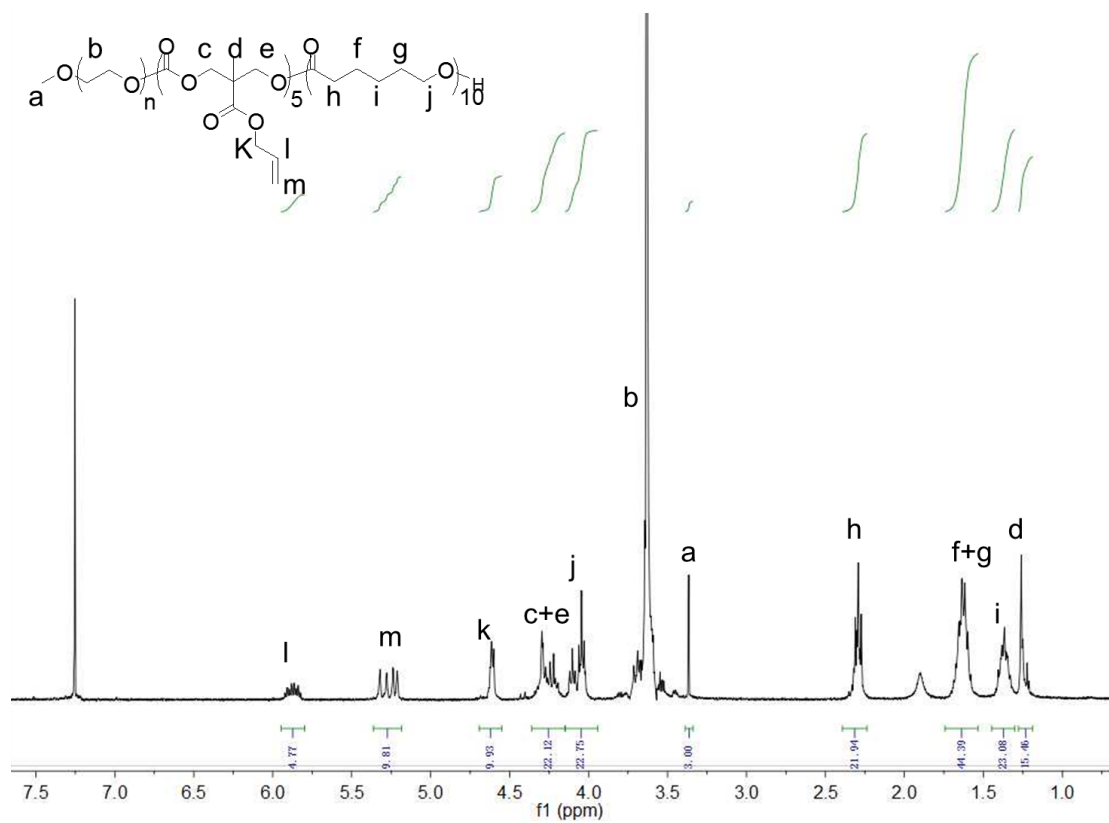


<sup>1</sup>H-NMR spectra (CDCl<sub>3</sub>, 298 K) of hPG-PCL<sub>10</sub>-mPEG (CMS 2)

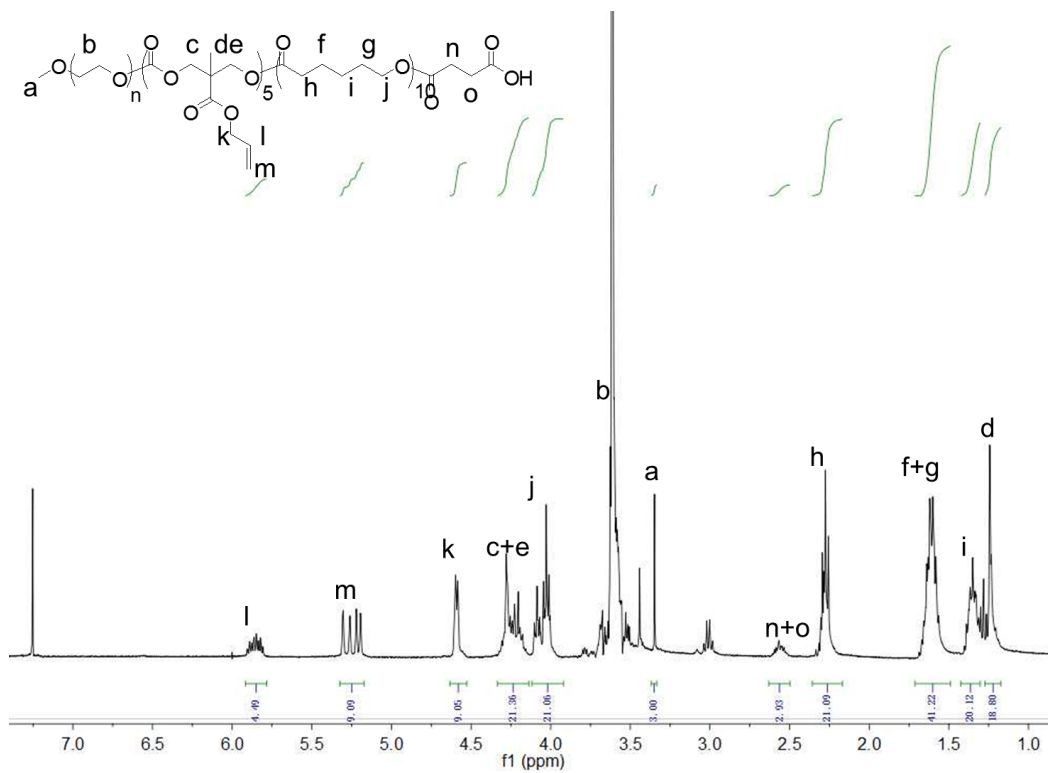


<sup>1</sup>H-NMR spectra (CDCl<sub>3</sub>, 298 K) of hPG-PCL<sub>20</sub>-mPEG (CMS 3)

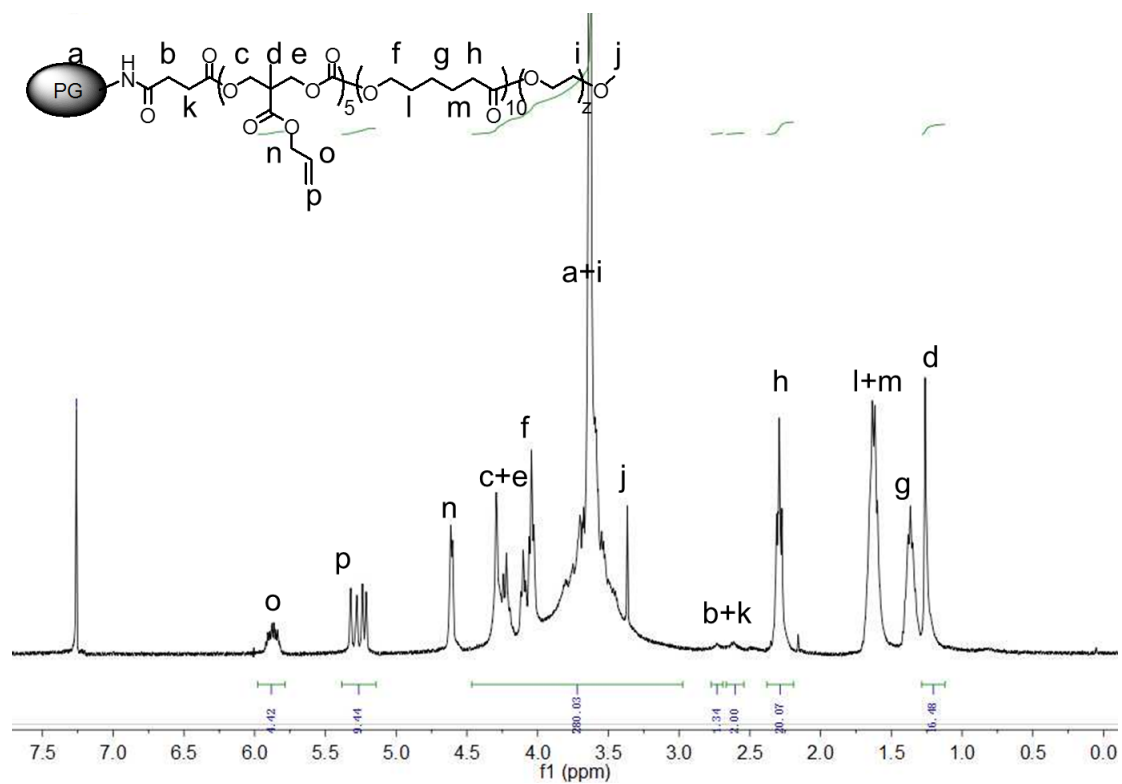




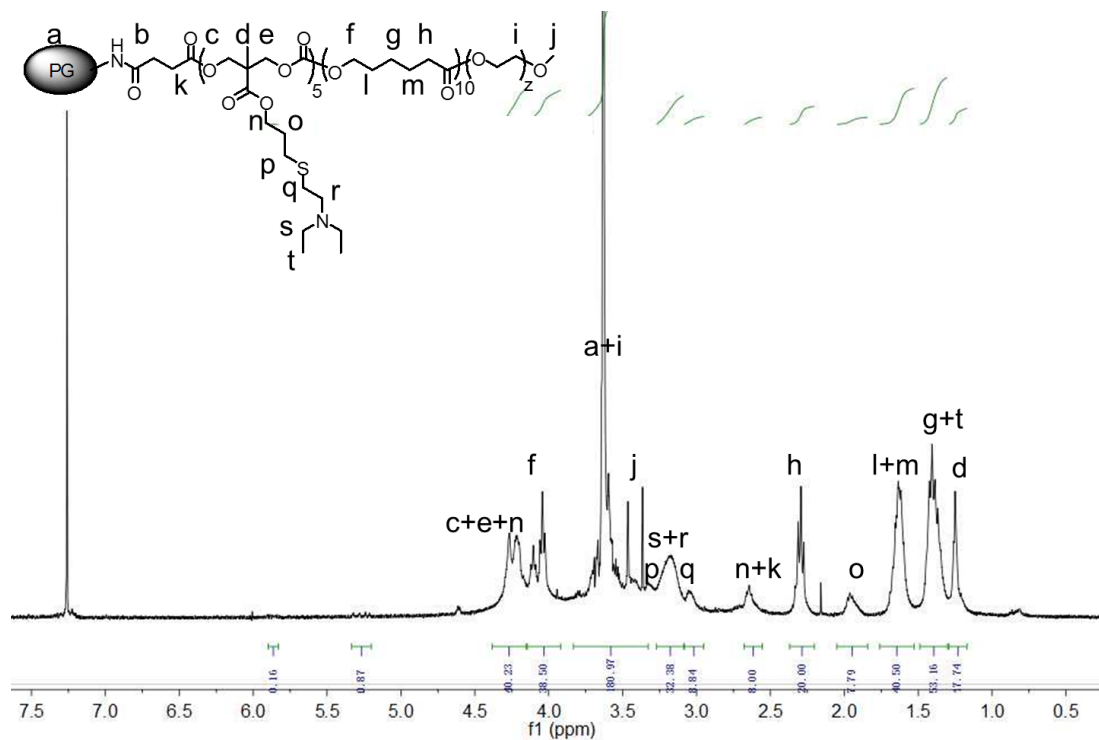
<sup>1</sup>H-NMR spectra (CDCl<sub>3</sub>, 298 K) of mPEG-P(MAC<sub>5</sub>-co-CL<sub>10</sub>)-OH



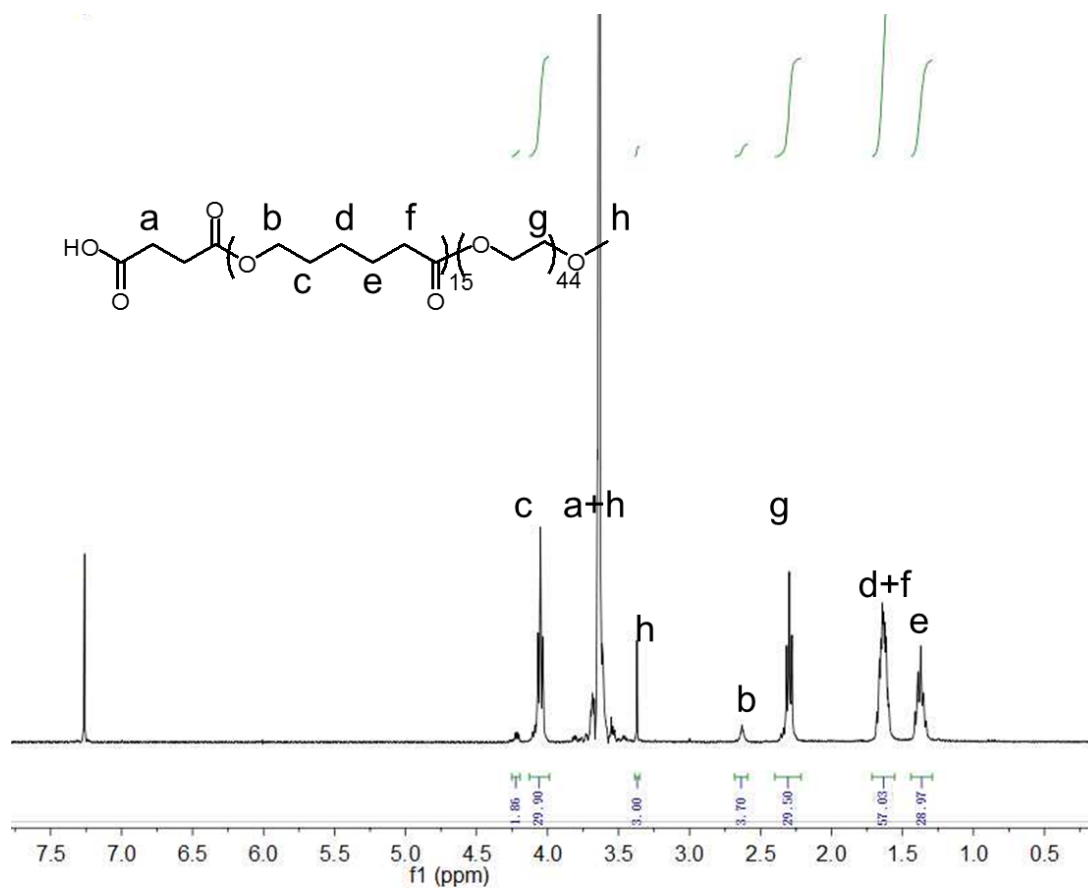
$^1\text{H-NMR}$  spectra ( $\text{CDCl}_3$ , 298 K) of  $\text{mPEG-P(MAC}_5\text{-co-CL}_{10}\text{)-COOH}$



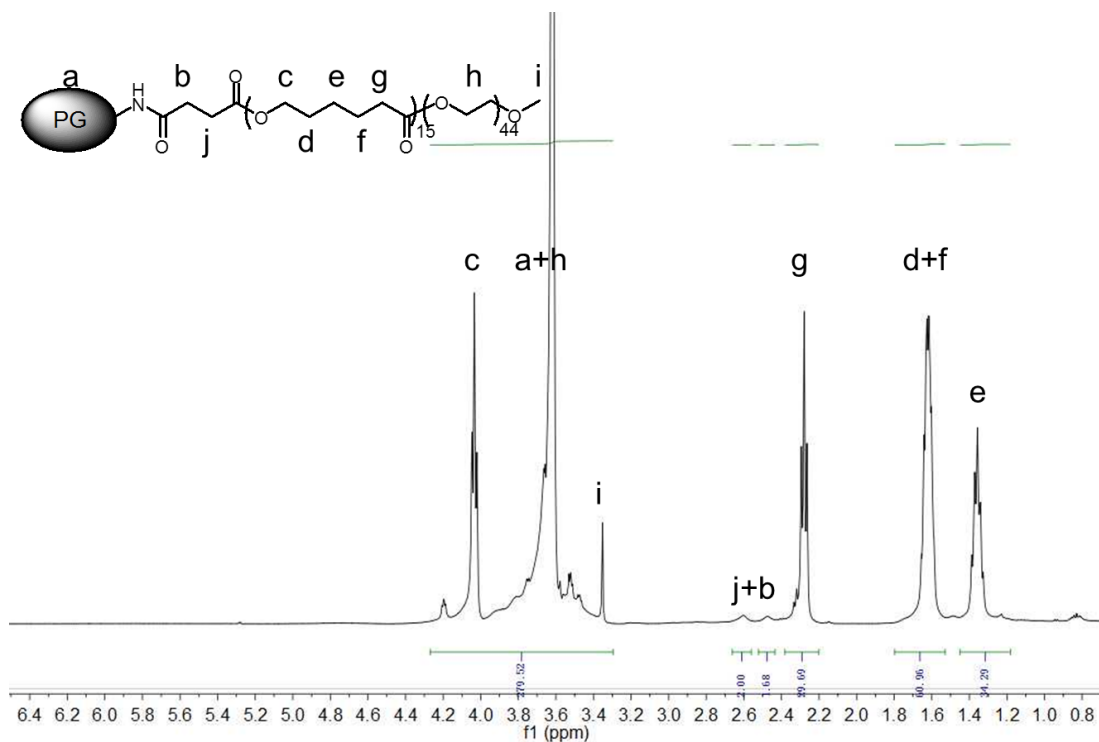
<sup>1</sup>H-NMR spectra (CDCl<sub>3</sub>, 298 K) of hPG-P(MAC<sub>5</sub>-co-CL<sub>10</sub>)-mPEG (CMS-MAC)



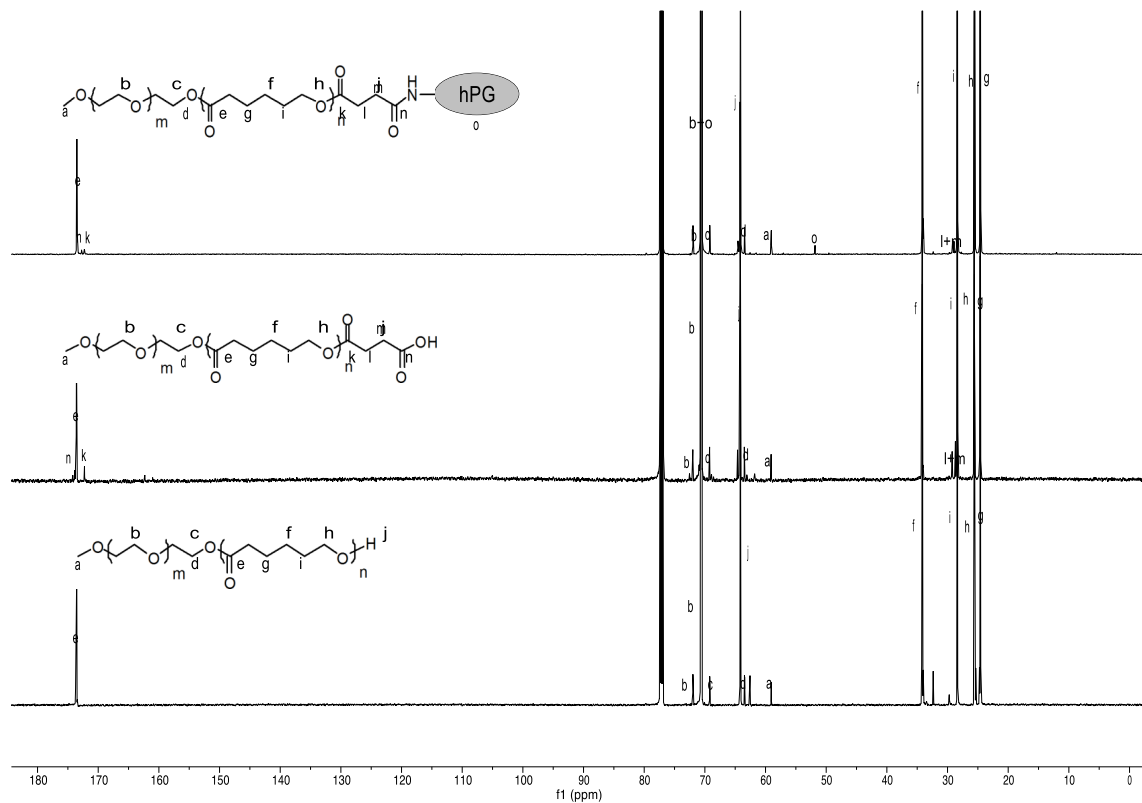
<sup>1</sup>H-NMR spectra (CDCl<sub>3</sub>, 298 K) of hPG-P(DEA<sub>5</sub>-co-CL<sub>10</sub>)-mPEG (CMS-DEA)



<sup>1</sup>H-NMR spectra (CDCl<sub>3</sub>, 298 K) of mPEG-PCL<sub>15</sub>-COOH

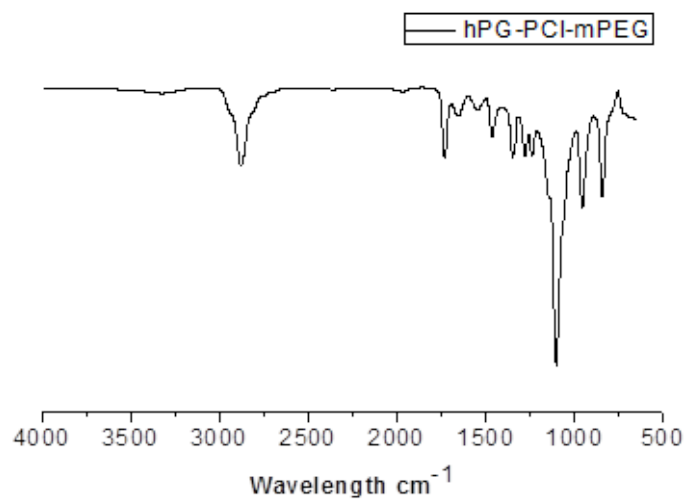
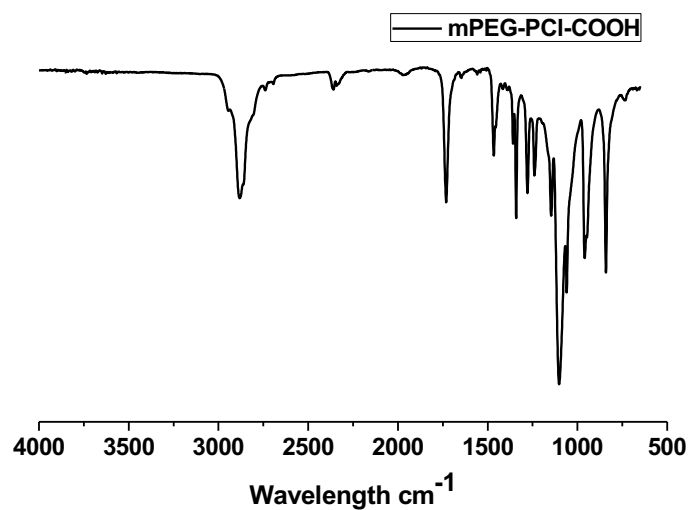
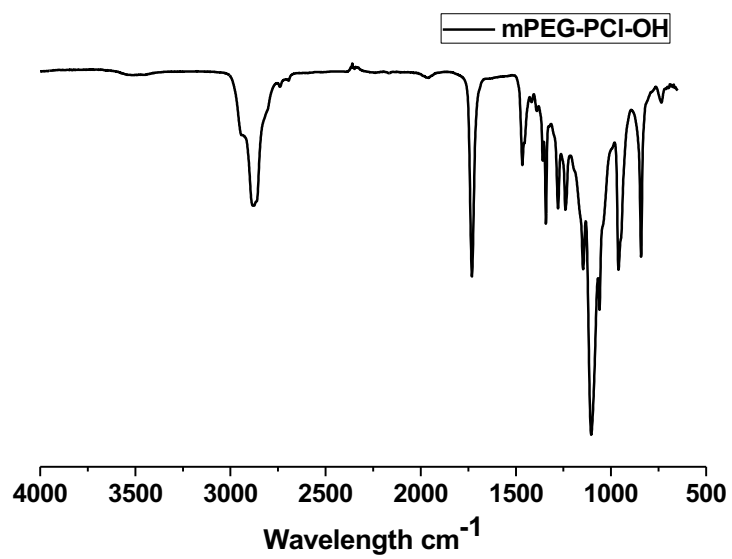


<sup>1</sup>H-NMR spectra (CDCl<sub>3</sub>, 298 K) of hPG-PCL<sub>15</sub>-mPEG (CMS-PCL)



$^{13}\text{C}$ -NMR spectra ( $\text{CDCl}_3$ , 298 K) of mPEG-PCL-OH, mPEG-PCL-COOH and hPG-PCL-mPEG (CMS)

## FTIR Spectra



FTIR spectra of mPEG-PCL-OH, mPEG-PCL-COOH and hPG-PCL-mPEG (CMS)



## References

- [1] V. Wagner, A. Dullaart, A.-K. Bock, A. Zweck, *Nat. Biotech.* **2006**, *24*, 1211-1217.
- [2] aK. E. Uhrich, S. M. Cannizzaro, R. S. Langer, K. M. Shakesheff, *Chem. Rev.* **1999**, *99*, 3181-3198; bE. Fleige, M. A. Quadir, R. Haag, *Adv. Drug Delivery Rev.* **2012**, *64*, 866-884.
- [3] Y. Barenholz, *J. Controlled Release* **2012**, *160*, 117-134.
- [4] R. Duncan, M. J. Vicent, *Adv. Drug Delivery Rev.* **2013**, *65*, 60-70.
- [5] M. M. A. Abdel-Mottaleb, C. Try, Y. Pellequer, A. Lamprecht, *Nanomedicine* **2014**, *9*, 1727-1743.
- [6] M. Boegh, H. M. Nielsen, *Basic Clin. Pharmacol. Toxicol.* **2015**, *116*, 179-186.
- [7] aE. Blanco, H. Shen, M. Ferrari, *Nat. Biotech.* **2015**, *33*, 941-951; bS. Barua, S. Mitragotri, *Nano Today* **2014**, *9*, 223-243.
- [8] J. M. Scherrmann, *Vasc. Pharmacol.* **2002**, *38*, 349-354.
- [9] M. Longmire, P. L. Choyke, H. Kobayashi, *Nanomedicine* **2008**, *3*, 703-717.
- [10] L. Ilium, I. M. Hunneyball, S. S. Davis, *Int. J. Pharm.* **1986**, *29*, 53-65.
- [11] F. Danhier, O. Feron, V. Préat, *J. Controlled Release* **2010**, *148*, 135-146.
- [12] H. Maeda, T. Sawa, T. Konno, *J. Controlled Release* **2001**, *74*, 47-61.
- [13] aH. Maeda, G. Y. Bharate, J. Daruwalla, *Eur. J. Pharm. Biopharm.* **2009**, *71*, 409-419; bR. Haag, F. Kratz, *Angew. Chem. Int. Ed.* **2006**, *45*, 1198-1215.
- [14] H. Cabral, Y. Matsumoto, K. Mizuno, Q. Chen, M. Murakami, M. Kimura, Y. Terada, M. R. Kano, K. Miyazono, M. Uesaka, N. Nishiyama, K. Kataoka, *Nat. Nanotechnol.* **2011**, *6*, 815.
- [15] H.-J. Li, J.-Z. Du, J. Liu, X.-J. Du, S. Shen, Y.-H. Zhu, X. Wang, X. Ye, S. Nie, J. Wang, *ACS Nano* **2016**, *10*, 6753-6761.
- [16] J. Lu, S. C. Owen, M. S. Shoichet, *Macromolecules* **2011**, *44*, 6002-6008.
- [17] R. D. Vinluan, J. Zheng, *Nanomedicine* **2015**, *10*, 2781-2794.
- [18] Y.-Y. Wang, S. K. Lai, J. S. Suk, A. Pace, R. Cone, J. Hanes, *Angew. Chem. Int.*

- Ed.* **2008**, *47*, 9726-9729.
- [19] S.-T. Yang, Y. Liu, Y.-W. Wang, A. Cao, *Small* **2013**, *9*, 1635-1653.
- [20] N. J. Butcher, G. M. Mortimer, R. F. Minchin, *Nat. Nanotechnol.* **2016**, *11*, 310-311.
- [21] aS. Schöttler, G. Becker, S. Winzen, T. Steinbach, K. Mohr, K. Landfester, V. Mailänder, F. R. Wurm, *Nat. Nanotechnol.* **2016**, *11*, 372-377; bS.-D. Li, L. Huang, *J. controlled release* **2010**, *145*, 178-181.
- [22] E. Wenande, L. H. Garvey, *Clinical & Experimental Allergy* **2016**, *46*, 907-922.
- [23] aY. Deng, J. K. Saucier-Sawyer, C. J. Hoimes, J. Zhang, Y.-E. Seo, J. W. Andrejcsk, W. M. Saltzman, *Biomaterials* **2014**, *35*, 6595-6602; bA. Thomas, S. S. Müller, H. Frey, *Biomacromolecules* **2014**, *15*, 1935-1954.
- [24] B. Kang, P. Okwieka, S. Schöttler, O. Seifert, R. E. Kontermann, K. Pfizenmaier, A. Musyanovych, R. Meyer, M. Diken, U. Sahin, V. Mailänder, F. R. Wurm, K. Landfester, *Biomaterials* **2015**, *49*, 125-134.
- [25] Z. Cao, S. Jiang, *Nano Today* **2012**, *7*, 404-413.
- [26] R. P. Brannigan, A. P. Dove, *Biomater. Sci.* **2017**, *5*, 9-21.
- [27] N. Kamaly, B. Yameen, J. Wu, O. C. Farokhzad, *Chem. Rev.* **2016**, *116*, 2602-2663.
- [28] H. Tan, C. R. Chu, K. A. Payne, K. G. Marra, *Biomaterials* **2009**, *30*, 2499-2506.
- [29] aM. Trollsås, V. Y. Lee, D. Mecerreyes, P. Löwenhielm, M. Möller, R. D. Miller, J. L. Hedrick, *Macromolecules* **2000**, *33*, 4619-4627; bS. Tempelaar, L. Mespouille, O. Coulembier, P. Dubois, A. P. Dove, *Chem. Soc. Rev.* **2013**, *42*, 1312-1336.
- [30] A.-C. Albertsson, I. K. Varma, *Biomacromolecules* **2003**, *4*, 1466-1486.
- [31] C. Cai, J. Lin, Y. Lu, Q. Zhang, L. Wang, *Chem. Soc. Rev.* **2016**, *45*, 5985-6012.
- [32] B. D. Ulery, L. S. Nair, C. T. Laurencin, *J. Polym. Sci. Part B, Pol. phys.* **2011**, *49*, 832-864.
- [33] P. Grossen, D. Witzigmann, S. Sieber, J. Huwyler, *J. Controlled Release* **2017**, *260*, 46-60.

- [34] S. A. Mirmohammadi, M. Imani, H. Uyama, M. Atai, M. B. Teimouri, N. Bahri-Lale, *Polym. Int.* **2014**, *63*, 479-485.
- [35] aY. Shibasaki, H. Sanada, M. Yokoi, F. Sanda, T. Endo, *Macromolecules* **2000**, *33*, 4316-4320; bD. Bourissou, B. Martin-Vaca, A. Dumitrescu, M. Graullier, F. Lacombe, *Macromolecules* **2005**, *38*, 9993-9998.
- [36] M. S. Kim, K. S. Seo, G. Khang, H. B. Lee, *Macromol. Rapid Commun.* **2005**, *26*, 643-648.
- [37] J. Ling, J. Shen, T. E. Hogen-Esch, *Polymer* **2009**, *50*, 3575-3581.
- [38] A. Kowalski, A. Duda, S. Penczek, *Macromolecules* **2000**, *33*, 689-695.
- [39] B. Parrish, R. B. Breitenkamp, T. Emrick, *J. Am. Chem. Soc.* **2005**, *127*, 7404-7410.
- [40] Y. Zhou, R.-X. Zhuo, Z.-L. Liu, *Macromol. Rapid Commun.* **2005**, *26*, 1309-1314.
- [41] X. Hu, X. Chen, S. Liu, Q. Shi, X. Jing, *J. Polym. Sci., Part A: Polym. Chem.* **2008**, *46*, 1852-1861.
- [42] S. Tempelaar, L. Mespouille, P. Dubois, A. P. Dove, *Macromolecules* **2011**, *44*, 2084-2091.
- [43] X. Zhang, S. Malhotra, M. Molina, R. Haag, *Chem. Soc. Rev.* **2015**, *44*, 1948-1973.
- [44] R. Trivedi, U. B. Kompella, *Nanomedicine* **2010**, *5*, 485-505.
- [45] aY. Masayuki, M. Mizue, Y. Noriko, O. Teruo, S. Yasuhisa, K. Kazunori, I. Shohei, *J. Controlled Release* **1990**, *11*, 269-278; bK. Yasugi, Y. Nagasaki, M. Kato, K. Kataoka, *J. Controlled Release* **1999**, *62*, 89-100.
- [46] N. Nishiyama, M. Yokoyama, T. Aoyagi, T. Okano, Y. Sakurai, K. Kataoka, *Langmuir* **1999**, *15*, 377-383.
- [47] aP. Venkatesan, Y. Cheng, D. Kahne, *J. Am. Chem. Soc.* **1994**, *116*, 6955-6956; bS. H. Kim, J. P. K. Tan, F. Nederberg, K. Fukushima, J. Colson, C. Yang, A. Nelson, Y.-Y. Yang, J. L. Hedrick, *Biomaterials* **2010**, *31*, 8063-8071.
- [48] E.-J. Cha, J. E. Kim, C.-H. Ahn, *Eur. J. Pharm. Sci.* **2009**, *38*, 341-346.

- [49] M. Yokoyama, S. Inoue, K. Kataoka, N. Yui, T. Okano, Y. Sakurai, *Makromol. Chem.* **1989**, *190*, 2041-2054.
- [50] T. Nakanishi, S. Fukushima, K. Okamoto, M. Suzuki, Y. Matsumura, M. Yokoyama, T. Okano, Y. Sakurai, K. Kataoka, *J. Controlled Release* **2001**, *74*, 295-302.
- [51] aC. Yang, A. B. Ebrahim Attia, J. P. K. Tan, X. Ke, S. Gao, J. L. Hedrick, Y.-Y. Yang, *Biomaterials* **2012**, *33*, 2971-2979; bA. B. Ebrahim Attia, C. Yang, J. P. K. Tan, S. Gao, D. F. Williams, J. L. Hedrick, Y.-Y. Yang, *Biomaterials* **2013**, *34*, 3132-3140.
- [52] Y. Li, W. Xiao, K. Xiao, L. Berti, J. Luo, H. P. Tseng, G. Fung, K. S. Lam, *Angew. Chem. Int. Ed.* **2012**, *51*, 2864-2869.
- [53] I. N. Kurniasih, J. Keilitz, R. Haag, *Chem. Soc. Rev.* **2015**, *44*, 4145-4164.
- [54] aD. Steinhilber, M. Witting, X. Zhang, M. Staegemann, F. Paulus, W. Friess, S. Küchler, R. Haag, *J. Controlled Release* **2013**, *169*, 289-295; bX. Zhang, K. Achazi, D. Steinhilber, F. Kratz, J. Dervede, R. Haag, *J. Controlled Release* **2014**, *174*, 209-216.
- [55] aM. K. Calabretta, A. Kumar, A. M. McDermott, C. Cai, *Biomacromolecules* **2007**, *8*, 1807-1811; bY. Zhao, X. Shuai, C. Chen, F. Xi, *Chem. Mater.* **2003**, *15*, 2836-2843.
- [56] aS. Stefani, I. N. Kurniasih, S. K. Sharma, C. Bottcher, P. Servin, R. Haag, *Polym. Chem.* **2016**, *7*, 887-898; bK. Walker, J.-F. Stumbé, R. Haag, *Polymers* **2016**, *8*, 192.
- [57] aM. Zheng, Y. Liu, O. Samsonova, T. Endres, O. Merkel, T. Kissel, *Int. J. Pharm.* **2012**, *427*, 80-87; bM. A. Quadir, M. R. Radowski, F. Kratz, K. Licha, P. Hauff, R. Haag, *J. Controlled Release* **2008**, *132*, 289-294.
- [58] aE. Burakowska, R. Haag, *Macromolecules* **2009**, *42*, 5545-5550; bM. R. Radowski, A. Shukla, H. von Berlepsch, C. Böttcher, G. Pickaert, H. Rehage, R. Haag, *Angew. Chem. Int. Ed.* **2007**, *46*, 1265-1269.
- [59] D. Yan, Y. Zhou, J. Hou, *Science* **2004**, *303*, 65-67.

- [60] E. Fleige, B. Ziem, M. Grabolle, R. Haag, U. Resch-Genger, *Macromolecules* **2012**, *45*, 9452-9459.
- [61] I. N. Kurniasih, H. Liang, S. Kumar, A. Mohr, S. K. Sharma, J. P. Rabe, R. Haag, *J. Mater. Chem. B* **2013**, *1*, 3569-3577.
- [62] J. Liu, Y. Pang, W. Huang, X. Huang, L. Meng, X. Zhu, Y. Zhou, D. Yan, *Biomacromolecules* **2011**, *12*, 1567-1577.
- [63] L. Zhao, G. Chen, J. Li, Y. Fu, T. A. Mavlyutov, A. Yao, R. W. Nickells, S. Gong, L.-W. Guo, *J. Controlled Release* **2017**, *247*, 153-166.
- [64] S. Stefani, S. Honzke, J. L. C. Camacho, F. Neumann, A. K. Prasad, S. Hedtrich, R. Haag, P. Servin, *Polymer* **2016**, *96*, 156-166.
- [65] aN. Alnasif, C. Zoschke, E. Fleige, R. Brodewolf, A. Boreham, E. Rühl, K.-M. Eckl, H.-F. Merk, H. C. Hennies, U. Alexiev, R. Haag, S. Kuchler, M. Schäfer-Korting, *J. Control. Release* **2014**, *185* 45-50; bS. Kuchler, M. R. Radowski, T. Blaschke, M. Dathe, J. Plendl, R. Haag, M. Schäfer-Korting, K. D. Kramer, *Eur. J. Pharm. Biopharm.* **2009**, *71*, 243-250.
- [66] aJ. Keilitz, M. Schwarze, S. Nowag, R. Schomäcker, R. Haag, *ChemCatChem* **2010**, *2*, 863-870; bM. Schwarze, J. Keilitz, S. Nowag, R. Y. Parapat, R. Haag, R. Schomäcker, *Langmuir* **2011**, *27*, 6511-6518.
- [67] M. R. Radowski, A. Shukla, H. von Berlepsch, C. Böttcher, G. Pickaert, H. Rehage, R. Haag, *Angew. Chem. Int. Ed.* **2007**, *119*, 1287-1292.
- [68] E. Fleige, K. Achazi, K. Schaletzki, T. Triemer, R. Haag, *J. Controlled Release* **2014**, *185*, 99-108.
- [69] M. Brazil, *Nat. Rev. Drug. Discov.* **2005**, *4*, 372-373.
- [70] M. R. Prausnitz, S. Mitragotri, R. Langer, *Nat. Rev. Drug. Discov.* **2004**, *3*, 115-124.
- [71] J. D. Bos, M. M. H. M. Meinardi, *Exp. Dermatol.* **2000**, *9*, 165-169.
- [72] J. A. Bouwstra, P. L. Honeywell-Nguyen, *Adv. Drug Delivery Rev.* **2002**, *54*, S41-S55.
- [73] aL. M. Russell, S. Wiedersberg, M. B. Delgado-Charro, *Eur. J. pharm.*

- biopharm.* **2008**, *69*, 861-870; bT. Marjukka Suhonen, J. A. Bouwstra, A. Urtti, *J. Controlled Release* **1999**, *59*, 149-161.
- [74] C. R. Harding, *Dermatol. Ther.* **2004**, *17*, 6-15.
- [75] E. Candi, R. Schmidt, G. Melino, *Nat. Rev. Mol. Cell Bio.* **2005**, *6*, 328-340.
- [76] M. Haftek, *Cell Tissue Res.* **2015**, *360*, 483-490.
- [77] G. Cevc, *Adv. Drug Delivery Rev.* **2004**, *56*, 675-711.
- [78] I. Iwai, H. Han, L. d. Hollander, S. Svensson, L.-G. Öfverstedt, J. Anwar, J. Brewer, M. Bloksgaard, A. Laloeuf, D. Nosek, S. Masich, L. A. Bagatolli, U. Skoglund, L. Norlén, *J. Invest. Dermatol.* **2012**, *132*, 2215-2225.
- [79] H. Xu, L. Timares, C. A. Elmets, in *Clinical Immunology (Fourth Edition)* (Eds.: T. A. Fleisher, W. T. Shearer, H. W. Schroeder, A. J. Frew, C. M. Weyand), London, **2013**, pp. 228-238.
- [80] S. D. White, J. A. Yager, *Vet. Dermatol.* **1995**, *6*, 1-8.
- [81] L. Rittié, G. J. Fisher, *Cold Spring Harb. Perspect. Med.* **2015**, *5*, a015370.
- [82] L. T. Smith, K. A. Holbrook, P. H. Byers, *J. Invest. Dermatol.* **1982**, *79*, 93-104.
- [83] D. D. Verma, S. Verma, G. Blume, A. Fahr, *Eur. J. Pharm. Biopharm.* **2003**, *55*, 271-277.
- [84] S. A. Wissing, R. H. Müller, *J. Control. Release* **2002**, *81*, 225-233.
- [85] aV. R. Leite-Silva, W. Y. Sanchez, H. Studier, D. C. Liu, Y. H. Mohammed, A. M. Holmes, E. M. Ryan, I. N. Haridass, N. C. Chandrasekaran, W. Becker, J. E. Grice, H. A. E. Benson, M. S. Roberts, *Eur. J. Pharm. Biopharm.* **2016**, *104*, 140-147; bM. Crosera, A. Prodi, M. Mauro, M. Pelin, C. Florio, F. Bellomo, G. Adami, P. Apostoli, G. De Palma, M. Bovenzi, M. Campanini, F. Larese Filon, *Int. J. Environ. Res. Public Health* **2015**, *12*, 9282-9297; cF. Larese Filon, M. Crosera, G. Adami, M. Bovenzi, F. Rossi, G. Maina, *Nanotoxicology* **2011**, *5*, 493-501.
- [86] D. Šmejkalová, T. Muthný, K. Nešporová, M. Hermannová, E. Achbergerová, G. Huerta-Angeles, M. Svoboda, M. Čepa, V. Machalová, D. Luptáková, V. Velebný, *Carbohydr. Polym.* **2017**, *156*, 86-96.

- [87] F. Rancan, M. Asadian-Birjand, S. Dogan, C. Graf, L. Cuellar, S. Lommatzsch, U. Blume-Peytavi, M. Calderón, A. Vogt, *J. Controlled Release* **2016**, *228*, 159-169.
- [88] P. Desai, R. R. Patlolla, M. Singh, *Mol.membr. bio.* **2010**, *27*, 247-259.
- [89] G. Sonavane, K. Tomoda, A. Sano, H. Ohshima, H. Terada, K. Makino, *Colloids Surf. B Biointerfaces* **2008**, *65*, 1-10.
- [90] L. Sun, Z. Liu, L. Wang, D. Cun, H. H. Y. Tong, R. Yan, X. Chen, R. Wang, Y. Zheng, *J. Controlled Release* **2017**, *254*, 44-54.
- [91] S. Wang, D. Zeng, J. Niu, H. Wang, L. Wang, Q. Li, C. Li, H. Song, J. Chang, L. Zhang, *J. Mater. Chem. B* **2014**, *2*, 877-884.
- [92] Y. Yang, S. Sunoqrot, C. Stowell, J. Ji, C.-W. Lee, J. W. Kim, S. A. Khan, S. Hong, *Biomacromolecules* **2012**, *13*, 2154-2162.
- [93] aN. Dragicevic-Curic, S. Gräfe, B. Gitter, S. Winter, A. Fahr, *Int. J. Pharm.* **2010**, *384*, 100-108; bL. Montenegro, A. M. Panico, A. Ventimiglia, F. P. Bonina, *Int. J. Pharm.* **1996**, *133*, 89-96.
- [94] Y.-K. Song, C.-K. Kim, *Biomaterials* **2006**, *27*, 271-280.
- [95] Y. Yang, R. M. Pearson, O. Lee, C.-W. Lee, R. T. Chatterton, S. A. Khan, S. Hong, *Adv. Funct. Mater.* **2014**, *24*, 2442-2449.
- [96] R. Bleul, R. Thiermann, M. Maskos, *Macromolecules* **2015**, *48*, 7396-7409.
- [97] M. Lapteva, K. Mondon, M. Möller, R. Gurny, Y. N. Kalia, *Mol. Pharm.* **2014**, *11*, 2989-3001.
- [98] aV. V. K. Venuganti, O. P. Perumal, *Int. J. Pharm.* **2008**, *361*, 230-238; bV. V. K. Venuganti, O. P. Perumal, *J. Pharm. Sci.*, *98*, 2345-2356.
- [99] D. E. Poree, M. D. Giles, L. B. Lawson, J. He, S. M. Grayson, *Biomacromolecules* **2011**, *12*, 898-906.
- [100] aS. Kuchler, M. Abdel-Mottaleb, A. Lamprecht, M. R. Radowski, R. Haag, M. Schäfer-Korting, *Int. J. Pharm.* **2009**, *377*, 169-172; bS. Hönzke, C. Gerecke, A. Elpelt, N. Zhang, M. Unbehauen, V. Kral, E. Fleige, F. Paulus, R. Haag, M. Schäfer-Korting, B. Kleuser, S. Hedtrich, *J. Controlled Release* **2016**, *242*, 50-

63.

- [101] K. Yamamoto, A. Klossek, R. Flesch, T. Ohigashi, E. Fleige, F. Rancan, J. Frombach, A. Vogt, U. Blume-Peytavi, P. Schrade, S. Bachmann, R. Haag, S. Hedtrich, M. Schäfer-Korting, N. Kosugi, E. Rühl, *J. Controlled Release* **2016**, *242*, 64-70.
- [102] S. Kuchler, M. R. Radowski, T. Blaschke, M. Dathe, J. Plendl, R. Haag, M. Schäfer-Korting, K. D. Kramer, *Eur. J. Pharm. Biopharm.* **2009**, *71*, 243-250.
- [103] N. Alnasif, C. Zoschke, E. Fleige, R. Brodewolf, A. Boreham, E. Rühl, K.-M. Eckl, H.-F. Merk, H. C. Hennies, U. Alexiev, R. Haag, S. Kuchler, M. Schäfer-Korting, *J. Controlled Release*, *185*, 45-50.
- [104] M. G. Carstens, J. J. L. Bevernage, C. F. van Nostrum, M. J. van Steenberg, F. M. Flesch, R. Verrijck, L. G. J. de Leede, D. J. A. Crommelin, W. E. Hennink, *Macromolecules* **2007**, *40*, 116-122.
- [105] Y. He, Y. Inoue, *Polym. Int.* **2000**, *49*, 623-626.
- [106] R. K. Kainthan, C. Mugabe, H. M. Burt, D. E. Brooks, *Biomacromolecules* **2008**, *9*, 886-895.
- [107] X. J. Cai, A. Woods, P. Mesquida, S. A. Jones, *Mol. Pharm.* **2016**, *13*, 1375-1384.
- [108] C. Gerecke, A. Edlich, M. Giubudagian, F. Schumacher, N. Zhang, A. Said, G. Yealland, S. B. Lohan, F. Neumann, M. C. Meinke, N. Ma, M. Calderón, S. Hedtrich, M. Schäfer-Korting, B. Kleuser, *Nanotoxicology* **2017**, *11*, 267-277.
- [109] aM. de Jager, W. Groenink, J. van der Spek, C. Janmaat, G. Gooris, M. Ponc, J. Bouwstra, *Biochim. Biophys. Acta (BBA) - Biomembranes* **2006**, *1758*, 636-644; bD. Lee, J. N. Ashcraft, E. Verploegen, E. Pashkovski, D. A. Weitz, *Langmuir* **2009**, *25*, 5762-5766.
- [110] S. Belegriou, I. Mannelli, P. Lisboa, F. Bretagnol, A. Valsesia, G. Ceccone, P. Colpo, H. Rauscher, F. Rossi, *Langmuir* **2008**, *24*, 7251-7261.
- [111] aM. Boncheva, F. Damien, V. Normand, *Biochim. Biophys. Acta (BBA) - Biomembranes* **2008**, *1778*, 1344-1355; bS. Kumar, M. Zakrewsky, M. Chen, S.



Menegatti, J. A. Muraski, S. Mitragotri, *J. Controlled Release* **2015**, *199*, 168-178; cM. Witting, A. Boreham, R. Brodewolf, K. Vávrová, U. Alexiev, W. Friess, S. Hedtrich, *Mol. Pharm.* **2015**, *12*, 1391-1401.

# Curriculum Vitae

**Fang Du**

[dufangecnu@hotmail.com](mailto:dufangecnu@hotmail.com)

---

## Education

**Ph.D. Organic Chemistry**, Free University of Berlin, Berlin, **2013-2017**.

Thesis research with Prof. Dr. Rainer Haag entitled “Degradable Core-Multishell Nanocarriers for the Delivery of Bioactive Molecules”.

**M.Sc. Polymer Chemistry and Physics**, East China Normal University, Shanghai, **2010- 2013**.

Thesis research with Prof. Dr. Jiahui Yu entitled “Self-assembled Nanoscale Prodrug for Tumor Inhibition”.

**B.S., Material Chemistry**, Guizhou University, Guiyang, **2006-2010**.

Thesis with Prof. Dr. Shengjun Lu entitled “Preparation of Functional Acrylic Emulsions”.

## Scholarship and Awards

- Scholarship from Dahlem Research School (DRS), 09.2017-02.2018
- Scholarship from China Scholarship Council (CSC), 09.2013-09.2017.
- Second Best Talk Prize for 11th International Symposium on Polymer Therapeutics, Valencia, Spain, May, 2016.

## Conferences and Posters

1. **Fang Du**, Stefan Hönzke, Falko Neumann, Juliane Keilitz, Nan Ma, Sarah Hedtrich, Rainer Haag.  
Development of Biodegradable Hyperbranched Core-Multi-shell (CMS) Nanocarriers for Efficient Topical Drug Delivery  
11<sup>th</sup> International Symposium on Polymer Therapeutics, Valencia, Spain, May, 2016.
2. Michael Unbehauen, **Fang Du**, Karolina Walker, Stefan Mecking, Rainer Haag.

Ester-Based Core-Multishell Nanocarriers for the Encapsulation of Hydrophobic Drugs International Conference on Dermal Drug Delivery by Nanocarriers, Berlin, Germany, March, 2016.

3. Fang Du, Juliane Keilitz, Mohsen Adeli, Rainer Haag  
Development of Biodegradable Core-Multishell-Nanocarriers.  
4th International Symposium on Biomedical Applications of Dendrimers, Lugano, Switzerland, June, 2014.

### **Publications**

1. **F. Du**, S. Hönzke, F. Neumann, J. Keilitz, W. Chen, N. Ma, S. Hedtrich and R. Haag, *J. Controlled Release*, **2016**, 242, 42-49, *Development of biodegradable hyperbranched core-multishell nanocarriers for efficient topical drug delivery.*
2. R. Schwarzl, **F. Du**, R. Haag, and R. R. Netz, *Eur. J. Pharm. Biopharm.* **2017**, 116, 131–137. *General method for the quantification of drug loading and release kinetics of nanocarriers.*
3. M. Adeli, H. Namazi, **F. Du**, S. Hönzke, S. Hedtrich, J. Keilitz, and R. Haag, *RSC Advances*, **2015**, 5, 14958-14966, *Synthesis of Multiarm Star Copolymers Based on Polyglycerol Cores with Polylactide Arms and Their Application as Nanocarriers.*
4. Y. Fang, **F. Du**, Y. Xu, H. Meng, J. Huang, X. Zhang, W. Lu, S. Liu, J. Yu, *Colloids Surf. B Biointerfaces*, **2015**, 128, 357-362. *Enhanced cellular uptake and intracellular drug controlled release of VESylated gemcitabine prodrug nanocapsules.*
5. Y. Xu, H. Meng, **F. Du**, W. Lu, S. Liu, J. Huang, J. Yu, *In. J. Pharm*, **2015**, 495, 792–797. *Preparation of intravenous injection nanoformulation of VESylated gemcitabine by co-assembly with TPGS and its anti-tumor activity in pancreatic tumor-bearing mice.*
6. **F. Du**, H. Meng, K. Xu, Y. Xu, P. Luo, Y. Luo, W. Lu, J. Huang, S. Liu, J. Yu, *Colloids Surf. B: Biointerfaces*, **2014**, 113, 230-236. *CPT loaded nanoparticles based on beta-cyclodextrin-grafted poly(ethylene glycol)/poly (L-glutamic acid)*

*diblock copolymer and their inclusion complexes with CPT,*

7. Q. Wu, **F. Du**, Y. Luo, W. Lu, J. Huang, J. Yu, S. Liu, *Colloids Surf. B: Biointerfaces*, **2013**, *105*, 294-302. *Poly(ethylene glycol) shell-sheddable nanomicelle prodrug of camptothecin with enhanced cellular uptake,*
8. X. Zhang, **F. Du**, J. Huang, W. Lu, S. Liu, J. Yu. *Colloids Surf. B: Biointerfaces*, **2012**, *100* 155-162. *Fabrication of biodegradable micelles with reduction-triggered release of 6-mercaptopurine profile based on disulfide-linked graft copolymer conjugate.*